ACTIVE TECTONICS IN SOUTHERN ALASKA AND THE ROLE OF THE YAKUTAT BLOCK CONSTRAINED BY GPS MEASUREMENTS

By

Julie Elliott

RECOMMENDED:

Advisory Committee Chair

Chair, Department of Geology and Geophysics

APPROVED:

Dean, College of Natural Science and Mathematics

Dean of the Graduate School

August 8, 2011

Date

ACTIVE TECTONICS IN SOUTHERN ALASKA AND THE ROLE OF THE YAKUTAT BLOCK CONSTRAINED BY GPS MEASUREMENTS

A

THESIS

Presented to the Faculty

of the University of Alaska Fairbanks

in Partial Fulfillment of the Requirements

for the Degree of

DOCTOR OF PHILOSOPHY

By

Julie Elliott, B.A., M.S.

Fairbanks, Alaska

August 2011

UMI Number: 3484669

All rights reserved

INFORMATION TO ALL USERS
The quality of this reproduction is dependent upon the quality of the copy submitted.

In the unlikely event that the author did not send a complete manuscript
and there are missing pages, these will be noted. Also, if material had to be removed,
a note will indicate the deletion.

UMI 3484669
Copyright 2011 by ProQuest LLC.
All rights reserved. This edition of the work is protected against
unauthorized copying under Title 17, United States Code.

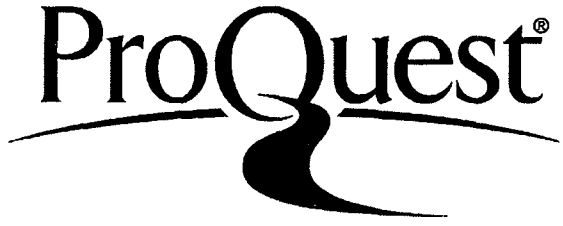

ProQuest LLC
789 East Eisenhower Parkway
P.O. Box 1346
Ann Arbor, MI 48106-1346

Abstract

GPS data from southern Alaska and the northern Canadian Cordillera have helped redefine the region's tectonic landscape. Instead of a comparatively simple interaction between the Pacific and North American plates, with relative motion accommodated on a single boundary fault, the margin is made up of a number of small blocks and deformation zones with relative motion distributed across a variety of structures. Much of this complexity can be attributed to the Yakutat block, an allochthonous terrane that has been colliding with southern Alaska since the Miocene.

This thesis presents GPS data from across the region and uses it to constrain a tectonic model for the Yakutat block collision and its effects on southern Alaska and eastern Canada. The Yakutat block itself moves NNW at a rate of 50 mm/yr. Along its eastern edge, the Yakutat block is fragmenting into small crustal slivers. Part of the strain from the collision is transferred east of the Fairweather – Queen Charlotte fault system, causing the region inboard of the Fairweather fault to undergo a distinct clockwise rotation into the northern Canadian Cordillera. About 5% of the relative motion is transferred even further east, causing small northeasterly motions well into the northern Cordillera.

Further north, the GPS data and model results indicate that the current deformation front between the Yakutat block and southern Alaska runs along the western side of the Malaspina Glacier. The majority of the ~37 mm/yr of relative convergence is accommodated along a narrow band of thrust faults concentrated in the southeastern part of the St. Elias orogen. Near the Bering Glacier, the tectonic regime abruptly changes as

crustal thrust faults give way to subduction of the Yakutat block beneath the western St. Elias orogen and Prince William Sound. This change aligns with the Gulf of Alaska shear zone, implying that the Pacific plate is fragmenting in response to the Yakutat collision. The Bering Glacier region is undergoing internal deformation and may represent the final stage of accretion of the Yakutat block sedimentary layers. Further west, modeled block motions suggest the crust is laterally escaping along the Aleutian forearc.

Table of Contents

Page

Signature Page i

Title Page ii

Abstract iii

Table of Contents v

List of Figures ix

List of Tables xi

List of Appendices xii

Acknowledgements xiii

1 Introduction 1

1.1 General 1

1.2 References 4

2 Tectonic Block Motion and Glacial Isostatic Adjustment in Southeast Alaska and Adjacent Canada Constrained by GPS Measurements 6

2.1 Abstract 6

2.2 Introduction 7

2.3 Tectonic Setting 8

2.4 Data Analysis 12

2.4.1 Dataset 12

2.4.2 Data Processing and Velocity Estimation 13

2.4.3 Coseismic and Postseismic Effects 15

2.4.4 Glacial Isostatic Adjustment Model....16
2.4.5 GIA-adjusted Velocity Field....21
2.5 Block Model....21
2.5.1 Modeling Approach....21
2.5.2 Block and Fault Geometries....24
2.5.3 A Priori Block Motion Estimates....30
2.5.4 A Priori Slip Rate Estimates....31
2.6 Results and Interpretation....31
2.6.1 Pole and Rotation Rate Estimates....31
2.6.2 Relative Block Motions....34
2.6.3 Goodness of Fit....35
2.7 Discussion....36
2.7.1 Slip Rate Estimates and Seismic Hazard....36
2.7.2 Extent of Coherent Yakutat Block....39
2.7.3 Significance of Nunatak and Foothills Blocks....40
2.7.4 The Transition Fault Paradox....42
2.7.5 Glacier Bay Structures....44
2.7.6 Southern Boundary of the Baranof Block....46
2.7.7 The Northern Cordillera Block and Strain Transfer....47
2.8 Conclusions....51
2.9 Acknowledgements....52
2.10 References....53

Appendices 77

3 Active Tectonics of the St. Elias Orogen, Alaska, Observed with GPS Measurements 97

3.1 Abstract 97

3.2 Introducton 98

3.3 Tectonic Setting 100

3.4 GPS Data and Analysis 102

3.4.1 Data Set 102

3.4.2 Data Processing and Velocity Estimation 102

3.4.3 Postseismic Effects 104

3.4.4 Glacial Isostatic Adjustment 106

3.4.5 Velocity Field 106

3.5 Block Model 107

3.5.1 Modeling Approach 107

3.5.2 Blocks and Fault Geometries 108

3.5.3 A Priori Block Motion Estimate 112

3.6 Results and Interpretation 112

3.6.1 Pole and Rotation Rate Estimates 112

3.6.2 Relative Block Motions 114

3.6.3 Goodness of Fit 115

3.7 Discussion 115

3.7.1 Slip Rates and Seismic Hazard 115

3.7.2 Onshore versus Offshore Deformation 117

3.7.3 The Malaspina Foreland Fault Zone 120

3.7.4 Bering Glacier Region Deformation 120

3.7.5 Collision and Accretion versus Subduction 123

3.7.6 Plate Coupling Variations and the 1964 Rupture 124

3.7.7 Lateral Escape in the Western St. Elias Orogen 126

3.8 Conclusions 126

3.9 Acknowledgements 127

3.10 References 128

4 The Influence of the Yakutat Block on Southern Alaska 165

4.1 General 165

4.2 References 171

List of Figures

Page

Figure 1.1 Location map for thesis study....5

Figure 2.1 Tectonic setting of southeast Alaska....64

Figure 2.2 Seismicity in southeastern Alaska and the adjacent region of Canada....65

Figure 2.3 Glacial isostatic adjustment model predictions for southeast Alaska....66

Figure 2.4 GPS velocities with GIA model predictions applied for southeast Alaska and the adjacent portion of the Canadian Cordillera....67

Figure 2.5 Blocks and bounding faults used in our southeast Alaska inversion model....68

Figure 2.6 Alternate model geometries without an offshore fault....69

Figure 2.7 Euler poles and uncertainty clouds for our preferred block model....70

Figure 2.8 Block velocity predictions for selected points in southeast Alaska and adjacent Canada....71

Figure 2.9 Relative block motion predictions for southeast Alaska....72

Figure 2.10 Velocity residuals between data and block model predictions....73

Figure 2.A-1 Glacial isostatic adjustment model predictions for southeast Alaska....77

Figure 2.A-2 Comparison between data and glacial isostatic adjustment model predictions....78

Figure 2.A-3 Comparison between data and glacial isostatic adjustment model predictions in the Glacier Bay area....79

Figure 2.A-4 Comparison of GIA model predictions for preferred model and end-member acceptable model parameters....80

Figure 2.A-5 GPS velocities with GIA model predictions applied for southeast Alaska.81

Figure 3.1 Tectonic setting for the St. Elias Orogen.....137

Figure 3.2 Seismicity in the St. Elias region.....138

Figure 3.3 Denali fault earthquake postseismic estimate for the St. Elias orogen.....139

Figure 3.4 GPS velocities with GIA model predictions and postseismic estimates applied for the St. Elias orogen.....140

Figure 3.5 GPS velocities in the Icy Bay region.....141

Figure 3.6 Block and fault geometries used in the model.....142

Figure 3.7 Alternate fault geometries 143

Figure 3.8 Poles and uncertainty estimates.....144

Figure 3.9 Model block velocity predictions for the St. Elias orogen 145

Figure 3.10 Relative block motions in the St. Elias orogen.....146

Figure 3.11 Velocity residuals between the data and block model predictions.....147

Figure 3.12 Division between tectonic regimes in the St. Elias orogen 148

Figure 4.1 Combined velocity field for southeast Alaska and the St. Elias orogen 173

Figure 4.2 Block velocity predictions along the southern Alaska margin.....174

List of Tables

Page

Table 2.1 F-test results for alternate model fault geometries....74

Table 2.2 Fault geometry parameters for block model....75

Table 2.3 Poles, rotation rates, and angular velocites....76

Table 2.B-1 GPS velocities for sites used in this study....82

Table 2.B-2 Glacial isostatic adjustment model predictions for sites used in this study..87

Table 2.B-3 Occupation histories for GPS sits....92

Table 3.1 GPS velocities used in this study....149

Table 3.2 Occupation histories for GPS sites in the St. Elias orogen....153

Table 3.3 Denali postseismic estimates....157

Table 3.4 Model fault geometry parameters....161

Table 3.5 Block poles, rotation rates, angular velocities, and uncertainties....163

Table 3.6 Sediment characteristics relative to distance from deformation front....164

List of Appendices

Page

Appendix 2.A Supplemental Figures 77

Appendix 2.B Supplemental Tables 82

Acknowledgements

A number of people contributed to my research and this thesis. First, I would like to thank my advisor, Jeff Freymueller. He has taken the time to discuss Alaskan tectonics, help solve programming and modeling problems, and read over many paper drafts. He also graciously paid the damage bill after I had borrowed field equipment destroyed by the bears of the St. Elias Mountains. My other committee members, Chris Larsen, Wes Wallace, Natasha Ruppert, and Ron Bruhn, provided me with valuable discussions, taught me about glaciology, and kept my structural geology honest.

This work required a great deal of fieldwork and I could not have done it on my own. Chris Larsen was responsible for much of the initial planning and implementation of the St. Elias GPS network and spent a great deal of time helping me to collect data. Over five field seasons, Max Kaufman, Ronni Grapenthin, Terry Pavlis, Ron Bruhn, Jay Chapman, and Steve Estes provided much appreciated help.

The fieldwork could have never been accomplished without the skills of the pilots and boat captains who took me to the remote corners of southern Alaska: Jan Gundersen and Lambert DeGavere of ERA Helicopters, George Carter of Coastal Helicopters, Steve Ranney of Orca Adventure Lodge, and Paul Claus of Ultima Thule Outfitters.

I am indebted to Terry Pavlis, Jay Chapman, Sean Gulick, Lindsay Worthington, Doug Christensen, Peter Haeussler, Jeff Benowitz, Jim Spotila, and Dave Scholl for providing early research results and comments on earlier drafts of this thesis.

Finally, I would like to thank my officemates who made the 4th Floor of the Geophysical Institute a great place to work and my friends who have made Fairbanks a fun place to live.

Chapter 1

Introduction

1.1 General

In 1890, the fledging National Geographic Society sponsored its first expedition. Under the direction of geologist Israel C. Russell, a group of ten men set out to explore the region around Mount St. Elias, Alaska (Figure 1.1) and make a preliminary study of its geology and glaciers. The trek was long and arduous, filled with crevasses to cross, mosquitos to endure, and bears to avoid, but the landscape the explorers found stretched their imaginations and descriptive abilities. After spending days crossing the Malaspina Glacier, Russell gained his first full view of St. Elias. "What a glorious sight! The great mountain seemed higher and grander and more regularly proportioned than any peak I had ever beheld before...Could I give the reader a tithe of the impressions that such a view suggests, they would declare that painters had never shown them mountains, but only hills. So majestic was St. Elias, with the halo of the sunset above his brow, that other magnificent peaks now seen for the first time or more fully revealed then ever before, although worthy the respect and homage of the most experienced mountain climber, scarcely received a second glance" [*Russell*, 1891]. As superlative as the massive ice-shrouded pyramid of St. Elias proved to be, Russell was equally astounded by something on a much smaller scale: fossil mollusk shells and leaves from living species. These fossils, found at an elevation of 5,000 feet at Pinnacle Pass east of St.

Elias, and the relative positions of the surrounding rock formations implied that the uplift of the St. Elias Mountains was rapid and recent in geologic time. "If these conclusions are sustained by future investigation, they will carry with them certain deductions which are among the most remarkable in geological history [*Russell*, 1891].

Concrete proof of recent and ongoing uplift came as soon as September 1899, when living mollusks of the same type found by Russell were thrust meters above their usual sea level along the shores of Yakutat Bay during a series of large earthquakes that shook a large swath of southern Alaska [*Tarr and Martin*, 1912]. The first major event, on September 3, caused uplift near the settlement of Yakataga (Figure 1.1) and was widely felt in southern Alaska. An event in the vicinity of Yakutat Bay on the morning of September 10 was followed by the largest event around noon on that day. These back-to-back earthquakes were felt throughout southern Alaska and the Yukon territory, were recorded at observing stations around the world, shattered glaciers in southeast Alaska, generated landslides and waves that erased prospecting camps in the upper reaches of Yakutat Bay, and caused a maximum of 14 meters of shoreline uplift [*Tarr and Martin*, 1912].

Half a century or more before the general acceptance of plate tectonic theory and the idea of mobile terranes, Russell, Tarr, and Martin could not have imagined that the underlying reason for the earthquakes and stunning topography was the collision of the Yakutat block with southern Alaska. The Yakutat block, a small terrane that travelled north along the western margin of North America, has been colliding with, accreting to, and partially subducting beneath Alaska since at least the Miocene. Although large-scale

effects of the collision, such as the St. Elias Mountains, have long been recognized, many details remain unresolved. Major questions persist, including:

- What is the velocity of the Yakutat block?
- What are the boundaries of the Yakutat block?
- What is the current deformation front between the Yakutat block and southern Alaska?
- How is the relative plate motion partitioned between various structures? Where are the active structures?
- Where does the transition between a collisional tectonic regime and subduction occur?
- What are the far-field effects of the Yakutat collision?

In this thesis, I will use GPS data to examine the Yakutat collision and develop regional tectonic block models that can help provide answers to the questions outlined above.

Beginning in Chapter 2, I will focus on southeast Alaska and the southern and eastern boundaries of the Yakutat block (Figure 1.1). A transform boundary along the Fairweather-Queen Charlotte fault system dominates the region, but there is significant off-boundary deformation. Far-field effects and the interaction between the Pacific plate and the Yakutat block receive particular attention. The tectonic interpretation is complicated by a strong glacial isostatic adjustment signal resulting from ice mass loss following the end of the Little Ice Age [*Larsen et al.*, 2005] and corrections for this effect are discussed.

Chapter 3 focuses on the St. Elias orogen of southeast and southcentral Alaska (Figure 1.1). The majority of my fieldwork time over the course of five summers was spent collecting data for this chapter. The fieldwork was conducted as part of the ST. Elias Erosion/Tectonics Project (STEEP), a multi-disciplinary study designed to gain a more thorough understanding of the Yakutat collisional zone. This region contains the present-day deformation front between the Yakutat block and southern Alaska. The GPS data reveal two major deformation regimes, one associated with a collisional tectonic environment and one with subduction, as well as several sharp strain gradients indicating major fault boundaries.

1.2 References

Larsen, C. F., R. J. Motyka, J. T. Freymueller, K. A. Echelmeyer, and E. R. Ivins (2005), Rapid viscoelastic uplift in southeast Alaska caused by post-Little Ice Age glacial retreat, *Earth Planet. Sci. Lett., 237*, 548-560.

Russell, I. C. (1891), An Expedition to Mount St. Elias, Alaska, *Nat. Geographic*, *3*, 53 – 204.

Tarr, R. S., and L. Martin (1912), The earthquakes of Yakutat Bay, Alaska in September 1899, U.S. Geol. Surv. Prof. Pap., 69, 135 pp.

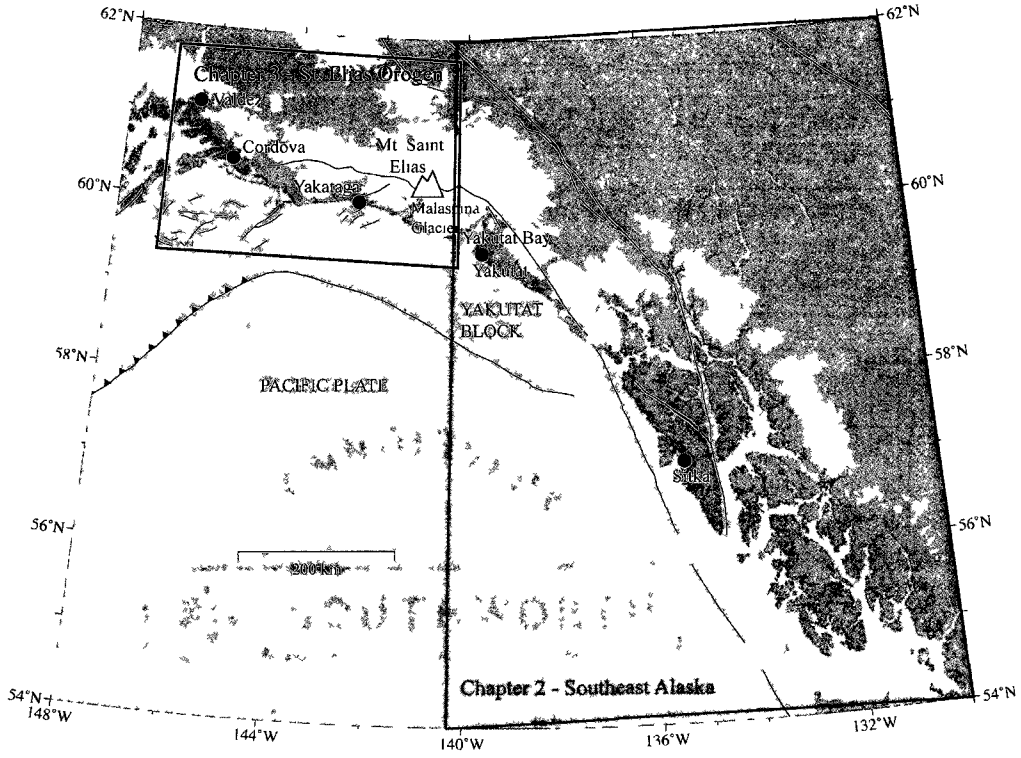

Figure 1.1. Location map for thesis study. YB is Yakutat Bay while MG is the Malaspina Glacier.

Chapter 2

Tectonic Block Motion and Glacial Isostatic Adjustment in Southeast Alaska and Adjacent Canada Constrained by GPS Measurements[1]

2.1 Abstract

We use data from campaign and continuous GPS sites in southeast Alaska and the neighboring region of Canada to constrain a regional tectonic block model that estimates block angular velocities and derives a self-consistent set of fault slip rates from the block motions. Present-day tectonics in southeast Alaska is strongly influenced by the collision of the Yakutat block. Our model predicts a velocity of 50.3 ± 0.8 mm/a towards N22.9 ± 0.6° W for that block. Our results suggest that the eastern edge of the Yakutat block is deforming. Along this edge, the Fairweather fault accommodates a large portion of the Pacific-North America relative plate motion through 42.9 ± 0.9 mm/a of dextral slip. Further south along the Queen Charlotte fault, our model predicts an average of 43.9 ± 0.6 mm/a of dextral slip and a southward increasing amount of transpression. Strain from the Yakutat collision is transferred far to the east of the strike-slip system. This strain transfer causes the region north of Glacier Bay to undergo a clockwise rotation. South of Glacier Bay and inboard of the Queen Charlotte fault, a smaller but clearly defined clockwise rotation is observed. The heterogeneous block motion north and south of

---

[1] Published as Elliott, J. L., C. F. Larsen, J. T. Freymueller, and R. J. Motyka (2010), Tectonic Block Motion and Glacial Isostatic Adjustment in Southeast Alaska and Adjacent Canada Constrained by GPS Measurements, *J. Geophys. Res., 115*(B9), B09407, 10.1029/2009JB007139.

Glacier Bay may indicate the area is undergoing internal deformation and could explain regional patterns of diffuse seismicity. The Northern Cordillera of Canada displays a small northeasterly motion. Our block model suggests that the entire southeastern Alaska – northwestern Canada margin is mobile.

2.2 Introduction

Southeast Alaska and the adjacent portion of northwest Canada form an important segment of the Pacific-North America plate boundary, marking the beginning of the transition from a transform margin to subduction along the Aleutian megathrust (Figure 2.1). The tectonics of this region is greatly complicated by the Yakutat block's collision with and accretion to southern Alaska. In the southern part of this area the plate boundary is fairly simple, with the dextral Fairweather – Queen Charlotte fault system accommodating the majority of the relative motion (*Mazzotti et al.*, 2003). From Chatham Strait northward, however, the distribution of relative motion is unclear. The partitioning of motion between onshore and offshore faults is a major question. Several studies suggested that the effects of the Yakutat collision are far-reaching [e.g. *Leonard et al.*, 2007; *Leonard et al.*, 2008; *Mazzotti et al.*, 2008] , but the available GPS data did not allow the detailed resolution of deformation inboard of the coast.

In this paper, we present a new, larger GPS dataset and use that data to develop a tectonic block model for southeastern Alaska and the neighboring part of Canada. We also present an updated version of the southeast Alaska glacial isostatic adjustment model of *Larsen et al.* [2005] and apply the horizontal model predictions to our data. A block model divides a region with complex, varied deformation patterns into a set of rigid

blocks whose motion can then be calculated. Using a block model allows us to create a kinematically consistent model that accounts for both long-term tectonic block motion and the transient effects of interseismic strain accumulation on the block-bounding faults [e.g. *Meade and Hager*, 1999; *McCaffrey*, 2002; *Meade and Hager*, 2005]. This approach avoids inconsistencies that can arise when fault slip rates or block velocities are estimated individually.

The improved GPS dataset and the block model technique provide a broader perspective on the problem of how the relative motion between the Pacific plate and North America is distributed in this region. Using poles and rotation rates from the block model, we calculate relative rates of motion between the blocks and evaluate what these mean in terms of seismic hazard and strain transfer into adjoining tectonic regions. Particular attention is paid to the question of how relative motion is partitioned between onshore and offshore faults and what this might imply about fragmentation of both the Yakutat block and the Pacific plate. Examining the deformation patterns inboard of the strike-slip system also allows us to assess how much of the present-day eastern Alaska – western Canada margin is mobile.

2.3 Tectonic Setting

The Yakutat block is a wedge-shaped allochthonous terrane that originated during the mid-Cenozoic as part of what is now the Pacific Northwest [*Bruns,* 1983] or British Columbia and southeastern Alaska [*Plafker et al.*, 1994a] and traveled north along the Fairweather – Queen Charlotte transform system. It arrived and began colliding with southern Alaska by the late Miocene, roughly 6 – 10 Ma [*Lagoe et al.*, 1993; *Ferris et al.*,

2003]. The present-day motion of the Yakutat block has been a matter of debate. Some studies have concluded that the Yakutat block moves mainly with the Pacific plate with little or no relative motion between the two [e.g. *Plafker et al.*, 1994a; *Bruns*, 1983] while others have suggested that significant Pacific plate – Yakutat block relative motion exists [e.g. *Fletcher and Freymueller*, 1999; *Perez and Jacob*, 1980].

The dextral Fairweather-Queen Charlotte fault system is a major tectonic feature of southeast Alaska and accommodates most of the Pacific – North America relative plate motion. The Fairweather fault is usually taken to be the eastern boundary of the Yakutat block [*Plafker et al.,* 1978; *Lahr and Plafker,* 1980]. The fault extends from the vicinity of Yakutat Bay to Chatham Strait, where it is postulated to connect with the Queen Charlotte fault [*Plafker et al.*, 1994a]. Several M_w>7 earthquakes have occurred along the fault during the past century (Figure 2.2). In 1958, a M_w7.9 earthquake occurred just north of Cross Sound [*Doser and Lomas*, 2000]. The earthquake resulted in well-documented dextral slip of up to 3.5m and the onshore surface rupture extended over 200 km to at least the northern end of Yakutat Bay [*Plafker et al.*, 1978]. In 1972, the M_w7.6 Sitka earthquake ruptured 180 km offshore the Alexander archipelago [*Doser and Lomas*, 2000; *Schell and Ruff*, 1989]. A M_w7 earthquake in 1927 occurred in the region between the ruptures of the two larger earthquakes [*Doser and Lomas*, 2000]. Geologic and geodetic slip rate estimates for the Fairweather fault range from 41 – 58 mm/a [*Plafker et al.*, 1978; *Lisowski et al.*, 1987; *Fletcher and Freymueller,* 2003]. A segment of the Queen Charlotte fault located south of our study area generated a M_w8.1 right-lateral

strike-slip earthquake in 1949. In 2004, a M_w6.8 event occurred near the northern end of the fault.

Perhaps the most enigmatic tectonic feature in southeast Alaska, the Transition fault forms the southern boundary of the Yakutat block. Based on undisturbed sediments seen in seismic reflection data, *Bruns* [1983] concluded that the Transition fault has been inactive since the Pliocene and is a fossil fracture zone. In 1973, a series of earthquakes occurred outboard of Cross Sound near the southeastern edge of the Transition fault (Figure 2.2). The M_s6.7 mainshock and the two largest aftershocks had focal mechanisms consistent with thrust/reverse faulting on a fault dipping to the northeast [*Doser and Lomas*, 2000]. *Perez and Jacob* [1980] estimated that the Transition fault accommodates about 10 mm/a of N30°E directed convergence between the Pacific plate and Yakutat block based on seismic slip vectors. The block model of *Lahr and Plafker* [1980] included 4 mm/a of Pacific plate – Yakutat block relative motion across a dextral/oblique Transition fault. A GPS study by *Fletcher and Freymueller* [1999] found that ~20 mm/a of Yakutat – Pacific relative convergence must be accommodated on an offshore fault, with the Transition fault suggested as the obvious candidate. Deriving a Yakutat block rotation pole from a small network of GPS velocities and fault azimuth data, *Pavlis et al.* [2004] estimated nearly pure thrust motion along the Transition fault at rates increasing from about 10 mm/a at the southeast end to more than 30 mm/a at the northwestern end. *Gulick et al.* [2007] reported on seismic reflection and bathymetric data that implies the eastern end of the Transition fault has developed into a strike-slip fault. A tectonic model in that study suggested that the entire fault accommodates 10

mm/a or less relative plate motion. Wide-angle seismic data and seismic reflection profiles collected across the Transition fault offshore Yakutat Bay in 2008 indicate that the major, developed structure is nearly vertical and thus likely to be a strike-slip fault if it is active [Gail Christeson, personal communication, 2009].

Southeast Alaska and the adjacent region of Canada exhibit several distinct seismicity trends inboard of the Fairweather-Queen Charlotte system. A band of small earthquakes follows the trace of the Duke River fault [*Horner*, 1983; *Mazzotti et al.*, 2008] (Figure 2.2), suggesting that it may be involved in the distribution of the relative plate motions. The eastern Denali fault shows low levels of seismicity between the Duke River fault and Chatham strait. No seismic activity is seen along the Chatham Strait fault [*Horner*, 1983; *Mazzotti et al.*, 2008] (Figure 2.2).

A trend of seismicity is also found across the Glacier Bay region between the Fairweather and eastern Denali faults. *Horner* [1983] suggested that the seismicity and high uplift rates observed in Glacier Bay indicated the presence of convergence across the Fairweather fault. Using a model constrained by raised shoreline dating, tide gauge data, and GPS measurements, *Larsen et al.* [2005] concluded that the high uplift rates seen in Glacier Bay are due to glacial isostatic adjustment, not tectonics. Seismicity in this region has consisted of mostly smaller events, with only one possible $M \geq 6$ earthquake recorded east of the Fairweather fault. *Doser and Lomas* [2000] interpret that event, a M6.0 earthquake in 1952, as a right-lateral strike-slip event that may have occurred on the Border Ranges fault east of the Fairweather fault. Several smaller,

M≥4.5 earthquakes have also occurred in this area in the recent past and the available focal mechanisms show a mixture of strike-slip and thrust events (Figure 2.2).

Further to the north, a series of very large earthquakes occurred between Icy Bay and Yakutat Bay in September 1899. A M_s7.9 event on September 4 preceded a M_s7.4 foreshock and a M_s8.0 mainshock on September 10 [*Doser*, 2006]. The September 10 mainshock generated the largest known onshore coseismic vertical displacement, 14 m of uplift near the head of Yakutat Bay [*Tarr and Martin*, 1912]. The analysis of *Doser* [2006] suggests that the September 10 foreshock occurred offshore southeast Alaska and possibly involved the Transition fault while the mainshock occurred near Yakutat Bay and may have ruptured onshore thrust faults (Figure 2.2). *Doser* [2006] located the September 4 event within the Pamplona thrust zone to the west of Icy Bay.

2.4 Data Analysis

2.4.1 Dataset

We use GPS data collected at 102 sites in southeast Alaska, Yukon Territory, and British Columbia (Appendix 2.B). Four of the sites are continuously running GPS sites; the other 98 are campaign sites. The continuous GPS sites have operated for 6 – 10 years. The campaign sites each have between 2 and 11 visits and the time span between first and last visits ranges from 4 to 15 years (Appendix 2.D). Much of the campaign data is an extension of the dataset presented by *Larsen et al.* [2005]. Many of the velocities reported in that study now have been enhanced by at least one additional occupation. We also use data from several Canadian Base Network sites and augment data we collected at some campaign sites with data collected at those sites by Geomatics

Canada and the Pacific Geoscience Centre, Geological Survey of Canada [*Leonard et al.*, 2007; *Henton et al.*, 2006].

2.4.2 Data Processing and Velocity Estimation

We used the GIPSY/OASIS GOA4 software developed by the Jet Propulsion Laboratory (JPL) [*Zumbrege et al.*, 1997] to analyze the GPS data presented here. Data from each day were analyzed separately to create daily loosely constrained frame-free solutions. For data collected prior to 1995, we combined the Alaska data with data from global International GPS Service (IGS) sites and estimated orbits. For data collected from 1995 onwards, we used JPL's fiducial-free orbits. We transformed the daily solutions into the International Terrestrial Reference Frame 2000 (ITRF2000, realization IGSb00). We used ITRF2000 rather than the more recent ITRF2005 because of our need to express our solutions in a North America-fixed frame. We consider the estimate of *Sella et al.* [2007] to be the most reliable determination of the motion of North America as it is based on substantially more data than any other estimate and considers the effects of glacial isostatic adjustment. The estimate of *Sella et al.* [2007] is based on ITRF2000 (IGSb00) and should not be used with ITRF2005 due to differences between the frames. The daily solutions were combined in a linear least-squares inversion to estimate velocities at each GPS site.

In our uncertainty estimates, we included uncertainties in the definition of the North America-fixed frame and in the geocenter stability of ITRF in addition to the formal errors in site velocities. The ITRF2000 and ITRF2005 frames differ by a ~ 1.8 mm/a geocenter translation along the spin axis (Z axis). At the latitudes considered in

this study, the geocenter difference results in a velocity difference of ~ 1 mm/a in the north component and ~ 1 mm/a in the vertical component. *Argus* [2007] and *Kogan and Steblov* [2008] both attempted to estimate a geocenter correction to ITRF. The result of *Argus* [2007] lies between ITRF2000 and ITRF2005 while *Kogan and Steblov* [2007]'s result is closer to ITRF2000. Since we do not know if either frame is correct, we augmented the velocity uncertainties by 1.8 mm/a in the Z component, which reduces the weight given to the north and vertical velocity components accordingly. The impact of any small bias in the velocities on the model results in this paper is very small. The use of ITRF2000 in both our velocity estimates and our choice of reference plate pole minimizes the bias. Further details about the processing, velocity estimation, and the augmentation of uncertainties due to possible systematic errors can be found in the work of *Freymueller et al.* [2008].

2.4.3 Coseismic and Postseismic Effects

The data time span for many sites (Appendix 2.D) crosses the date of the 2002 Denali fault earthquake and we applied a correction for the coseismic displacements [*Hreinsdottir et al.*, 2006] to each station as part of the velocity estimation. The magnitude of the correction ranges from 2 mm to 14 mm across our network, with the larger displacements located in Canada east of the Shakwak strand of the Denali fault (Figure 2.1). Postseismic deformation from the Denali earthquake is very small for most of the area considered in this study. A robust postseismic deformation model for our study area is not available as published models [*Pollitz*, 2005; *Freed et al.*, 2006; *Johnson et al.*, 2009] significantly over predict the postseismic effect in the far field. We were

able to calculate the difference between the pre-earthquake and post-earthquake velocities at a number of sites in the Northern Cordillera, near the Duke River fault, and in the city of Yakutat (Figure 2.1). These sites, as the sites closest to the 2002 rupture, would be expected to display the largest postseismic effects. Only the two most northerly sites, Y565 and DEST (Appendix 2.B), displayed differences greater than their 2-σ uncertainty estimates. For these two sites, we used only the pre-earthquake data to determine their velocities. The other sites had differences at or below the 1-σ level. The differences between the pre-earthquake velocities and velocities calculated using both pre- and post-earthquake data were even smaller. For this reason, we used all available data to calculate velocities at the remaining 100 sites in our dataset.

We did not correct for the postseismic effects of the 1964 M9.2 Prince William Sound earthquake. Our study area is over 250 km east of the end of that rupture. The model of *Suito and Freymueller* [2009] predicts that southeast Alaska sites showing the largest effect, Y565 and the site at Yakutat, have postseismic motion of 0.1 mm/a and 0.2 mm/a, respectively.

We also do not correct for the possible postseismic effects of the 1958 earthquake on the Fairweather fault or the 1899 earthquake sequence. While formal postseismic models do not exist for either the 1899 or 1958 earthquakes, we can estimate the degree to which any postseismic effect from those events would have decayed by the present time. If we assume a shear modulus of 70 GPa (based on PREM [*Dziewonski and Anderson*, 1981]) and an asthenosphere viscosity of 3.7e18 Pa s [*Larsen et al.*, 2005], we obtain a Maxwell relaxation time of ~ 2 years for southeast Alaska. Even if these ~M8

events had considerable initial postseismic effects, they would have decayed into negligible amounts by the present day. Corroborating this, *Fletcher and Freymueller* [2003] used both EDM data collected in the 1980's and GPS data collected in the 1990's in the region of the 1958 rupture and found the two datasets to be compatible. If substantial postseismic effects from the 1958 event were present, the decade time lapse between the datasets should have resulted in apparent differences.

2.4.4 Glacial Isostatic Adjustment Model

Southeast Alaska has experienced considerable ice volume loss since the end of the Little Ice Age (LIA) in the late 1700's [*Motyka*, 2003; *Larsen et al.*, 2004]. The glacial isostatic adjustment (GIA) due to this ice loss results in the fastest ongoing isostatic uplift measured anywhere [*Larsen et al.*, 2005]. Two uplift centers have been identified with peak uplift rates of 30 mm/a in Glacier Bay and 32 mm/a in the Yakutat icefield. We find that the GIA models discussed below indicate horizontal deformation associated with this ice loss reaches maximum values in excess of 7 mm/a and overprints the regional tectonic deformation pattern. Tectonic interpretation of the regional deformation field relies on first accounting for the GIA horizontal signal. Here we follow the approach of *Larsen et al.* [2005], but use an updated dataset and an improved model calculation.

To model the Earth's viscoelastic response to ice load changes in southeast Alaska, we tested a suite of Earth models in which we varied the effective elastic lithospheric thickness and the viscosity profile of the upper mantle while minimizing misfit between the observations and the predicted uplift. The models presented here use a non-rotating,

incompressible, self-gravitating, Maxwell viscoelastic spherically symmetric Earth model and are computed using the TABOO program [*Spada et al.*, 2003; *Spada*, 2003; *Spada et al.*, 2004]. Numerically, this model uses axial-symmetric disks to describe surface loads and both the current models and previously presented models [*Larsen et al.*, 2005] use the same surface load geometry and load history.

In our earth model, we explicitly include a thin, low viscosity asthenosphere overlaying the upper mantle. The density and elastic properties of the Earth model follow the seismic model PREM [*Dziewonski and Anderson*, 1981]. We expanded the spherical harmonics used throughout the numerical modeling to degree and order 2048 in order to resolve small ice load changes and their effects. This is a factor of two greater resolution on the numerical earth modeling compared to the previously presented models [*Larsen et al.*, 2005]. The higher resolution accommodates the denser distribution and greater accuracy of the GPS data and is fully consistent with the 20 x 20 km resolution of the ice model.

The earth model parameters and the ranges over which we varied them are as follows: lithospheric elastic thickness, 30-120 km, asthenosphere thickness and viscosity, 80-150 km and 1 x 10^{18}-5 x 10^{19} Pa s, and upper mantle viscosity, 1 x 10^{20}-5 x 10^{20} Pa s. Misfit with the observations was found to rapidly increase at the upper and lower limits of all of these parameter ranges. Our GIA model assessments were performed through comparisons of model predictions to vertical GPS velocities, raised shoreline records of RSL (relative sea level), and the tide gauge rates of RSL as described in *Larsen et al.* [2005]. We did not attempt to analyze the horizontal motions resultant from our rebound

models here as has been done in Fennoscandia [*Milne et al.*, 2001], because the dominant horizontal signal observed in southern Alaska is of tectonic origin.

These earth models were subjected to two ice load models simultaneously – one that approximates southern Alaskan and adjoining Canadian glacial history ("Regional") and another that describes the asynchronous behavior of the Glacier Bay icefield ("Glacier Bay"). Both of these load histories were held fixed in magnitude and timing for all of the rebound model results presented here. Only the last ~2 ka of load histories were considered in our Regional and Glacier Bay load models. Earlier load changes have relatively minimal effects on present day velocities [*Larsen et al.*, 2005]. Load histories for both the Regional and Glacier Bay ice models are shown in Figure 2.5 of *Larsen et al.* [2005] and account for both loading and unloading phases of the past 2000 years. The present response is dominated by the unloading phase over approximately the past 100-200 years.

The regional ice load model used here is unchanged from previous studies [*Larsen et al.*, 2005]. It estimates the change in ice volume through the advance and retreat of the LIA [*Porter*, 1989; *Wiles et al.*, 1999]. The measured rates of volume change [*Arendt et al.*, 2002] were extrapolated to estimate the LIA peak volume in 1900. Earlier volume changes are based on the relative strength of the advance and retreat cycles [*Wiles et al.*, 1999]. We used Neoglacial terminal moraine positions to estimate differential ice volume of these earlier advance and retreat cycles [*Larsen et al.*, 2004], a method that can be problematic in polar systems but is realistic in rapidly adjusting temperate ice systems [*Harrison et al.*, 2003]. The spatial distribution of ice thickness change throughout the

load history was allotted according to elevation [*Arendt et al.*, 2002]. The distribution of these thickness changes was gridded at a 20-km x 20-km resolution and assigned a history. This regional ice load model is based on dendrochronologic and geomorphologic histories of the LIA in southern Alaska [*Porter*, 1989; *Wiles et al.*, 1999].

We accounted for the large-scale retreat of the Glacier Bay icefield in a separate load model, also unchanged from *Larsen et al.* [2005]. We modeled an ice volume loss of 3030 km^3 from the collapse of the icefield, which occurred rapidly (< 250 years beginning ca. 1780 AD) through the process of a tidewater calving retreat. This localized ice wastage represents the largest post-LIA deglaciation known to us. Greater than the volume lost from all Alaskan and neighboring Canadian glaciers between 1955 and 2002 [*Arendt et al.*, 2002], it covered a much smaller area with ice thickness changes of up to 1.5 km [*Clague et al.*, 1993]. The volume of ice lost in Glacier Bay alone since the end of the LIA is equivalent to a global rise in seal level (SLE) of 8 mm.

The best-fit earth model parameters found here are slightly different from those of *Larsen et al.* [2005]: a 50 km (vs. 60 km in the previous model) thick lithosphere overlying a 110 km thick asthenosphere of viscosity 3.7×10^{18} Pa s (vs. $2.5\text{-}4.0 \times 10^{18}$ Pa s) over an upper mantle with a viscosity of 4×10^{20} Pa s. The best-fit model now results in a reduced χ^2 value of 1.29 while the previous model had a reduced χ^2 value of 1.52. These minor differences result from a combination of the expanded degree and order of the spherical harmonics and the increased spatial density and accuracy of the GPS dataset used, but do not represent a significant change from our earlier results. Specifically, the best-fit earth model parameters of *Larsen et al.* [2005] lie within the 95% confidence

region of the present estimate. Figure 2.3 shows the full 3-D deformation field of the modeled GIA motion at selected sites in southeast Alaska and Appendix 2.C lists the model predictions for each site. Figures 2.A-2 and 2.A-3 shows a comparison between the modeled horizontal GIA motion and our horizontal GPS velocities.

These GIA predictions are subject to the assumptions inherent in the earth models we have invoked as well as to the degree to which the data can constrain the models. We have assumed an incompressible earth model. *Árnadóttir et al.* [2009] showed that an incompressible earth model can underestimate the horizontal velocities associated with GIA by factor of 1.5 when compared to compressible earth models while vertical velocities appear to be largely insensitive to the choice. Because of this contrast in sensitivity, our results could underestimate the GIA horizontal effects while still providing a good fit to the observed vertical velocities.

In order to test the widest range of reasonable predictions of horizontal GIA effects in the tectonic models that follow, we considered two additional models beyond the best-fit model. These two models (elastic lithospheric thickness with asthenosphere viscosity: 50 km with 7 x 10^{18} Pa s, 85 km with 1.5 x 10^{18} Pa s) lie on opposite edges of the 95% confidence range and represent the greatest allowable variation in model parameters (see Figure 6, *Larsen et al.* [2005], for description of the misfit distribution). The resulting predictions of the horizontal GIA effects at the sites in our GPS network vary by a factor of two or more in magnitude at some sites and also display considerable variations in azimuth compared to the best-fit model (Figure 2.A-4). Although we do not explicitly test the effects of our assumption of incompressibility in the earth models, the range of

horizontal GIA effects produced by our three test models reasonably accommodates the range of predictions that could be associated with various assumptions of compressibility/incompressibility. In the development of our tectonic block model, we favor the best-fit GIA model but also use the two end member models to gauge their effects on our conclusions.

2.4.5 GIA-adjusted Velocity Field

Figure 2.4 shows the GPS velocities with the predicted horizontal GIA motion removed. Velocities near the Fairweather fault show nearly uniformly northwest-directed motion while velocities closer to the coast display slightly more northerly motion. The largest magnitude velocities, ~ 50 mm/a, border Yakutat Bay, with little difference seen between the magnitudes at sites on the north and south sides of the mouth of the bay. Inboard of the coast, sites between the Fairweather – Queen Charlotte system and Denali fault – Coast Shear zone have comparatively slower velocities and this portion of the velocity field displays a distinct clockwise rotation. East of the eastern Denali fault, velocities have a nearly uniform northeasterly trend and decrease in magnitude from north to south. East of 130°W longitude, velocities at sites in the Canadian Base Network have very small magnitudes.

2.5. Block Model

2.5.1 Modeling Approach

To develop our block model for southeast Alaska and northwest Canada, we adapted the method of *Meade and Hager* [2005]. We present a summary of the method below; further details can be found in their study.

Assuming linear elasticity, we can express the interseismic velocity $\vec{v}_I$ observed at a GPS site as a combination of block motion and elastic effects:

$$\vec{v}_I = \vec{v}_B(\vec{x}_{site}) - \vec{v}_{SD}(\vec{x}_{site}, \vec{x}_{geom}) \quad (1)$$

The GPS site coordinates correspond to $\vec{x}_{site}$, the fault geometry to $\vec{x}_{geom}$, and the block velocity to $\vec{v}_B$. The term $\vec{v}_{SD}$ represents the slip deficit accumulating on a locked fault.

When dealing with block velocities, it is convenient to work in terms of rotations in an earth-centered Cartesian (XYZ) coordinate system. The angular velocities of the blocks are then represented by $\Omega = [\Omega_X, \Omega_Y, \Omega_Z]$. Rewriting the equation for block velocity in terms of Ω yields

$$\vec{v}_B(\vec{x}_{site}) = \vec{\Omega} \times \vec{x}_{site} = \mathbf{R}_B(\vec{x}_{site})\vec{\Omega} \quad (2)$$

where $\mathbf{R}_B(\vec{x}_{site})$ is a linear cross product operator that is a function of the site coordinates.

The slip deficit term can be written as

$$\vec{v}_{SD} = \mathbf{G}(\vec{x}_{site}, \vec{x}_{geom})\vec{s} \quad (3)$$

where $\mathbf{G}$ is the matrix of Green's functions that relate slip, $\vec{s}$, on each fault plane to the displacement at each GPS site assuming an elastic half-space and a Poisson's ratio of 0.25 [*Okada*, 1985].

The slip vector is written as

$$\vec{s} = \mathbf{R}_{FP}(\vec{x}_{geom})\mathbf{R}_{X\to E}(\vec{x}_{geom})\mathbf{R}_{vdiff}(\vec{x}_{geom})\vec{\Omega}. \quad (4)$$

$\mathbf{R}_{vdiff}(\vec{x}_{geom})$ takes the angular velocities for two neighboring blocks and calculates their relative velocity at the midpoint of each plane of the fault that divides them. $\mathbf{R}_{X\to E}(\vec{x}_{geom})$ transforms the relative velocities from the XYZ coordinate system to the

ENU system. Finally, $\mathbf{R}_{FP}(\vec{x}_{geom})$ projects the relative velocities into fault parallel and fault perpendicular components. Each fault plane is only allowed two components of slip, either strike-slip and fault normal (contraction or extension) if the fault is vertical or strike-slip and dip-slip if not.

The fault slip rates directly depend on the block angular velocities and the block geometries. Since the slip rates cannot vary independently of each other, the block model ensures that the estimated slip rates are internally consistent (see Figure 2, *Meade et al.* [2002]).

By substituting (4) into (3) and combining the successive transformations into a single matrix $\mathbf{R}_{SD}$, (1) can be rewritten as

$$\vec{v}_I = (\mathbf{R}_B - \mathbf{R}_{SD})\vec{\Omega}. \tag{5}$$

To include a priori block angular velocities and slip rates in the model, a system of equations can be written as follows:

$$\begin{bmatrix} \vec{v}_I \\ \vec{s}_{apr} \\ \vec{\Omega}_{apr} \end{bmatrix} = \begin{bmatrix} \mathbf{R}_B - \mathbf{R}_{SD} \\ \mathbf{R}_{FP}\mathbf{R}_{X\to E}\mathbf{R}_{vdiff} \\ \mathbf{I} \end{bmatrix} \vec{\Omega} \tag{6}$$

where $\mathbf{I}$ is the identity matrix.

Equation (6) can be written as

$$\vec{d} = \mathbf{R}\vec{\Omega} \tag{7}$$

where $\vec{d}$ contains the east and north components of the GPS velocities, the a priori slip estimates, and the a priori block angular velocities.

This equation allows us to solve for the block angular velocities $\vec{\Omega}$ through a weighted linear least-squares inversion.

$$\vec{\Omega}_{est} = (\mathbf{R}^T \mathbf{W} \mathbf{R})^{-1} \mathbf{R}^T \mathbf{W} \vec{d}$$

where $\mathbf{W}^T\mathbf{W} = \Sigma^{-1}$ and Σ is the data covariance matrix. Besides containing the variance of the observed east and north GPS velocities and the correlations between the east and north components of the GPS data, Σ contains uncertainty estimates for a priori slip rates and block angular velocities. In our implementation, predictions from an a priori model calculated using our a priori block angular velocities (see Section 2.4.3 below) are subtracted from the data. The estimated angular velocities obtained from the inversion are corrections to that a priori model.

Slip rate and linear block velocity uncertainty estimates are calculated by propagating the estimated uncertainty for $\vec{\Omega}_{est}$ through (4) and (2), respectively.

2.5.2 Block and Fault Geometries

Our block model for southeast Alaska and the neighboring region of Canada includes ten blocks and plates and eleven bounding faults or fault zones (Figure 2.5). Block boundaries are either recognized faults (through geologic studies or documented seismic activity) or previously postulated faults or fault zones. Locations generally follow mapped traces on geologic maps, seismicity trends, or topography. Due to the region's ruggedness and ice cover, the map traces often represent inferred faults or uncertain locations.

Most of our model faults are well known and based on the map of *Plafker et al.* [1994b], but several of our faults and block designations came from other sources and

merit further discussion. *Richter and Matson* [1971] and *Lahr and Plafker* [1980] postulated that a connection between the southern end of the Totschunda fault and the Fairweather fault existed. There are a number of NNW-ESE oriented linear valleys in the region that could indicate the presence of a fault. Exposed geological features along the East Nunatak and Art Lewis glaciers east of the Fairweather fault in the Yakutat icefield are compatible with right-lateral slip [G. Plafker, personal communication, 2006]. Using geologic slip rates as inputs into a finite element model for southern Alaska, *Kalbas et al.* [2008] concluded that the presence of a connection between the Totschunda and Fairweather faults provided the best explanation of the data. Our modeled Totschunda-Fairweather connector fault branches off the Fairweather fault near the Art Lewis glacier and follows linear, ice-filled valleys northwestward before making a simple connection to the Totschunda fault (Figure 2.5).

The Chatham Strait fault (Figure 2.1) would seem like a plausible location for a block boundary as it appears to connect to the Eastern Denali fault [e.g. *Lahr and Plafker,* 1980], but there is little to no seismicity along that fault (Figure 2.2). The GPS velocity field (Figure 2.4) shows no indication of an active fault along the Strait; the velocities instead imply that GPS sites on either side of the Strait belong on the same crustal block. We propose the Coast Shear zone as an alternative block boundary (Figure 2.1; Figure 2.5), following *Lanphere* [1978] who suggested that the Eastern Denali fault might continue onto the Coast Shear zone instead of the Chatham Strait fault. The Coast Shear zone serves as the general boundary between the western metamorphic belt and the Coast Mountains batholith to the east [*Brew and Ford*, 1998; *McClelland et al.*, 2000;

McClelland et al., 1992; *Klepeis et al.*, 1998]. Along much of its length, the Coast Shear zone coincides with a tonalite sill belt [*Brew and Ford*, 1981; *Brew*, 1994; *Brew and Ford*, 1998]. Both contraction and dextral transpression appear to have occurred along the Coast Shear zone during early Tertiary time and it may have played a role in strain partitioning during oblique subduction of the Kula plate beneath North America [*Rusmore et al.*, 2001; *Klepeis et al.*, 1998]. *McClelland et al.* [2000] suggested that the Coast Shear zone originated as a strike-slip structure and may have played a role in the evolution of the Denali fault system.

We have subdivided two previously recognized blocks (Yakutat and Fairweather) in order to provide the best fit between the GPS data and our block model. First, we modified the Fairweather block of *Fletcher* [2002]. The Duke River fault replaces the northern Eastern Denali fault (Shakwak strand) and the Totschunda and Totschunda-Fairweather connector faults as the northern boundary. A northwest-southeast trending band of seismicity roughly follows the trace of the Duke River fault [*Leonard et al.*, 2007; *Horner*, 1983] (Figure 2.2). In contrast, the Shakwak strand shows only sparse present-day seismicity. Paleoseismological evidence obtained from resuspended lake sediments suggests that the Duke River fault and southern Eastern Denali fault (Dalton strand) have been seismically active during the past 300-500 years [*Doig*, 1998]. This change minimized the misfit between our model and several of the GPS sites in the vicinity of the Duke River fault.

Second, we added two small blocks, the Nunatak block and the Foothills block, along the eastern edge of the Yakutat block. Our initial motivation for including onshore

faults along the edge of the Yakutat block was to reduce the unreasonably high rate of convergence (~ 20 mm/a) across the Transition fault predicted by an early version of our block model. As mentioned earlier, recent offshore seismic data suggests that the Transition fault does not have significant thrust fault characteristics. In order to evaluate the compatibility of onshore faults with the GPS data and determine if both offshore and onshore faults were required by the data, we tested a number of alternate fault geometries. For each trial geometry, we performed the inversion, calculated misfit, and ran F-ratio tests to determine the statistical significance of the results. The offshore fault involved was the Transition fault while the onshore faults were the Boundary fault and the Foothills fault. The Boundary fault is a well-known mapped fault while the Foothills fault used here is a modified version of the Yakutat fault of *Plafker and Thatcher* [2008]. We tried four combinations of onshore faults (Figure 2.6, Table 2.1) without an offshore fault as well as several combinations of onshore and offshore faults. Our results show that if no offshore fault is present, including both onshore faults provides the best fit to the data. This model, however, fits more poorly than one with the Transition fault and without either onshore fault. The best-fit model has the Transition fault plus both onshore faults, the presence of which greatly reduced the misfit at sites along the northern Fairweather fault. The addition of each fault to our block model met or exceeded the F-test criteria for significance at the 95% level (Table 2.1). The implications of these faults and blocks are discussed further below.

Finally, our model includes a boundary across Glacier Bay. In the northern Glacier Bay region, structures undergo an abrupt change from north-south strikes to east-

west trends [*Brew et al.*, 1978; *MacKevett et al.*, 1971]. This change is particularly obvious at Tidal Inlet, a nearly perfectly east-west trending fjord. *MacKevett et al.* [1971] reported an east-west fault zone here. *Brew et al.* [1978] also noted the presence of a zone of east-west trending faults in the northern section of Glacier Bay and remarked on the unusual orientation. The change in structural strike occurs along the southern edge of observed band of seismicity discussed earlier and separates a more seismically active region in the north from a seismically quiet region to the south. In addition, GPS velocities in the north are generally faster than those in the southern region (Figure 2.4). We included a boundary, designated the Glacier Bay Partition (GBP), running between the Fairweather and Denali faults through Tidal Inlet, dividing the Fairweather block to the north from the Baranof block to the south. Compared to the best-fit model discussed in the previous paragraph, the GBP model reduced the overall misfit by ~ 10% and exceeded the F-test criteria for significance at the 99% level (Table 2.1). The GBP is discussed further below.

For our modeling purposes, we assumed that the region north of the central segment of the Denali fault is part of the North American plate. We adopted the Southern Alaska block (SOAK) of *Fletcher* [2002] and assume that block occupies the area south of the Denali-Totschunda system and north of the Chugach and St. Elias Ranges (Figure 2.1). We defined the region immediately east of the Eastern Denali fault and Coast Shear zone to be the Northern Cordillera block, following *Mazzotti and Hyndman* [2002].

Fault locking depths, dips, and widths in the down-dip directions are all fixed; they are not estimated as part of the inversion. We used an iterative process to adjust fault segment endpoints, fault locking depths, and fault width and dip to find the fault geometry that provided the best fit to the GPS data. For each fault, we began with published estimates of the fault geometry, most of which were derived from seismic or geodetic data. If no published estimate or other information was available, we began with a vertical fault with a locking depth of 10 km. If a fault segment had no nearby GPS data to constrain the iterative process, we assigned the fault parameters compatible with neighboring faults. There were two exceptions to this process. The first was the Transition fault. While the northern and central regions were designated as vertical to agree with the offshore seismic reflection data, the southern segment was defined as a steeply dipping thrust fault to agree with the 1973 Cross Sound Earthquakes. The second exception concerns the Boundary and Foothills faults. *Plafker and Thatcher* [2008] used vertical shoreline displacement measurements to constrain a coseismic model for the 1899 earthquakes. In that model, the Boundary fault dips 10° to the NE while the Yakutat fault dips 30° to the NE. Our model Boundary fault dips 85° to the NE and our Foothills fault is vertical. Our model geometries were chosen to minimize both the misfit to the GPS data and the amount of contraction across the Transition fault. These geometries are discussed further below. Table 2.2 lists fault geometry parameters for the faults used in this model.

2.5.3 A Priori Block Motion Estimates

Our modeling approach allows the inclusion of a priori block motion estimates. We chose to use a priori block angular velocities for three of the blocks in our model: Pacific, North America, and SOAK. Our dataset does not include any GPS sites on these three blocks, so their inclusion is only important for the calculation of deformation along their boundaries. North America is our reference block – all of our GPS velocities and block angular velocities (estimated and a priori) are relative to it. We used the definition of North America presented by *Sella et al.* [2007]. The GPS data used by *Sella et al.* [2007] to develop this model were aligned with ITRF2000 (IGSb00 realization), so this estimate of North American plate motion will not have reference frame compatibility problems with our GPS velocities. As our a priori Pacific plate motion estimate, we used the GPS-derived angular velocity estimate of *Plattner et al.* [2007], who also used the IGSb00 realization of ITRF2000. We used the pole and rotation rate determined by *Fletcher* [2002] for the motion of SOAK relative to North America. In that model, SOAK rotates counterclockwise about a pole in Prince William Sound. The small circle geometry of the central Denali fault constrains the location of the pole.

Along with the angular velocities, we included uncertainties for the motion of the Pacific plate, North America, and SOAK as a priori information. To ensure numerical stability during the inversion and limit the maximum rate of vertical axis rotation for small blocks, we also applied loose a priori uncertainties to the estimated angular velocities in our block model. These uncertainties were large, with σ equal to 0.1 radians/Ma.

2.5.4 A Priori Slip Rate Estimates

With three exceptions, we did not constrain the sense of slip on any of the faults; the slip is solely controlled by the inversion. The first exception is the Eastern Denali fault between the Totschunda and Duke River faults (Shakwak strand), to which we assigned dextral slip of 5 ± 5 mm/a based on recent geologic studies [*Seitz et al.*, 2008]. There are no GPS sites along this part of the fault, so the geologic slip rate estimate is the only data for this segment. For a similar reason, we constrained the Totschunda fault to have 6 ± 6 mm/a of dextral slip following the geologic estimate of *Seitz et al.* [2008]. Finally, we constrained the Dalton strand of the Eastern Denali fault to have 0 ± 3 mm/a of fault normal motion. We did not constrain the fault parallel motion on this fault. The initial unconstrained iteration of the block model predicted > 5 mm/a of contraction across this portion of the fault. Previous geodetic and geologic studies [e.g. *Fletcher and Freymueller*, 2003; *Plafker et al.*, 1994a] have concluded that the fault is primarily a dextral fault, so we considered this rate to be unreasonably high.

2.6 Results and Interpretation

2.6.1 Pole and Rotation Rate Estimates

We inverted 246 data (east and north components of GPS velocities at 102 sites, X, Y, and Z components of a priori angular velocities for 10 blocks, and 12 slip constraints) to estimate 21 model parameters (X, Y, and Z components of angular velocity for 7 blocks). We then transformed the estimated angular velocities from the XYZ coordinate system to the geographic coordinate system (longitude, latitude, and rotation rate) in order to present the block rotations in the more familiar Euler pole form.

Table 2.3 and Figure 2.7 display the Euler poles, rotation rates, angular velocities, block velocity vectors, and associated uncertainties for our preferred block model. Angular velocities for small blocks or blocks without widespread site distributions have a large uncertainty in one component, typically the local vertical direction at the block in question. The nonlinear transformation between Cartesian and geographic coordinates means that the uncertainty regions for the Euler poles are distorted from ellipses into the shape of a great circle path when one axis of the Cartesian error ellipsoid is large. In addition, at the high latitudes considered in this study, a simple conversion of ellipse parameters can display a rotational bias in the error ellipse due to the different scales (in distance units) of the latitude and longitude axes. For these reasons, we show a Monte Carlo sampling of the uncertainty regions instead of the usual 95% confidence ellipses with the poles in Figure 2.7. We took 2500 random samples of a distribution with zero mean and covariance equal to the angular velocity covariance, added each sample to our estimated angular velocities, computed the corresponding Euler pole, and plotted the pole as a point on the map. The density of the points on the map corresponds to the probability distribution of the pole location. For blocks with large uncertainty regions for the poles, the predicted linear block velocities for points on the blocks will still have small uncertainties. This results from the strong correlation between the pole location and the angular speed.

We find the Yakutat block pole near the center of Hudson Bay in Canada, far from the block itself and consistent with the minimal rotation seen in the data along the northern coastal region of southeast Alaska. At the city of Yakutat, our model predicts a

block velocity of 50.3 ± 0.8 mm/a at an azimuth of N22.9 ± 0.6° W (Figure 2.8). For comparison, the model of *Plattner et al.* [2007] predicts a Pacific plate velocity of 50.9 mm/a at an azimuth of N14.6W at this location. Our estimate of the Yakutat block velocity is much closer to the velocity of the Pacific plate than the Yakutat estimate presented by *Fletcher and Freymueller* [1999], although a distinct difference in azimuth between the two tectonic blocks remains. At least part of the difference between the two geodetically derived estimates may be due to the fact that we removed the effects of GIA while the previous study did not. At YKTT, the Yakutat block GPS site used by *Fletcher and Freymueller* [1999], the predicted GIA motion is 3 mm/a, directed WSW. Removing this GIA estimate from the GPS data results in a more northerly directed velocity than that derived from the unadjusted data (Figure 2.A-2).

The Foothills block pole is the farthest away from southeast Alaska. Its location in the Atlantic Ocean results in block velocities that show little or no observable rotation along the block. This agrees well with the observed sub-parallel velocities on or near the Foothills block (Figure 2.4) and the linearity of the Fairweather fault in this region. Block velocity predictions display a similar magnitude but a more westerly azimuth than those for the Yakutat block.

Unlike the poles discussed above, the pole for the Nunatak block is located to the west of our study area, south of the Alaska Peninsula. Predicted block velocities have smaller magnitudes but almost identical azimuths to those on the Foothills block. The Eastern Denali block pole is located north of the Denali fault. Counter-clockwise rotation

about the pole results in N-NE directed block velocities that decrease in magnitude toward the north.

The Northern Cordillera pole is located to the east of the Queen Charlotte Islands. While the azimuth of the block velocity predictions is uniformly NE in our study area, the magnitudes steadily decrease towards the south until the zero point is reached at the pole. The Fairweather and Baranof block poles are both found on the Northern Cordillera block, with the Baranof pole located east and north of the Fairweather pole. Velocities along the Fairweather block show variation in both magnitude and azimuth, with magnitudes decreasing from north to south and azimuths displaying a clockwise rotation. The Baranof block displays block velocities that are much smaller and more uniform in magnitude than those on the Fairweather block. The azimuths, however, show a distinct clockwise rotation.

2.6.2 Relative Block Motions

Relative block motions resulting from our preferred model are shown in Figure 2.9. The majority of the relative motion between the Pacific plate and North America occurs along the Fairweather – Queen Charlotte system. Along the Fairweather fault, the motion is nearly pure translation while the Queen Charlotte fault displays varying degrees of transpression. Inboard of the Fairweather – Queen Charlotte system, the magnitude of the relative block motion remains fairly constant along the Eastern Denali and Coast Shear zone faults. The sense of motion, however, progresses from contraction and translation along the Eastern Denali fault to translation and dilatation along the Coast

Shear zone. The Duke River fault displays contraction between the Totschunda and Eastern Denali faults.

Relative motion between the Pacific plate and the Yakutat block results in 7.9 ± 0.9 mm/a of oblique convergence across the Transition fault. Summed together, the Boundary and Foothills faults accommodate ~ 6 mm/a of relative convergence as well as ~ 4 mm/a of relative translation between the coast and the Fairweather fault.

Lahr and Plafker [1980] suggested that relative block motion in this region may have recently begun shifting westward from the Duke River – Eastern Denali – Chatham Strait fault system to the Totschunda – Fairweather connector fault. Roughly double the amount of predicted relative block motion occurs on the Totschunda-Fairweather connector and Duke River faults than on the Eastern Denali and Coast Shear zone, so our results appear to support this idea.

Overall, the relative block motion map provides a picture of the current influence of the Yakutat block on the tectonics of southeast Alaska. In the northern part of the region, the complex combination of contraction, dilatation, and translation delineate the active collisional zone. Farther south, the relative motions indicate that the area has transformed from a collisional zone to a more translational boundary zone with some active deformation continuing inboard of the Queen Charlotte fault.

2.6.3 Goodness of Fit

Our block model provides a reasonable explanation for the observed GPS velocity field in southeast Alaska and the adjacent region of Canada, as shown by the residual vector plot in Figure 2.10. The reduced χ^2 (χ^2 per degree of freedom) for our preferred

model is 1.01, indicating that we have accounted for most of the effects of major structures and blocks in the region. 76% of the site-specific residual velocities are smaller than their 1-σ uncertainty estimates. The mean residual velocity magnitude is 1.1 mm/a while the mean data uncertainty magnitude is 1.7 mm/a. The residual velocities do not show a clear trend in any region.

2.7 Discussion

2.7.1 Slip Rate Estimates and Seismic Hazard

The only two faults without slip constraints in our model that have previous geologic and geodetic slip estimates are the Fairweather fault and the Dalton strand of the Eastern Denali fault. *Plafker et al.* [1978] reported an average dextral slip rate of 48 – 58 mm/a over the past 1,000 years for the Fairweather fault based on geologic studies, but the dates used were imprecise. The lower end of that estimate is more likely since Pacific-North America relative plate motion is only about 50 mm/a in this area. Using EDM networks across the fault, *Lisowski et al.* [1987] estimated a slip rate of 41 – 51 mm/a. The large range in this estimate results from a strong trade-off between slip rate and locking depth. *Fletcher and Freymueller* [2003] combined the GPS and EDM data to generate an estimate of about 46 mm/a.

Our preferred block model gives an average slip rate of 42.9 ± 0.9 mm/a along the Fairweather fault. The slip rate estimate varies along strike, from 36.6 ± 0.8 mm/a along the northern end of the fault to 41.5 ± 0.8 mm/a along the central segment of the fault to 45.8 ± 1.2 mm/a near Cross Sound. At the average slip rate, it would take 80 years to recover the 3.5 m of slip that occurred during the 1958 Fairweather fault event. Within

model uncertainties, the average slip rate given by our block model agrees with the geodetic estimate of *Fletcher and Freymueller* [2003].

In their kinematic model, *Lahr and Plafker* [1980] proposed a dextral slip rate of 2 mm/a along the Eastern Denali fault. Based on a combined profile of geodetic data across the Fairweather and Eastern Denali faults, *Fletcher and Freymueller* [2003] estimated that the Eastern Denali currently had a dextral slip rate of 3.8 mm/a. In these two studies, the region between the Fairweather and Eastern Denali faults moved northwestward roughly parallel to the Fairweather fault.

Our block model predicts an average of 1.5 ± 0.5 mm/a of dextral slip and 1.5 ± 0.6 mm/a of contraction along the Dalton strand of the Eastern Denali fault. This slip estimate is lower and much more transpressional than the previous geodetic estimate. The difference results from our rotating Fairweather block, which gives nearly fault normal motion in the vicinity of the Eastern Denali fault, and our substitution of the rotating Northern Cordillera block for fixed North America.

On the Boundary fault, our block model predicts an average of 3.6 ± 1.4 mm/a right-lateral strike-slip with an average 2.2 ± 1.5 mm/a of convergence across the northern end of the fault and 1.9 ± 1.2 mm/a of extension across the southern end of the fault. The change from convergence to extension occurs because of changes in the orientation of the model fault planes from north to south. Along the Foothills fault, our model predicts an average of 0.5 ± 1.6 mm/a of left-lateral strike-slip and 4.7 ± 0.9 mm/a of convergence. Slip estimates from our model are not directly comparable to the model of *Plafker and Thatcher* [2008] due to differences in fault geometry (see Section 2.4.2).

Regardless of fault geometry differences, we can conclude that our GPS-constrained block model allows low to moderate amounts of strain accumulation in the area suspected of generating the 1899 earthquake sequence.

Since it is offshore, direct measurements of the slip rate on the Queen Charlotte fault do not exist. In our block model, slip on the Queen Charlotte fault is defined by the relative motion between the Pacific plate and the Fairweather block. Our model predicts an average of 43.9 ± 0.6 mm/a fault parallel motion (right-lateral sense) and southward increasing convergence of 0.7 ± 0.4 mm/a (northern end of fault) to 15 ± 0.6 mm/a (north of the Queen Charlotte Islands). The increasing convergence is a result of the changing relative azimuth between the plate motion vectors and the model fault. At a rate of 43.9 mm/a, it would take about 130 years to recover the average slip of 5.8 m from the 1949 M_w8.1 Queen Charlotte Island event reported by *Nishenko and Jacob* [1990].

There is no consensus on slip rates and seismic hazard along the Transition fault among previously published estimates. *Fletcher and Freymueller* [2003] suggested that a freely slipping Transition fault could accommodate the ~20 mm/a of Fairweather fault normal motion implied by the GPS velocity at the city of Yakutat. In their model, the sense of slip on the Transition fault would be almost pure reverse motion. A suite of models presented by *Pavlis et al.* [2004] predicted 10 to 30 mm/a of dextral/oblique to pure convergent motion across the Transition fault. The kinematic model of *Lahr and Plafker* [1980] included 4 mm/a of dextral oblique motion across the Transition fault. Based on estimates of rupture length, focal depth, and moment of the 1973 mainshock, *Doser and Lomas* [2000] calculated a convergent slip rate of ~ 3 mm/a over the last

century for the segment of the Transiton fault offshore of Cross Sound. Our block model produces an average of 5.4 ± 1.1 mm/a of left-lateral strike-slip and 5.8 ± 0.9 mm/a of convergence across the Transition fault. Our fault normal estimate is quite close to those of both *Lahr and Plafker* [1980] and *Doser and Lomas* [2000], but it is substantially lower than the estimates of the previous model utilizing geodetic data. This difference is due to our inclusion of the Boundary and Foothills faults, which accommodate some of the relative convergence. The type of fault normal motion predicted by our model varies along the length of the Transition fault. We defined the northern and central sections of the fault as a vertical fault, so the fault normal estimate is represented by contraction. The southernmost section, around Cross Sound, was defined as a NE-dipping thrust fault, so the fault normal motion is translated into reverse slip.

2.7.2 Extent of Coherent Yakutat Block

Some studies have suggested that structures within the Yakutat block such as the Dangerous River zone are currently active (e.g. *Gipp* [2003]) and thus create a block boundary running across the lower part of Yakutat Bay. Our results do not support this hypothesis. The GPS velocity field (Figure 2.4) shows nearly identical velocities at sites on the Yakutat block, suggesting that no active structure exists between them. All of the GPS data from sites on the Yakutat block can be explained by a combination of strain accumulation on nearby faults to the east and a block rotation described by a single pole and rotation rate. Based on these results, we conclude that the Yakutat block behaves as a coherent block from Cross Sound to at least the eastern side of the Malaspina Glacier.

The eastern Yakutat block boundary in our model is the Foothills fault and is further west than the most oft-cited boundary, the Fairweather fault. GPS velocities between the coast and the Fairweather fault become progressively smaller and more westerly towards the east. This suggests that as the Yakutat block has jammed into the corner between the Pacific plate, southern Alaska, and western Canada, its eastern edge has undergone deformation and is now actively fragmenting. Such fragmentation would explain why the large earthquakes of the 1899 sequence occurred off of the major translational plate boundary formed by the Fairweather-Queen Charlotte system.

2.7.3 Significance of Nunatak and Foothills Blocks

The Nunatak and Foothills blocks are the two smallest blocks in our model and their size raises questions about whether they can truly be called rigid blocks, whether our interpretation could be based on transient strain, and whether these blocks are actually required by our block model.

The unlikelihood of detectable transient strain from the postseismic effects of the 1964, 1958, or 1899 earthquakes has been discussed in an earlier section. There remains the possibility that an under- or over-estimation of our predicted horizontal GIA effect could introduce a bias into the data, leading to spurious tectonic conclusions. To assess this possibility, we ran the alternate geometry model tests (see Section 2.4.2, Table 2.1, and 2.6) using datasets that had had predictions from the two end-member GIA model predictions applied instead of those of our best-fit model (see Section 2.3.4). Horizontal predictions from the two end-member GIA models differ substantially in both azimuth and direction from our best-fit GIA model (Figure 2.A-4), so the results from these tests

should reveal any inherent bias. The results displayed no significant effects; the statistical conclusions were the same as those drawn from the best-fit GIA model.

The inclusion of the Foothills and Nunatak blocks improved the fit between the block model and the data in the northern Fairweather fault region to degrees that met or exceeded the F-test criteria for significance at the 95% level (Table 2.1). Although this misfit reduction is important, it is the secondary reason for the inclusion of the blocks in our model. The main impetus is that without the two blocks, our model predicts ~ 20 mm/yr of contraction across the Transition fault. This amount of convergence would essentially place a subduction zone offshore southeast Alaska. As discussed earlier, offshore seismic data recently collected in the Gulf of Alaska [Christeson, personal communication, 2009] show no evidence for such a structure. Instead, the data suggest that the central section of the Transition fault is a near vertical structure.

There remains the question of whether the Nunatak and Foothills blocks actually deserve the designation of "block". In the process of developing our block model, we found that the amount of convergence accommodated between the coastal region and the Fairweather fault was more important than the precise locations and geometries of the faults. To fit the GPS data, the northern half of the Boundary fault did require specific fault plane dips and locking depths. Along the southern half, the GPS data only required the presence of a creeping boundary (represented by a fault with a 0 km locking depth – Table 2.2). The Foothills fault was assigned a vertical geometry to minimize misfit and contraction across Transition fault, but a moderately NE-dipping geometry did not radically increase the misfit. Angular velocities for the Nunatak and Foothills blocks

have large uncertainties (Table 2.3, Figure 2.7) and are the most sensitive of all the blocks to changes in fault geometries.

Given the complex nature of the Yakutat collisional corner, it is unlikely that the convergence is neatly or simply partitioned between the two faults presented here. Instead, the deformation could be distributed across the region on a number of structures whose exact geometries and slip rates are likely impossible to fully determine. Based on the evidence laid out in the previous paragraph, we propose that the Nunatak and Foothills blocks represent a deformation zone along the eastern edge of the Yakutat block rather than truly rigid blocks. Such a deformation zone would be realistic given the complicated tectonic environment of southeast Alaska and would accommodate the strain responsible for events like the 1899 earthquake sequence that occur off the main plate boundaries.

2.7.4 The Transition Fault Paradox

In our block model, the Transition fault accommodates oblique transpressive motion between the Pacific plate and the Yakutat block. The Transition fault is the obvious candidate for the Pacific-Yakutat boundary, but the amount and sense of present-day motion on the fault is controversial (see Section 2.2).

Our block model predicts an average of 5.4 ± 1.1 mm/a of left-lateral strike-slip and 5.8 ± 0.9 mm/a of contraction along the Transition fault. This amount of predicted convergence is far less than that suggested by *Fletcher and Freymueller* [1999], but more than might be expected in a dominantly strike-slip boundary. *Pavlis et al.* [2004] proposed that the rate of sedimentation in the Gulf of Alaska could mask evidence of

convergence. Extremely high sedimentation rates of 10-30 mm/a have been reported for the region [e.g *Jaeger et al.*, 1998; *Sheaf et al.*, 2003; *Hallet et al.*, 1996; *Koppes and Hallet*, 2002], implying that a substantial layer of sediment could accumulate over a relatively short time period. If our fairly modest amount of estimated convergence has been occurring over a comparably short time period, visible structures may not have developed yet. This could make our predicted motion along the Transition fault compatible with the available offshore seismic record.

Another possibility is that the Pacific-Yakutat relative motion is divided between strike-slip on the Transition fault and motion on another fault. Between 1987 and 1992, a sequence of M_w7+ earthquakes defined a north-south trending plane beginning near the junction of the Transition fault with the Pamplona zone and extending south into the Pacific plate [*Lahr et al.*, 1988; *Pegler and Das*, 1996]. The fault plane coincided with a preexisting weakness in the Pacific plate, magnetic anomaly 13. The two largest events of the sequence had right-lateral strike-slip mechanisms. Seismic reflection lines in the Gulf of Alaska [*Reece et al.*, 2009] suggest the presence of an active zone of faulting coincident with the north-south trending plane (Figure 2.1). The lack of offshore GPS sites or other constraints prevents us from including a Gulf of Alaska fault in our block model inversion. We can, however, estimate the slip rates on the a Gulf of Alaska fault and the Transition fault required to completely accommodate the Pacific-Yakutat relative motion through a simple linear combination solution. Assuming pure strike-slip motion on both faults and our predicted relative motion of 7.4 ± 1 mm/a east and 2.8 ± 1 mm/a north, we obtain estimates of 8.3 ± 1.0 mm/a of left-lateral slip on the Transition fault and

6.5 ± 1.1 mm/a of right-lateral slip on the Gulf of Alaska fault. The combination of left-lateral slip on the Transition fault and right-lateral slip on the Gulf of Alaska fault would require internal deformation of the block located between the two faults. A simple rotation of the block is not adequate.

The currently available data do not allow us to unequivocally confirm or disallow the sedimentation hypothesis, slip rates on a Gulf of Alaska fault and the Transition fault, or the amount of internal deformation between the two faults. But taken together, the sedimentation hypothesis and the Gulf of Alaska/Transition fault combination form reasonable end-member solutions to the problem of reconciling our predicted Pacific-Yakutat relative motion and the offshore seismic data.

2.7.5 Glacier Bay Structures

Our block model includes a boundary running through Tidal Inlet in Glacier Bay, dividing the Fairweather and Baranof blocks. We chose the location of this boundary, which we termed the Glacier Bay Partition (GBP), based on seismicity patterns and geologic observations of structural trends. The inclusion of the GBP improved the overall reduced χ^2 by ~ 10% and exceeded the F-test criteria for significance at the 99% level (Table 2.1).

Given that Glacier Bay is the current focus of considerable GIA effects due to ice loss since the LIA, there is a possibility that the signal we interpret as tectonic deformation could be an artifact introduced by our use of our best-fit GIA model. To test the dependence of our Glacier Bay conclusion on the GIA model predictions, we ran versions of our block inversion with and without the GBP using data that had the

predictions of the two end-member GIA models (see Section 2.3.4) applied instead of the best-fit model. For the case of the 50 km, 7 x 10^{18} Pa s GIA model, the version with the GBP had a reduced χ^2 value over 10% smaller than the version without and exceeded the F-test criteria for significance at the 99% level. In the case of the 85 km, 1.5 x 10^{18} Pa s GIA model, the version with the GBP had a reduced χ^2 value about 5% smaller than the version without and met the F-test criteria for significance at the 98% level. The relative independence of our GBP results from the choice of GIA models is not an unexpected result; while vertical GIA effects reach some of their maximum values in the Glacier Bay area, horizontal GIA effects are quite small there (Figure 2.A-3, Figure 2.3).

There remains the question of whether the GBP represents an actual discrete structure or if it instead serves as a proxy for distributed deformation. Our block model predicts 1.5 ± 0.4 mm/a of dextral slip and negligible fault-normal motion on the GBP. The Fairweather and Baranof block angular velocities predict very similar motions on their block boundary, but quite different motions away from the boundary. The available earthquake focal mechanisms do not show evidence of right-lateral strike-slip motion but instead indicate mixed strike-slip/thrust events. We found that the exact orientation of the Glacier Bay Partition was not crucial to the model results. Faults oriented 10°, 20°, and 30° from our model fault (Figure 2.5) did not cause significant changes in the misfit.

Based on these findings, we propose that the GBP represents internal deformation of the region comprising our Fairweather and Baranof blocks. The deformation north of Glacier Bay (Fairweather block) is strongly influenced by its proximity to the active collisional front between the Yakutat block and southern Alaska. Strain transferred from

the collision is forcing the Fairweather block to move to the northeast. The magnitude of the block velocities and their degree of easterly rotation decreases towards the south as distance from the collisional front in the St. Elias mountains increases (Figure 2.1; Figure 2.8). South of the GBP, block velocity magnitudes along the Baranof block are much smaller and more uniform than those observed to the north, but a distinct clockwise rotation is still evident. The rotation may be a result of the Baranof block being pulled along with the Fairweather block as the latter is pushed northeastward. The difference in deformation north and south of the GBP provides an explanation for the dearth of seismicity along the Chatham Strait fault and in the rest of the Baranof block (Figure 2.2) as well as the southward decreasing magnitudes in the GPS data and block motion predictions along the Northern Cordillera block.

2.7.6 Southern Boundary of the Baranof Block

Our block model does not define a unique southern boundary for the Baranof block. Our dataset is very sparse south of 58°N and includes no sites south of 55°N, so the model does not have adequate constraints in this region to exactly determine the boundary. We can, however, indirectly constrain the limits of the Baranof block.

Mazzotti et al. [2003] noted that the GPS velocities at sites in the Queen Charlotte Islands (Figure 2.1) had a significant margin-normal component. They found that the GPS data, in particular the margin-normal component, could not be explained by elastic deformation from the Queen Charlotte fault, even if a landward-dipping thrust was assumed to be part of the offshore plate boundary. This led them to suggest that the GPS data required active faulting between the Queen Charlotte Islands and stable North

America. We repeated their experiment, with the Baranof block in place of North America, to test whether the Queen Charlotte Islands lie on the Baranof block or whether the Baranof block motion modifies their conclusion. Our results were similar to those of *Mazzotti et al.* [2003] – the GPS velocities in the Queen Charlotte Islands could not be fully explained by a landward-dipping thrust fault accommodating the margin-normal component of the Pacific-Baranof block relative motion. This suggests that the Queen Charlotte Islands move independently of both North America and the Baranof block. Thus the Queen Charlotte Islands represent a different tectonic regime than the region to the north, likely due to the high degree of transpression along the offshore plate boundary. This conclusion agrees with the results of *Leonard et al.* [2008] and *Mazzotti et al.* [2008], who proposed that a coastal block including the Queen Charlotte Islands moves northerly at a rate of ~ 5 mm/a. In comparison, our model predicts ~ 4 mm/a of WSW-directed motion for the Baranof block in the Queen Charlotte Island region.

In the course of the above test, we found that one of the GPS sites in our southeast Alaska dataset likely belongs in the Queen Charlotte tectonic regime. After removing the elastic signal predicted by the fault model discussed above, the residual at this site (AIS1 on Annette Island, Figure 2.1) closely resembled the residuals seen at sites in the Queen Charlotte Islands. Based on this, we excluded AIS1 from our modeling and conclude that the Baranof block ends north of Annette Island (see dashed line in Figure 2.5).

2.7.7 The Northern Cordillera Block and Strain Transfer

As Figures 4 and S4 show, the GPS velocities at sites on the Northern Cordillera block are small, especially towards the south. This raises the question of whether the

Northern Cordillera block actually has distinct motion or is just part of the North American plate. The definition of the Northern Cordillera block is primarily based on GPS data, following *Mazzotti and Hyndman* [2002] who noted that a continuous GPS station at Whitehorse in the northern Canadian Cordillera showed about 5 mm/a of northeastward motion relative to North America. They suggested that the northeastward motion of the northern Cordillera block was due to strain transfer from the Yakutat block collision. Using a larger set of GPS sites, *Leonard et al.* [2008] documented a pattern of northeastward motion east of the Eastern Denali fault. Magnitudes of the velocities decreased from north to south. Our velocity field shows a similar pattern (Figure 2.4). As mentioned earlier, we see a decrease in velocity magnitude from ~ 6 mm/a north of the Duke River fault to less than 1 mm/a in the southeast of Chatham Strait. Previous studies [e.g. *Mazzotti and Hyndman*, 2002; *Leonard et al.*, 2008; *Mazzotti et al.*, 2008] have discussed the seismicity in the Richardson and Mackenzie Mountains to the north and northeast of our study area, which strongly suggests that the Northern Cordillera is moving northeasterly relative to stable North America.

We tested a block model with North America substituted for the Northern Cordillera to determine the importance of the latter block. Defining the region east of the Eastern Denali and Coast Shear zone faults to be North America increased overall misfit between the GPS data and our block model by about 15%, with the largest residuals concentrated near or east of the Eastern Denali fault. Several sites, including WHIT, a well-established continuous GPS station, had residuals approaching the 2-σ level. When compared to the North America version, the Northern Cordillera block model had an F

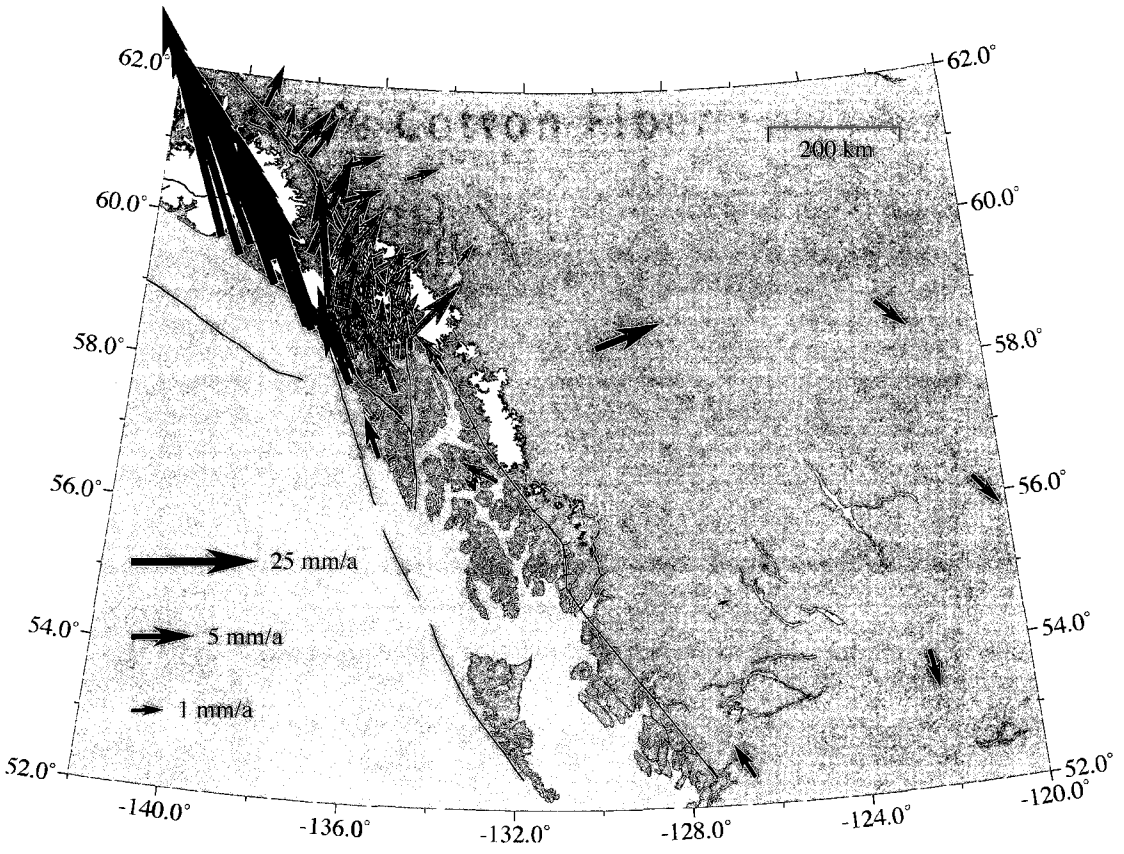

Figure 2.A-5. GPS velocities with GIA model predictions applied for southeast Alaska. Note the different scales for the velocities. Error ellipses are omitted for clarity.

Appendix 2.B Supplemental Tables

Table 2.B-1. GPS velocities for sites used in this study

Site[a]	E_Long[b]	N_Lat[c]	V_E[d]	V_N[e]	V_Up[f]	E_Sig[g]	N_Sig[h]	Up_Sig[i]
DEAS	-130.02887	58.43700	0.063	0.128	0.217	0.063	0.122	0.176
BLKP	-132.54409	56.59398	-0.412	0.189	0.544	0.113	0.147	0.289
LEV2	-133.09239	56.46566	-0.144	0.229	0.610	0.052	0.126	0.157
LEV1	-133.09278	56.46568	-0.215	0.154	0.844	0.042	0.124	0.151
ATLI	-133.71447	59.58948	0.205	0.347	0.881	0.059	0.121	0.175
TKHR	-134.01300	58.06755	-0.167	0.186	1.195	0.098	0.133	0.245
ANNX	-134.10051	58.31598	-0.146	0.086	1.608	0.092	0.129	0.201
5J22	-134.88981	58.57523	0.468	0.324	1.382	0.324	0.206	0.558
TDOG	-134.89978	58.38464	0.039	0.249	1.759	0.113	0.143	0.265
BRGT	-134.91064	58.59618	0.030	0.191	2.044	0.075	0.127	0.200
RAVE	-135.07598	58.40371	0.079	0.280	1.331	0.114	0.142	0.262
CLMB	-135.08428	58.24695	0.023	0.222	1.273	0.113	0.141	0.256
LSTR	-135.13001	58.50954	-0.029	0.127	2.061	0.078	0.128	0.200
STCK	-135.16032	58.64906	0.063	0.208	2.241	0.076	0.129	0.205
JA08	-135.17670	58.94741	0.173	0.364	2.264	0.147	0.144	0.316
CKOT	-135.22184	59.09118	0.204	0.395	1.858	0.161	0.144	0.316
WHIT	-135.22211	60.75051	0.132	0.195	0.229	0.043	0.117	0.157
ELD	-135.22232	58.97197	0.074	0.481	4.717	0.080	0.128	0.206
TENA	-135.22810	57.77115	-0.233	0.285	-0.562	0.077	0.130	0.201
WHB0	-135.23300	58.73260	0.247	0.182	2.216	0.103	0.131	0.234
CHKT	-135.27699	59.08026	0.193	0.394	1.977	0.112	0.140	0.262

T187	-135.32518	59.45599	0.358	0.490	0.804	0.220	0.219	0.270
FS32	-135.34696	59.14868	0.220	0.389	2.430	0.097	0.135	0.225
UDIG	-135.35868	58.28970	0.012	0.078	1.797	0.075	0.126	0.184
CAYO	-135.36499	58.92266	0.050	0.353	2.370	0.110	0.140	0.269
7SUN	-135.39746	59.04190	0.210	0.370	2.124	0.122	0.141	0.284
2437	-135.44464	58.41744	-0.183	0.081	2.020	0.075	0.127	0.192
2441	-135.46373	58.12489	-0.077	0.267	-1.751	0.121	0.144	0.282
2447	-135.48838	58.49645	0.076	0.010	2.591	0.106	0.136	0.232
HNSD	-135.53420	59.24810	0.219	0.551	2.367	0.069	0.125	0.188
BIS1	-135.53930	56.85449	-0.400	0.868	0.229	0.040	0.125	0.151
EA22	-135.64497	58.23192	0.082	0.108	1.869	0.079	0.130	0.212
2484	-135.65570	57.95744	-0.140	0.311	1.046	0.072	0.129	0.204
GUS2	-135.69748	58.41766	0.022	0.178	1.998	0.041	0.122	0.154
DMP2	-135.90720	58.24616	-0.135	0.212	2.088	0.066	0.128	0.195
BR39	-136.01446	58.73050	-0.027	0.235	2.617	0.055	0.124	0.170
DUKY	-136.02338	59.42399	0.362	0.494	2.939	0.106	0.150	0.289
GOOS	-136.03593	58.21122	-0.127	0.083	2.601	0.155	0.155	0.336
DAM	-136.04090	58.31914	-0.205	0.326	2.001	0.070	0.133	0.223
LAST	-136.14190	58.97887	0.047	0.423	3.306	0.077	0.126	0.191
ELSE	-136.15285	58.59350	-0.018	0.248	2.460	0.067	0.126	0.185
TLGT	-136.17599	58.74986	0.040	0.286	2.943	0.059	0.125	0.174
BAGO	-136.17964	59.05799	0.053	0.466	3.187	0.071	0.126	0.194
AID1	-136.25969	58.31778	-0.268	0.314	2.002	0.077	0.129	0.189
2629	-136.32661	58.26441	-0.244	0.282	2.098	0.076	0.127	0.196

MINE	-136.33823	58.00782	-0.424	0.525	1.540	0.064	0.127	0.187
508F	-136.36256	59.45039	0.040	0.639	1.863	0.191	0.170	0.414
DELT	-136.37786	58.36018	-0.198	0.361	2.100	0.052	0.124	0.165
ADZE	-136.38090	58.21219	-0.388	0.488	1.601	0.053	0.124	0.166
EX	-136.40509	58.26977	-0.334	0.463	1.660	0.105	0.140	0.283
BLUE	-136.42662	57.85222	-0.825	1.289	0.908	0.062	0.127	0.178
DACE	-136.43604	58.09134	-0.539	0.733	1.501	0.078	0.127	0.186
KNBG	-136.45710	58.61253	-0.124	0.405	2.273	0.058	0.125	0.176
BEUT	-136.46533	59.58148	0.184	0.747	3.085	0.067	0.125	0.190
DEPT	-136.48581	58.29991	-0.333	0.448	1.894	0.118	0.139	0.260
CINC	-136.49240	58.79782	-0.015	0.482	2.880	0.056	0.125	0.178
KAOS	-136.49980	58.42660	-0.222	0.502	2.168	0.141	0.142	0.288
TRTH	-136.63489	59.81952	0.248	0.699	1.870	0.059	0.123	0.178
CAPE	-136.64098	58.19767	-0.714	0.725	1.487	0.107	0.141	0.254
MART	-136.66526	58.89277	-0.006	0.551	3.111	0.081	0.128	0.210
NORM	-136.68720	58.27362	-0.816	0.606	1.531	0.088	0.135	0.245
PEEP	-136.73621	58.28622	-0.804	0.671	1.839	0.102	0.138	0.255
R205	-136.78826	58.90540	-0.112	0.696	2.740	0.068	0.127	0.186
OVAL	-136.79157	58.29275	-0.661	1.015	1.574	0.190	0.191	0.405
489F	-136.81893	59.97270	0.179	0.785	2.446	0.106	0.133	0.250
SARA	-136.93206	58.91843	-0.086	0.745	2.491	0.063	0.125	0.229
MARG	-137.02025	59.01742	-0.016	0.831	2.491	0.079	0.131	0.229
DEZA	-137.05421	60.37623	0.317	0.481	2.875	0.066	0.123	0.179
X7	-137.06285	60.85918	0.242	0.291	0.511	0.064	0.122	0.184

ANIT	-137.10027	58.86044	-0.374	0.995	3.458	0.116	0.138	0.252
ICE4	-137.48888	58.66888	-1.339	2.266	1.914	0.078	0.127	0.190
GILB	-137.51744	58.66329	-1.533	2.439	1.962	0.132	0.147	0.300
MIDB	-137.53464	58.57206	-1.727	2.928	1.296	0.229	0.189	0.460
LITU	-137.55579	58.65831	-1.652	2.600	2.177	0.071	0.127	0.190
CENO	-137.57322	58.63984	-1.790	2.858	1.771	0.054	0.125	0.177
2915	-137.62046	58.61563	-1.800	3.150	1.983	0.066	0.129	0.202
FROK	-137.63186	58.63993	-1.811	3.034	1.694	0.066	0.126	0.181
STRT	-137.67765	58.62526	-1.945	3.291	1.439	0.064	0.125	0.178
TATS	-137.73793	59.63044	0.184	1.113	2.931	0.063	0.125	0.185
WARR	-138.00837	58.92419	-1.898	3.246	1.650	0.097	0.135	0.234
MOTD	-138.04046	60.95774	0.158	0.537	1.099	0.200	0.200	0.190
NSLM	-138.49645	60.99267	0.229	0.573	1.152	0.056	0.121	0.181
NOVA	-138.55735	59.57353	-1.147	2.057	3.348	0.107	0.145	0.253
CANN	-138.63443	59.15519	-2.168	3.790	1.985	0.078	0.131	0.213
COMB	-138.63931	59.66985	-1.150	1.882	2.936	0.076	0.129	0.199
DEST	-138.72188	61.21692	-0.023	0.341	0.193	0.126	0.145	0.300
YAKU	-138.73328	59.49633	-1.786	3.042	3.280	0.060	0.125	0.177
FLAT	-138.86261	59.66928	-1.819	2.840	3.012	0.068	0.126	0.186
HIDD	-138.94546	59.70547	-1.938	3.068	2.911	0.063	0.125	0.181
MOSR	-138.99127	59.56797	-2.098	3.503	2.583	0.110	0.142	0.251
NQ4	-139.03155	59.82728	-1.648	2.800	2.434	0.084	0.130	0.213
NQ1	-139.13489	59.87933	-1.929	2.853	2.502	0.093	0.134	0.222
SITU	-139.40190	59.66639	-2.131	3.880	2.941	0.101	0.138	0.246

Y565	-139.44490	61.59267	0.079	0.295	0.611	0.087	0.126	0.200
YKTT	-139.64880	59.51074	-2.252	4.267	1.341	0.043	0.122	0.158
MLSP	-140.19775	59.72405	-2.019	4.417	1.228	0.076	0.130	0.220
SMTH	-127.18687	54.82375	-0.024	0.060	0.412	0.055	0.126	0.163
PRG6	-122.34039	53.91031	-0.017	-0.096	0.468	0.057	0.126	0.163
BLCL	-126.58925	52.38826	-0.093	0.148	0.684	0.059	0.132	0.165
FTSJ	-120.72985	56.24673	0.031	-0.079	0.437	0.057	0.119	0.163
FNEL	-122.57770	58.84187	0.034	-0.081	0.334	0.062	0.116	0.172

[a]"Site" = 4-letter name code for each GPS site.
[b]"E_Long" = degrees, longitude of site west of Greenwich.
[c]"N_Lat" = degrees, latitude of site, north of equator.
[d]"V_E" = cm/yr, east component of GPS data, not adjusted for effects of GIA, relative to North America.
[e]"V_N" = cm/yr, north component of GPS data, not adjusted for effects of GIA, relative to North America.
[f]"V_Up" = cm/yr, vertical component of GPS data, not adjusted for effects of GIA, relative to North America.
[g]"E_Sig" = cm/yr, 1-sigma uncertainty estimate for east component.
[h]"N_Sig" = cm/yr, 1-sigma uncertainty estimate for north component.
[i]"Up_Sig" = cm/yr, 1-sigma uncertainty estimate for vertical component.

Table 2.B-2. Glacial isostatic adjustment model predictions for sites used in this study

Site[a]	E_Long[b]	N_Lat[c]	E_GIA[d]	N_GIA[e]	Up_GIA[f]
DEAS	-130.02887	58.43700	-0.153	0.048	-0.301
BLKP	-132.54409	56.59398	-0.120	0.041	0.113
LEV2	-133.09239	56.46566	-0.131	0.059	-0.046
LEV1	-133.09278	56.46568	-0.131	0.059	-0.458
ATLI	-133.71447	59.58948	0.091	0.175	0.546
TKHR	-134.01300	58.06755	0.005	-0.084	0.928
ANNX	-134.10051	58.31598	0.061	-0.079	1.242
5J22	-134.88981	58.57523	0.091	-0.105	1.922
TDOG	-134.89978	58.38464	0.056	-0.153	1.661
BRGT	-134.91064	58.59618	0.094	-0.100	1.957
RAVE	-135.07598	58.40371	0.054	-0.166	1.758
CLMB	-135.08428	58.24695	0.027	-0.187	1.510
LSTR	-135.13001	58.50954	0.071	-0.147	1.937
STCK	-135.16032	58.64906	0.094	-0.103	2.131
JA08	-135.17670	58.94741	0.135	0.038	2.380
CKOT	-135.22184	59.09118	0.143	0.116	2.406
WHIT	-135.22211	60.75051	-0.112	0.104	-0.243
ELD	-135.22232	58.97197	0.135	0.050	2.422
TENA	-135.22810	57.77115	-0.040	-0.162	0.765
WHB0	-135.23300	58.73260	0.104	-0.074	2.264

CHKT	-135.27699	59.08026	0.139	0.109	2.452
T187	-135.32518	59.45599	0.123	0.288	2.071
FS32	-135.34696	59.14868	0.137	0.147	2.468
UDIG	-135.35868	58.28970	0.024	-0.207	1.678
CAYO	-135.36499	58.92266	0.121	0.015	2.508
7SUN	-135.39746	59.04190	0.129	0.084	2.561
2437	-135.44464	58.41744	0.041	-0.196	1.934
2441	-135.46373	58.12489	-0.004	-0.219	1.411
2447	-135.48838	58.49645	0.051	-0.182	2.086
HNSD	-135.53420	59.24810	0.121	0.203	2.521
BIS1	-135.53930	56.85449	-0.065	0.039	-0.198
EA22	-135.64497	58.23192	0.001	-0.232	1.665
2484	-135.65570	57.95744	-0.032	-0.215	1.141
GUS2	-135.69748	58.41766	0.023	-0.216	2.040
DMP2	-135.90720	58.24616	-0.019	-0.249	1.769
BR39	-136.01446	58.73050	0.028	-0.130	2.739
DUKY	-136.02338	59.42399	0.061	0.304	2.614
GOOS	-136.03593	58.21122	-0.036	-0.257	1.725
DAM	-136.04090	58.31914	-0.025	-0.254	1.961
LAST	-136.14190	58.97887	0.030	0.017	3.227
ELSE	-136.15285	58.59350	-0.010	-0.199	2.573
TLGT	-136.17599	58.74986	0.003	-0.129	2.859

BAGO	-136.17964	59.05799	0.029	0.072	3.273
AID1	-136.25969	58.31778	-0.054	-0.265	2.015
2629	-136.32661	58.26441	0.068	-0.270	1.902
MINE	-136.33823	58.00782	-0.082	-0.248	1.314
508F	-136.36256	59.45039	0.017	0.317	2.773
DELT	-136.37786	58.36018	-0.070	-0.266	2.151
ADZE	-136.38090	58.21219	-0.079	-0.271	1.785
EX	-136.40509	58.26977	-0.080	-0.273	1.927
BLUE	-136.42662	57.85222	-0.093	-0.216	0.991
DACE	-136.43604	58.09134	-0.092	-0.262	1.502
KNBG	-136.45710	58.61253	-0.066	-0.207	2.773
BEUT	-136.46533	59.58148	0.009	0.367	2.544
DEPT	-136.48581	58.29991	-0.091	-0.274	2.016
CINC	-136.49240	58.79782	-0.058	-0.118	3.073
KAOS	-136.49980	58.42660	-0.087	-0.261	2.392
TRTH	-136.63489	59.81952	0.001	0.415	2.048
CAPE	-136.64098	58.19767	-0.119	-0.275	1.756
MART	-136.66526	58.89277	-0.089	-0.066	3.245
NORM	-136.68720	58.27362	-0.127	-0.278	1.949
PEEP	-136.73621	58.28622	-0.135	-0.278	1.976
R205	-136.78826	58.90540	-0.117	-0.065	3.274
OVAL	-136.79157	58.29275	-0.146	-0.278	1.985

489F	-136.81893	59.97270	-0.004	0.420	1.752
SARA	-136.93206	58.91843	-0.148	-0.065	3.291
MARG	-137.02025	59.01742	-0.153	-0.006	3.348
DEZA	-137.05421	60.37623	-0.022	0.361	0.871
X7	-137.06285	60.85918	-0.079	0.181	-0.769
ANIT	-137.10027	58.86044	-0.192	-0.111	3.201
ICE4	-137.48888	58.66888	-0.286	-0.212	2.646
GILB	-137.51744	58.66329	-0.291	-0.214	2.610
MIDB	-137.53464	58.57206	-0.293	-0.236	2.381
LITU	-137.55579	58.65831	-0.297	-0.216	2.567
CENO	-137.57322	58.63984	-0.300	-0.221	2.510
2915	-137.62046	58.61563	-0.307	-0.227	2.414
FROK	-137.63186	58.63993	-0.309	-0.221	2.462
STRT	-137.67765	58.62526	-0.316	-0.224	2.390
TATS	-137.73793	59.63044	-0.086	0.274	2.928
WARR	-138.00837	58.92419	-0.340	-0.152	2.764
MOTD	-138.04046	60.95774	-0.051	0.191	-0.013
NSLM	-138.49645	60.99267	-0.039	0.196	0.039
NOVA	-138.55735	59.57353	-0.204	0.088	3.450
CANN	-138.63443	59.15519	-0.354	-0.143	2.591
COMB	-138.63931	59.66985	-0.178	0.134	3.420
DEST	-138.72188	61.21692	-0.048	0.096	-0.276

YAKU	-138.73328	59.49633	-0.257	0.004	3.431
FLAT	-138.86261	59.66928	-0.205	0.089	3.383
HIDD	-138.94546	59.70547	-0.199	0.097	3.266
MOSR	-138.99127	59.56797	-0.256	-0.002	3.140
NQ4	-139.03155	59.82728	-0.160	0.161	3.011
NQ1	-139.13489	59.87933	-0.148	0.175	2.884
SITU	-139.40190	59.66639	-0.241	-0.019	2.743
Y565	-139.44490	61.59267	-0.035	-0.057	-0.552
YKTT	-139.64880	59.51074	-0.291	-0.145	2.335
MLSP	-140.19775	59.72405	-0.225	-0.114	2.530
SMTH	-127.18687	54.82375	-0.057	0.051	0.056
PRG6	-122.34039	53.91031	-0.037	0.029	0.022
BLCL	-126.58925	52.38826	-0.032	0.040	0.026
FTSJ	-120.72985	56.24673	-0.045	0.022	0.023
FNEL	-122.57770	58.84187	-0.058	0.011	0.048

[a]"Site" = 4-letter name code for each GPS site.
[b]"E_Long" = degrees, longitude of site west of Greenwich.
[c]"N_Lat" = degrees, latitude of site, north of equator.
[d]"E_GIA" = cm/yr, east component of GIA model prediction.
[e]"N_GIA" = cm/yr, north component of GIA model prediction.
[f]"Up_GIA" = cm/yr, vertical component of GIA model prediction.

Table 2.B-3. Occupation histories for GPS sites

Site[a]	Num[b]	First_obs[c]	Last_obs[d]	Time_Span[e]	GPS_Observations_Per_Year[f]
YKTT	58	1992.47	2007.75	15.28	9,2,0,5,5,0,0,8,0,8,4,3,3,0,3,8,0
CANN	12	1999.47	2005.58	6.11	0,0,0,0,0,0,0,2,0,5,0,0,0,5,0,0,0
WARR	10	2001.65	2005.58	3.92	0,0,0,0,0,0,0,0,0,4,0,0,0,6,0,0,0
STRT	15	1999.56	2007.64	8.08	0,0,0,0,0,0,0,4,0,3,0,4,0,0,0,4,0
FROK	16	1999.57	2007.64	8.08	0,0,0,0,0,0,0,2,0,5,0,4,0,0,0,5,0
2915	12	1999.56	2007.64	8.08	0,0,0,0,0,0,0,3,0,3,0,3,0,0,0,3,0
CENO	22	1999.56	2007.64	8.08	0,0,0,0,0,0,0,6,0,6,0,5,0,0,0,5,0
LITU	16	1999.57	2007.64	8.08	0,0,0,0,0,0,0,2,0,4,0,5,0,0,0,5,0
MIDB	6	1999.56	2001.66	2.1	0,0,0,0,0,0,0,2,0,4,0,0,0,0,0,0,0
GILB	12	1999.56	2003.38	3.81	0,0,0,0,0,0,0,5,0,3,0,4,0,0,0,0,0
ICE4	15	1999.56	2007.64	8.08	0,0,0,0,0,0,0,3,0,3,0,5,0,0,0,4,0
MARG	15	2000.43	2007.57	7.13	0,0,0,0,0,0,0,0,2,0,0,6,4,0,0,3,0
SARA	23	1998.77	2007.57	8.8	0,0,0,0,0,0,1,0,5,3,0,6,5,0,0,3,0
OVAL	8	1998.58	2003.4	4.83	0,0,0,0,0,0,1,0,0,0,0,7,0,0,0,0,0
R205	24	2000.43	2007.57	7.14	0,0,0,0,0,0,0,0,2,0,0,6,5,0,4,7,0
PEEP	10	1998.57	2003.39	4.82	0,0,0,0,0,0,6,0,0,0,0,4,0,0,0,0,0
NORM	18	1998.57	2003.4	4.83	0,0,0,0,0,0,4,6,0,0,1,7,0,0,0,0,0
MART	28	1998.77	2007.57	8.8	0,0,0,0,0,0,2,0,3,3,5,7,4,0,0,4,0
CAPE	6	1998.58	2003.39	4.81	0,0,0,0,0,0,2,0,0,0,0,4,0,0,0,0,0
CINC	29	1998.77	2007.57	8.8	0,0,0,0,0,0,1,0,3,3,6,7,5,0,0,4,0
DEPT	10	1998.59	2003.4	4.81	0,0,0,0,0,0,3,0,3,0,0,4,0,0,0,0,0
KNBG	24	1998.77	2007.57	8.8	0,0,0,0,0,0,3,0,0,4,0,8,5,0,0,4,0
DACE	19	1998.55	2007.51	8.97	0,0,0,0,0,0,2,0,3,3,3,3,0,0,0,5,0
BLUE	18	1998.54	2007.51	8.97	0,0,0,0,0,0,2,0,2,4,4,3,0,0,0,3,0

EX	7	1998.59	2003.4	4.81	0,0,0,0,0,0,3,0,0,0,0,4,0,0,0,0,0
ADZE	19	1998.59	2007.51	8.92	0,0,0,0,0,0,3,2,6,0,0,4,0,0,0,4,0
DELT	45	1999.58	2007.59	8.01	0,0,0,0,0,0,0,17,3,0,12,5,0,3,0,5,0
508F	10	1999.4	2002.36	2.96	0,0,0,0,0,0,0,4,2,0,4,0,0,0,0,0,0
MINE	24	1998.54	2007.51	8.98	0,0,0,0,0,0,4,0,3,4,4,4,0,0,0,5,0
2629	32	1999.56	2007.58	8.02	0,0,0,0,0,0,0,9,7,0,7,6,0,0,0,3,0
AID1	12	1999.58	2007.58	8	0,0,0,0,0,0,0,1,5,0,0,3,0,0,0,3,0
BAGO	21	1998.71	2007.58	8.87	0,0,0,0,0,0,1,0,0,4,0,7,5,0,0,4,0
TLGT	22	1998.7	2007.58	8.87	0,0,0,0,0,0,2,0,4,3,0,3,5,0,0,5,0
ELSE	18	1998.71	2007.58	8.87	0,0,0,0,0,0,2,0,0,3,0,5,5,0,0,3,0
LAST	21	1998.71	2007.58	8.87	0,0,0,0,0,0,1,0,0,5,0,5,5,0,0,5,0
DAM	9	1998.61	2007.58	8.98	0,0,0,0,0,0,2,0,0,0,0,3,0,0,0,4,0
GOOS	11	1999.48	2003.41	3.93	0,0,0,0,0,0,0,2,4,0,0,5,0,0,0,0,0
BR39	23	1998.7	2007.58	8.87	0,0,0,0,0,0,4,0,0,4,0,8,4,0,0,3,0
DMP2	10	1999.48	2007.58	8.1	0,0,0,0,0,0,0,3,0,0,0,3,0,0,0,4,0
2484	9	1999.47	2007.59	8.12	0,0,0,0,0,0,0,2,0,0,0,4,0,0,0,3,0
EA22	11	1999.48	2007.59	8.11	0,0,0,0,0,0,0,2,0,0,0,6,0,0,0,3,0
BIS1	2659	2000.22	2007.99	7.77	0,0,0,0,0,0,0,0,281,362,291,274, 365,361,364,361,0
HNSD	25	2002.35	2007.47	5.11	0,0,0,0,0,0,0,0,0,0,6,5,3,2,4,5,0
2447	12	1999.47	2007.59	8.11	0,0,0,0,0,0,0,2,2,0,0,4,0,0,0,4,0
2441	7	1999.47	2003.43	3.96	0,0,0,0,0,0,0,3,0,0,0,4,0,0,0,0,0
2437	12	1999.47	2007.59	8.11	0,0,0,0,0,0,0,2,3,0,0,4,0,0,0,3,0
7SUN	7	1999.59	2003.59	4	0,0,0,0,0,0,0,3,0,0,0,4,0,0,0,0,0
CAYO	7	1999.59	2003.59	4	0,0,0,0,0,0,0,3,0,0,0,4,0,0,0,0,0
UDIG	13	1999.62	2007.59	7.96	0,0,0,0,0,0,0,3,4,0,0,3,0,0,0,3,0

FS32	16	2002.84	2007.47	4.63	0,0,0,0,0,0,0,0,0,0,5,0,0,2,3,6,0
T187	5	1993.35	1999.41	6.06	0,2,0,0,0,0,0,3,0,0,0,0,0,0,0,0,0
CHKT	7	1999.59	2003.59	3.99	0,0,0,0,0,0,0,3,0,0,0,4,0,0,0,0,0
WHB0	6	1999.61	2005.59	5.99	0,0,0,0,0,0,0,2,0,0,0,0,0,4,0,0,0
TENA	14	2000.62	2007.8	7.18	0,0,0,0,0,0,0,0,3,0,0,0,0,6,0,5,0
ELD	19	1997.62	2006.45	8.82	0,0,0,0,0,5,0,0,0,0,8,0,0,4,2,0,0
CKOT	7	1999.59	2003.59	3.99	0,0,0,0,0,0,0,3,0,0,0,4,0,0,0,0,0
JA08	8	1999.61	2003.59	3.99	0,0,0,0,0,0,0,3,0,0,0,5,0,0,0,0,0
STCK	7	1999.61	2005.59	5.99	0,0,0,0,0,0,0,4,0,0,0,0,0,3,0,0,0
LSTR	9	1999.62	2005.59	5.97	0,0,0,0,0,0,0,5,0,0,0,0,0,4,0,0,0
CLMB	7	1999.62	2003.43	3.8	0,0,0,0,0,0,0,4,0,0,0,3,0,0,0,0,0
RAVE	8	1999.62	2003.43	3.81	0,0,0,0,0,0,0,5,0,0,0,3,0,0,0,0,0
BRGT	13	1999.52	2007.41	7.89	0,0,0,0,0,0,0,3,0,3,0,4,0,0,0,3,0
TDOG	7	1999.63	2003.43	3.79	0,0,0,0,0,0,0,4,0,0,0,3,0,0,0,0,0
5J22	6	1999.59	2001.66	2.07	0,0,0,0,0,0,0,2,0,4,0,0,0,0,0,0,0
ANNX	14	1999.45	2005.65	6.21	0,0,0,0,0,0,0,6,0,0,0,0,0,8,0,0,0
TKHR	10	1999.45	2007.66	8.21	0,0,0,0,0,0,0,2,0,0,0,4,0,0,0,4,0
LEV1	2096	2001.47	2007.64	6.17	0,0,0,0,0,0,0,0,0,101,336,341, 365,363,359,231,0
LEV2	315	2001.47	2007.58	6.11	0,0,0,0,0,0,0,0,0,28,93,16,0,4, 40,134,0
BLKP	16	1993.36	2001.42	8.06	0,4,0,0,0,0,5,3,0,4,0,0,0,0,0,0,0
BEUT	27	2000.41	2007.46	7.06	0,0,0,0,0,0,0,0,2,0,3,5,6,5,3,3,0
TRTH	26	2000.41	2007.47	7.06	0,0,0,0,0,0,0,0,2,0,5,5,3,2,5,4,0
489F	20	1999.39	2005.74	6.35	0,0,0,0,0,0,0,1,3,0,4,5,3,4,0,0,0
TATS	15	1999.47	2007.72	8.25	0,0,0,0,0,0,0,2,0,5,0,5,0,0,0,3,0

ANIT	11	2003.61	2007.57	3.96	0,0,0,0,0,0,0,0,0,0,0,3,5,0,0,3,0
DEST	29	1999.38	2007.71	8.33	0,0,0,0,0,0,0,2,2,2,16,0,4,0,0,3,0
X7	28	1992.43	2006.72	14.29	4,0,0,0,0,0,0,3,1,2,8,0,3,2,5,0,0
NSLM	40	2000.4	2007.71	7.31	0,0,0,0,0,0,0,0,2,2,16,0,8,4,4,4,0
WHIT	4316	1993.45	2008.19	14.73	0,9,63,0,197,365,360,361,358, 358,353,364,365,365,364,365,69
Y565	32	1992.43	2007.72	15.29	7,0,0,0,0,0,0,0,0,0,12,0,3,2,0,8,0
SLRV	7	1999.39	2002.35	2.96	0,0,0,0,0,0,0,2,2,0,3,0,0,0,0,0,0
DEZA	42	2002.34	2007.71	5.37	0,0,0,0,0,0,0,0,0,0,4,5,7,7,9,10,0
ATLI	22	1999.5	2006.52	7.02	0,0,0,0,0,0,0,4,0,2,5,0,2,4,5,0,0
DEAS	17	1999.5	2006.53	7.03	0,0,0,0,0,0,0,6,0,0,5,0,0,0,6,0,0
SITU	14	2002.62	2006.62	3.99	0,0,0,0,0,0,0,0,0,0,3,3,3,0,5,0,0
KAOS	9	2003.41	2007.59	4.18	0,0,0,0,0,0,0,0,0,0,0,2,0,2,0,5,0
MOTD	28	2002.34	2007.71	5.37	0,0,0,0,0,0,0,0,0,0,6,0,7,7,4,4,0
DUKY	17	2002.36	2007.47	5.11	0,0,0,0,0,0,0,0,0,0,1,6,3,2,0,5,0
GUS2	3731	1997.06	2008.19	11.13	0,0,0,0,0,340,274,295,336,362, 273,334,365,362,359,362,69
MLSP	7	2001.43	2007.75	6.32	0,0,0,0,0,0,0,0,0,4,0,0,0,0,0,3,0
NOVA	5	1992.48	2003.59	11.11	2,0,0,0,0,0,0,0,0,0,0,3,0,0,0,0,0
COMB	8	1992.48	2003.59	11.11	2,0,0,0,0,0,0,3,0,0,0,3,0,0,0,0,0
HIDD	12	1992.47	2003.59	11.12	5,0,0,0,0,0,0,3,0,0,0,4,0,0,0,0,0
FLAT	6	1992.47	2003.59	11.12	3,0,0,0,0,0,0,0,0,0,0,3,0,0,0,0,0
NQ1	3	1992.48	2003.59	11.1	2,0,0,0,0,0,0,0,0,0,0,1,0,0,0,0,0
NQ4	4	1992.48	2003.59	11.11	3,0,0,0,0,0,0,0,0,0,0,1,0,0,0,0,0
YAKU	8	1992.47	2003.59	11.12	5,0,0,0,0,0,0,0,0,0,0,3,0,0,0,0,0
MOSR	4	1992.48	2003.59	11.1	2,0,0,0,0,0,0,0,0,0,0,2,0,0,0,0,0

BLCL	24	1999.46	2006.52	7.06	0,0,0,0,0,0,0,7,0,0,9,0,0,0,8,0,0
PRG6	27	1999.47	2006.53	7.06	0,0,0,0,0,0,0,10,0,0,9,0,0,0,8,0,0
FTSJ	24	1999.48	2006.54	7.05	0,0,0,0,0,0,0,11,0,0,6,0,0,0,7,0,0
SMTH	18	1999.49	2006.52	7.03	0,0,0,0,0,0,0,9,0,0,4,0,0,0,5,0,0
FNEL	20	1999.5	2006.54	7.04	0,0,0,0,0,0,0,7,0,0,6,0,0,0,7,0,0

[a]"Site" = 4-letter name code for each GPS site.
[b]"Num" = total number of observations at each site.
[c]"First_obs" = Date of first observations, in decimal year.
[d]"Last_obs" = Data of last observations, in decimal year.
[e]"Time_span" = time span between first and last observations, in years.
[f]"GPS_Observations_Per_Year" = number of observations at a site each year. Year order is 1992,1993,1994,1995,1996,1997,1998,1999,2000,2001,2002,2003,2004,2005,2006,2007,2008.

Chapter 3

Active Tectonics of the St. Elias Orogen, Alaska, Observed with GPS Measurements[2]

3.1 Abstract

We use data from campaign and continuous sites in southeast and south central Alaska to constrain a regional tectonic block model for the St. Elias orogen. Active tectonic deformation in the orogen is dominated by the effects of the collision of the Yakutat block with southern Alaska. Our results indicate that ~ 37 mm/yr of convergence is accommodated along a relatively narrow belt of N- to NW-dipping thrust faults in the eastern half of the orogen. Near the Bering Glacier, the collisional thrust fault regime transitions into a broad, northwest dipping decollement as the Yakutat block begins to subduct beneath the counterclockwise-rotating Elias block. The location of this transition aligns with the Gulf of Alaska shear zone, implying that the Pacific plate is fragmenting in response to the Yakutat collision. Our model indicates that the Bering Glacier region is undergoing internal deformation and could correspond to the final stage of offscraping and accretion of sediments from the Yakutat block prior to subduction. Predicted block motions at the western edge of the orogen suggest that the crust is laterally escaping along the Aleutian forearc.

---

[2] Elliott, J., J. T. Freymueller, C. F. Larsen, and S. P. S. Gulick, Active Tectonics of the St. Elias Orogen, Alaska, Observed with GPS Measurements, prepared for submission to the Journal of Geophysical Research – Solid Earth.

3.2 Introduction

The St. Elias orogen lies within the transitional zone between a dominantly transform plate margin in southeast Alaska and subduction along the Aleutian megathrust. This transition is greatly complicated by the collision of the Yakutat block with southern Alaska. The convoluted tectonics of the region has given rise to some of the most spectacular topography on earth. Over half of North America's 25 highest peaks are in the orogen. The fourth highest peak, 5489-meter high Mount St. Elias, sits just 25 km from the fjords of Icy Bay.

Until recently, little was known about the details of the region's tectonics. Several studies [e.g. *Lahr and Plafker*, 1980; *Perez and Jacob*, 1980; *Savage and Lisowski*, 1988; *Estabrook et al.*, 1992] suggested models for the basic regional tectonic framework or focused on segments of the orogen, but available data were sparse and major questions remained about the distribution of relative motion and location of active structures, the present-day deformation front between the Yakutat block and southern Alaska, and how far the effects of the collision extended.

In this paper, we present a new GPS data set and use these data to develop a tectonic block model for the St. Elias orogen. Block modeling divides areas with complex and varied deformation patterns into a group of blocks whose motion can be calculated. This method allows us to generate a self-consistent kinematic model that accounts for both long term tectonic block motion and the transient effects of interseismic strain accumulation on the block-bounding faults [e.g. *McCaffrey*, 2002; *Meade and*

Hager, 2005]. The block modeling approach avoids inconsistencies that can arise when slip rates or block velocities are estimated individually.

The new GPS data set and the block modeling technique permit us to examine the active tectonics of the St. Elias orogen as a whole, integrated system. Using angular velocities estimated by the block model, we calculate relative rates of motion between the blocks and evaluate what these mean in terms of strain distribution within the orogen and seismic hazard. We pay particular attention to the transition between the collisional tectonic regime and subduction as well as to strain transfer at the western and eastern edges of the orogen.

3.3 Tectonic Setting

The driving force behind the superlative relief of the St. Elias orogen is the collision between the Yakutat block and southern Alaska. The Yakutat block is a wedge shaped allochthonous terrane (Figure 3.1) that originated during the mid-Cenozoic as part of the present-day Pacific Northwest [*Bruns*, 1983] or British Columbia and southeastern Alaska [*Plafker et al.*, 1994] and migrated north along the Fairweather – Queen Charlotte transform system. It arrived by and has been colliding with southern Alaska since at least the late Miocene, roughly 6 – 10 Mya [*Lagoe et al.*, 1993; *Ferris et al.*, 2003]. The Chugach – St. Elias fault is the suture between the Yakutat block and southern Alaska [*Pavlis et al.*, 2004] and has been assumed to be the active block boundary [*Plafker et al.*, 1978; *Perez and Jacob*, 1980; *Plafker et al.*, 1994]. Recent thermochronology work suggests that the Chugach – St. Elias fault has been inactive for ~ 1 My and that the active block boundary has shifted to the south and east over time [*Berger et al.*, 2008].

The Yakutat block has a velocity of 50.3 ± 0.8 mm/yr towards N22.9 ± 0.6°W, implying that ~ 4 cm/yr of convergence between the Yakutat block and southern Alaska occurs across the St. Elias orogen [*Elliott et al.*, 2010].

Consisting of a broad region of folds and thrust faults, the Pamplona fault zone lies offshore the St. Elias orogen. A number of studies have suggested that the Pamplona fault zone and its onshore continuation mark the present-day deformation front between the Yakutat block and southern Alaska [*Perez and Jacob*, 1980; *Horner*, 1983; *Estabrook et al.*, 1992; *Worthington et al.*, 2008]. Based on offshore seismic reflection data, *Worthington et al.* [2010] concluded that the active structures in the Pamplona fault zone have migrated southeast since the Pliocene and that only a small percentage of the Yakutat – Southern Alaska relative motion is accommodated offshore.

Onshore, a W-E to SW-NE trending fold-and-thrust belt is actively deforming the region between the coast and the Chugach – St. Elias fault [*Bruhn et al.*, 2004; *Wallace,* 2008]. The width of the fold-and-thrust belt narrows towards the east, where it becomes obscured beneath the ice cover of the Malaspina Glacier but presumably connects with the Fairweather fault and the Yakutat foreland faults [*Bruhn et al.*, 2004; *Chapman et al.*, in prep.]. *Bruhn et al.* [2004] suggested that the fold-and-thrust belt ends at the Bering Glacier, where a postulated north-south trending structure marks the beginning of a complex zone of superimposed folding in the western orogen.

Seismicity within the St. Elias orogen is concentrated in three main areas: the Icy Bay/St. Elias region, the Bering Glacier region, and the Copper River region (Figure 3.2). Within the Icy Bay cluster there are several smaller trends of seismicity. One runs across

Icy Bay, another is centered over the Chaix Hills and Mount St. Elias area, and two small concentrations lie over the center and eastern edge of the Malaspina Glacier. Seismicity between the major clusters and directly offshore the St. Elias orogen is relatively sparse. Several M6+ earthquakes have occurred in the St. Elias region during the past century. In September 1899, a series of M8 earthquakes caused significant uplift, landslides, and glacier changes in the area between Prince William Sound and southeast Alaska. *Tarr and Martin* [1912] reported that the first event, on September 4, resulted in uplift of the coast near Yakataga. A relocation by *Doser* [2006] places the earthquake in the Pamplona zone. The Pamplona zone was also the locus of an M6.7 earthquake in 1970. This event was preceded and followed by several M5 – 6 earthquakes with predominately N – NW dipping thrust mechanisms [*Doser et al.*, 1997]. At the end of February, 1979, a M_w7.4 earthquake occurred northwest of Mount St. Elias. The event, usually assumed to have ruptured the Pacific – North America plate interface [*Stephens et al.*, 1980; *Estabrook et al.*, 1992], had a depth of ~ 15 km [N. Ruppert, personal communication, 2011]. The complex pattern of aftershocks from the event propagated southeast and apparently migrated up to shallower depths along the Malaspina fault before spreading across the Malaspina Glacier [*Estabrook et al.*, 1992]. Between 1987 and 1992, a sequence of M7+ earthquakes defined a north-south trending plane in the Gulf of Alaska that coincided with a pre-existing weakness in the Pacific plate, magnetic anomaly 13 [*Lahr et al.*, 1988; *Pegler and Das*, 1996]. The M9.2 1964 Prince William Sound rupture plane extended into the western St. Elias orogen. *Shennan et al.* [2009] found evidence of coseismic uplift from that event as far east as the southern end of the Bering Glacier

and suggested that past megathrust events may have ruptured even further east to Icy Bay.

3.4 GPS Data and Analysis

3.4.1 Data Set

We use GPS data collected at 65 sites in southeast and southcentral Alaska (Table 3.1). One site, in the town of Cordova, is a continuously running GPS site. The other 64 are campaign sites. The majority of the sites were newly established in 2005 and 2006 as part of the ST. Elias Erosion/Tectonics Project (STEEP). In order to have a consistent timeseries for this data set, we only use data collected during the 2005 – 2009 time period, even for the small number of sites that have a longer timeseries. The only exceptions to this rule were two sites (BREM and TOYU) that did not have an adequate amount of data from the 2005 – 2009 time period. Each campaign site had at least two and as many as five annual visits. Table 3.2 details the occupation histories of sites used in this study.

3.4.2 Data Processing and Velocity Estimation

We used the GIPSY/OASIS GOA4 software developed by the Jet Propulsion Laboratory (JPL) [*Zumberge et al.,* 1997] to analyze the GPS data presented here. Data from each day were analyzed separately to create daily loosely constrained frame-free solutions. We used JPL's fiducial-free orbits and transformed these daily solutions into the International Terrestrial Reference Frame 2000 (ITRF2000, realization IGFb00). The daily solutions were combined in a linear least squares inversion to estimate velocities at each GPS site.

We used ITRF2000 rather than more recent versions of ITRF because of our need to express our solutions in a North America-fixed frame. We consider the estimate of *Sella et al.* [2007] to be the most reliable determination of the motion of North America as it is based on substantially more data than any other estimate and considers the effects of glacial isostatic adjustment. The estimate of *Sella et al.* [2007] is based on ITRF2000 (IGSb00) and should not be used with later versions of ITRF due to differences between the frames.

In our uncertainty estimates, we included uncertainties in the definition of the North America fixed frame and in the geocenter stability of ITRF in addition to the formal errors in site velocities. The ITRF2000 and ITRF2005 frames differ by a ~ 1.8 mm/yr geocenter translation along the spin axis (Z axis). At the latitudes considered in this study, the geocenter difference results in a velocity difference of ~ 1 mm/yr in the north component and ~ 1 mm/yr in the vertical component. *Argus* [2007] and *Kogan and Steblov* [2008] both attempted to estimate a geocenter correction to ITRF. The result of *Argus* [2007] lies between ITRF2000 and ITRF2005 while the result of *Kogan and Steblov* [2008] is closer to ITRF2000. Since we do not know if either frame is correct, we augmented the velocity uncertainties by 1.8 mm/yr in the Z component, which reduces the weight given to the north and vertical velocity components accordingly. The impact of any small bias in the velocities on the model results in this paper is very small. The use of ITRF2000 in both our velocity estimates and our choice of reference plate pole minimizes the bias. Further details about the processing, velocity estimation, and

the augmentation of uncertainties due to possible systematic errors can be found in the work of *Freymueller et al.* [2008].

3.4.3 Postseismic Effects

The location of the St. Elias orogen results in a considerable postseismic effect from the 2002 M7.9 Denali fault earthquake at our sites. A robust postseismic deformation model for our study area is not available as published models [*Pollitz*, 2005; *Freed et al.*, 2006; *Johnson et al.*, 2009] significantly over-predict the postseismic effect in the far field. In order to make a first-order correction for the postseismic effect, we develop an empirical estimate based on an interpolation of the differences between pre- and post-earthquake velocities in the region. We selected a group of sites that had reliable velocities before the earthquake and during the time period of our data set (Figure 3.3), subtracted the post-earthquake velocity from the pre-earthquake velocity, and performed a linear interpolation of the results to produce an estimate of the postseismic effect at each of our sites. Since our data set includes velocities spanning different time periods (2005 – 2008, 2005 – 2009, 2006 – 2008, 2006 – 2009), we calculated estimates using post-earthquake velocities covering each of those periods. The estimate spanning the appropriate time interval was then subtracted from each of the velocities. Magnitudes of our estimated postseismic effects range from 11 mm/yr at the northern edge of our study area to 7 mm/yr near the terminus of the Bering Glacier to 5 mm/yr at Icy Bay. Figure 3.3 shows our postseismic estimates at the sites used in this study. To account for uncertainties in the interpolation we added 10% of the magnitude of the postseismic estimate to our formal error estimate for each site.

We also correct for the postseismic effects of the 1964 M9.2 Prince William Sound earthquake using the model of *Suito and Freymueller* [2009]. The eastern end of the 1964 rupture overlaps with the western half of our study area. Model postseismic estimates range from 9 mm/yr in the northwest corner of our study area to ~ 2 mm/yr north of the Bering Glacier to ~ 1 mm/yr at Icy Bay.

We do not correct for the possible postseismic effects of the 1958 M7.9 Fairweather fault earthquake, the 1899 earthquake sequence, or the M_w7.4 1979 St. Elias earthquake. *Elliott et al.* [2010] demonstrated that due to a short Maxwell relaxation time of ~ 2 years for southeast Alaska, any postseismic effects from the former two earthquakes, even of considerable initial magnitude, would have decayed into negligible amounts by the present day. Although more recent and within our region of study, the M_s7.1 St. Elias earthquake is an order of magnitude smaller than the other earthquakes. Given the Maxwell relaxation time, present day postseismic effects should be insignificant. Corroborating this, *Savage and Lisowski* [1986] found that strain rates derived from Geodolite measurements taken in 1979, 1980, 1982, and 1984 within the Yakataga region were consistent with a constant rate of strain accumulation over the 1979 – 1984 time period. If significant postseismic deformation resulted from the 1979 event, the measured strain rate would be expected to show variations during the five years following the earthquake.

3.4.4 Glacial Isostatic Adjustment

The Gulf of Alaska coast has experienced substantial ice volume loss since the end of the Little Ice Age (LIA) in the late 1700s [*Motyka*, 2003; *Larsen et al.*, 2004]. The glacial isostatic adjustment (GIA) resulting from this ice loss causes one of the fastest ongoing isostatic uplift measured, second only to uplift observed in the southern Patagonian icefields [*Larsen et al.*, 2005; *Dietrich et al.*, 2010]. In southeast Alaska, centers of peak uplift in Glacier Bay and the Yakutat ice field show rates of more than 30 mm/yr [*Larsen et al.*, 2005]. GIA models predict that horizontal deformation associated with the ice loss in southeast Alaska produces rates exceeding 7 mm/yr [*Elliott et al.*, 2010]. Tectonic interpretation of the regional tectonic field relies on first accounting for the horizontal signal from the GIA. In the St. Elias orogen, the GIA signal results from a combination of ice load changes within Glacier Bay since the end of the LIA and past and ongoing load changes across southern Alaskan and adjoining Canadian ice cover. We apply an adjustment for the GIA signal using the model presented in *Elliott et al.* [2010], which is an updated version of the model of *Larsen et al.* [2005].

3.4.5 Velocity Field

Figure 3.4 shows the GPS velocities in the St. Elias orogen with the predicted horizontal GIA motion and postseismic corrections removed. The velocity field displays several distinctive trends. Across Icy Bay (Figure 3.5), the velocities rotate counterclockwise and decrease in magnitude by nearly 10 mm/yr over a distance of only 10 km. Moving north from Icy Bay, decreasing velocity magnitudes imply a strong strain gradient in the eastern half of the orogen. Around the vicinity of the Bering Glacier,

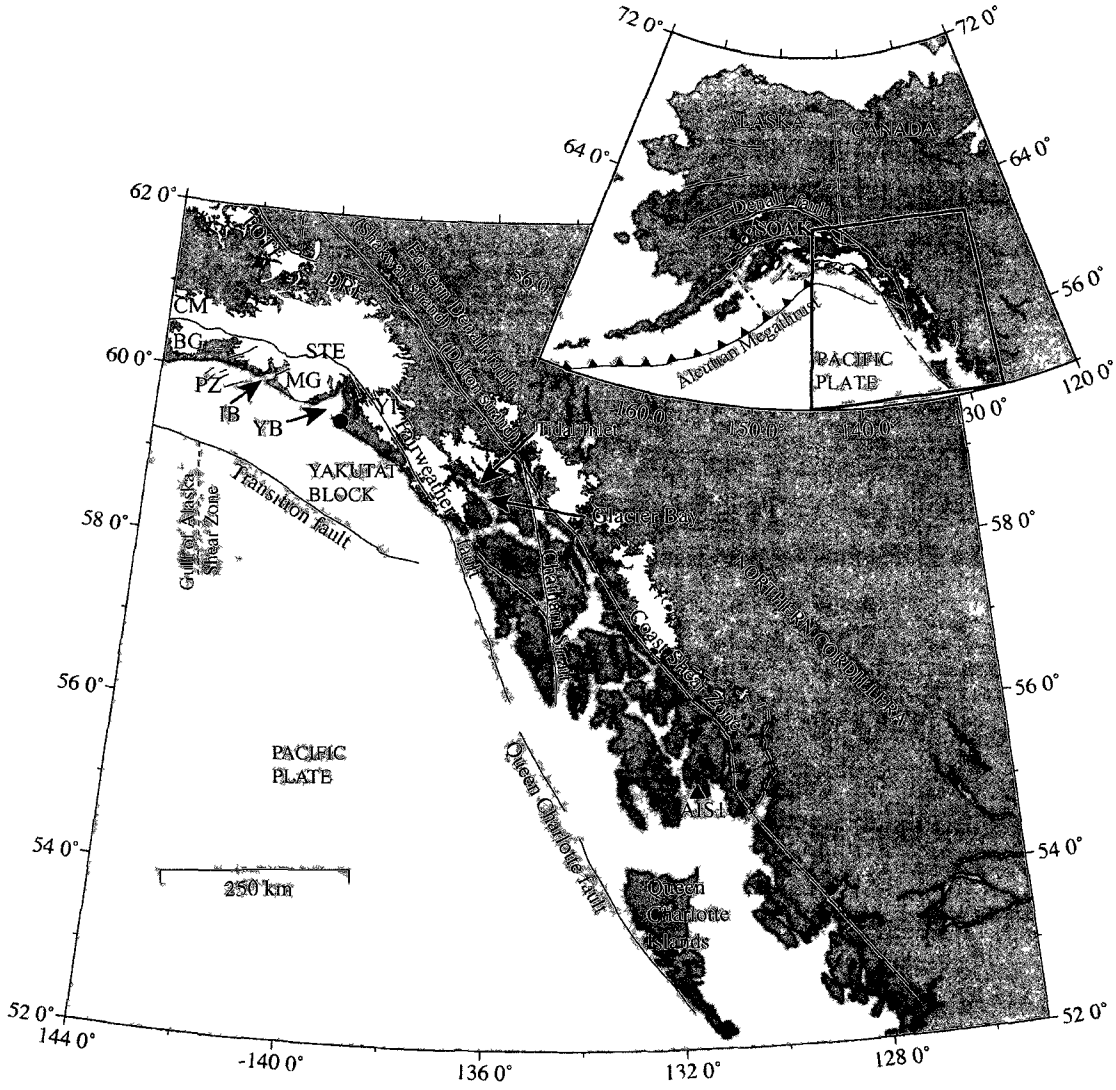

Figure 2.1 Tectonic setting of southeast Alaska Green dot marks the city of Yakutat Abbreviations are CM, Chugach Mountains, BG, Bering Glacier, PZ, Pamplona fault zone, IB, Icy Bay, MG, Malaspina Glacier, STE, St. Elias Mountains, YB, Yakutat Bay, YI, Yakutat icefield, DRF, Duke River fault, TOTF, Totschunda fault, and SOAK, Southern Alaska block. Faults are based on *Plafker et al* [1994b], *Brew and Ford* [1998], and *Pegler and Das* [1996].

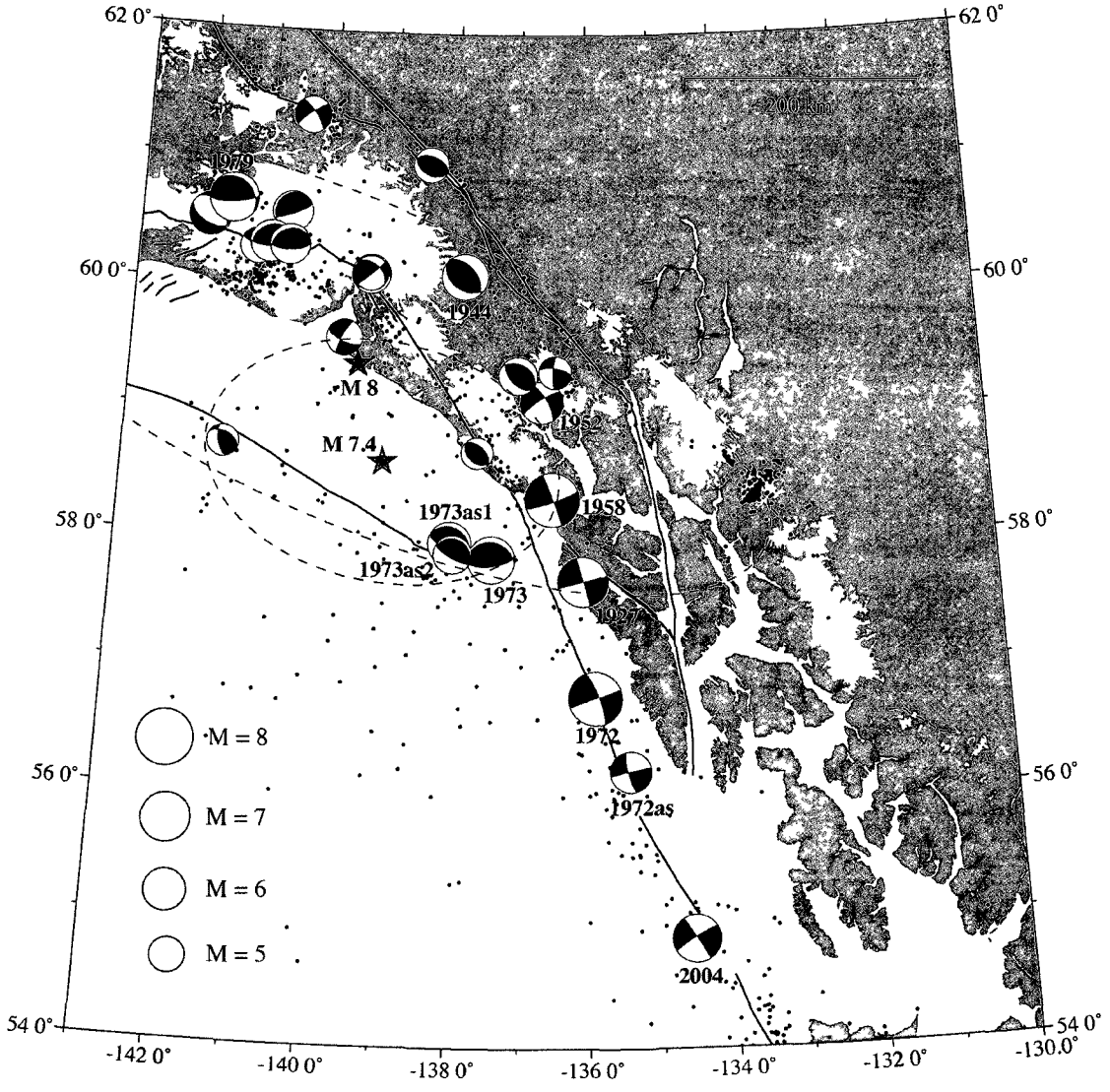

Figure 2.2. Seismicity in southeastern Alaska and the adjacent region of Canada. Seismic events with $M \geq 3$ are shoen by dots and are taken from the AEIC catalog. Available focal mechanisms are shown for $M \geq 4.5$ events. $M \geq 6$ events and their aftershocks are labeled with the year in which they occurred. Focal mechanisms are from *Doser and Lomas* [2000] and the AEIC database [N. Ruppert, personal communication, 2008]. Stars indicate the epicenters of the 10 September 1899 events as relocated by *Doser* [2006]. Dashed ellipses indicate uncertainty limits for the relocations. The cluster of earthquakes located east of -134° is not of tectonic origin; they are either glacial or groundwater related events [*Wolf et al.*, 1997].

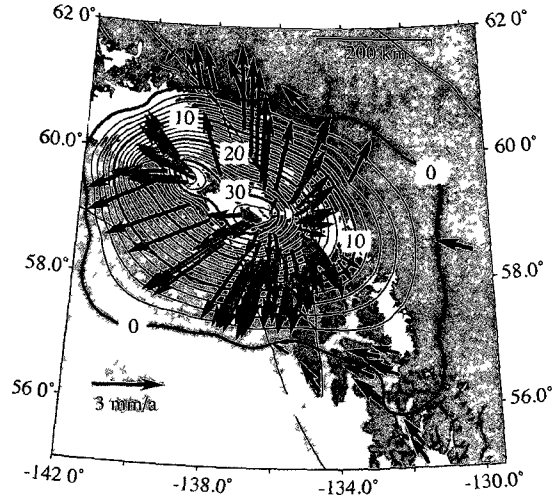

Figure 2.3. Glacial isostatic adjustment model predictions for southeast Alaska. Vectors show the horizontal motion while the contours show the vertical motion. Contour label units are mm/yr. Figure 2.A-1 shows a larger version of this figure.

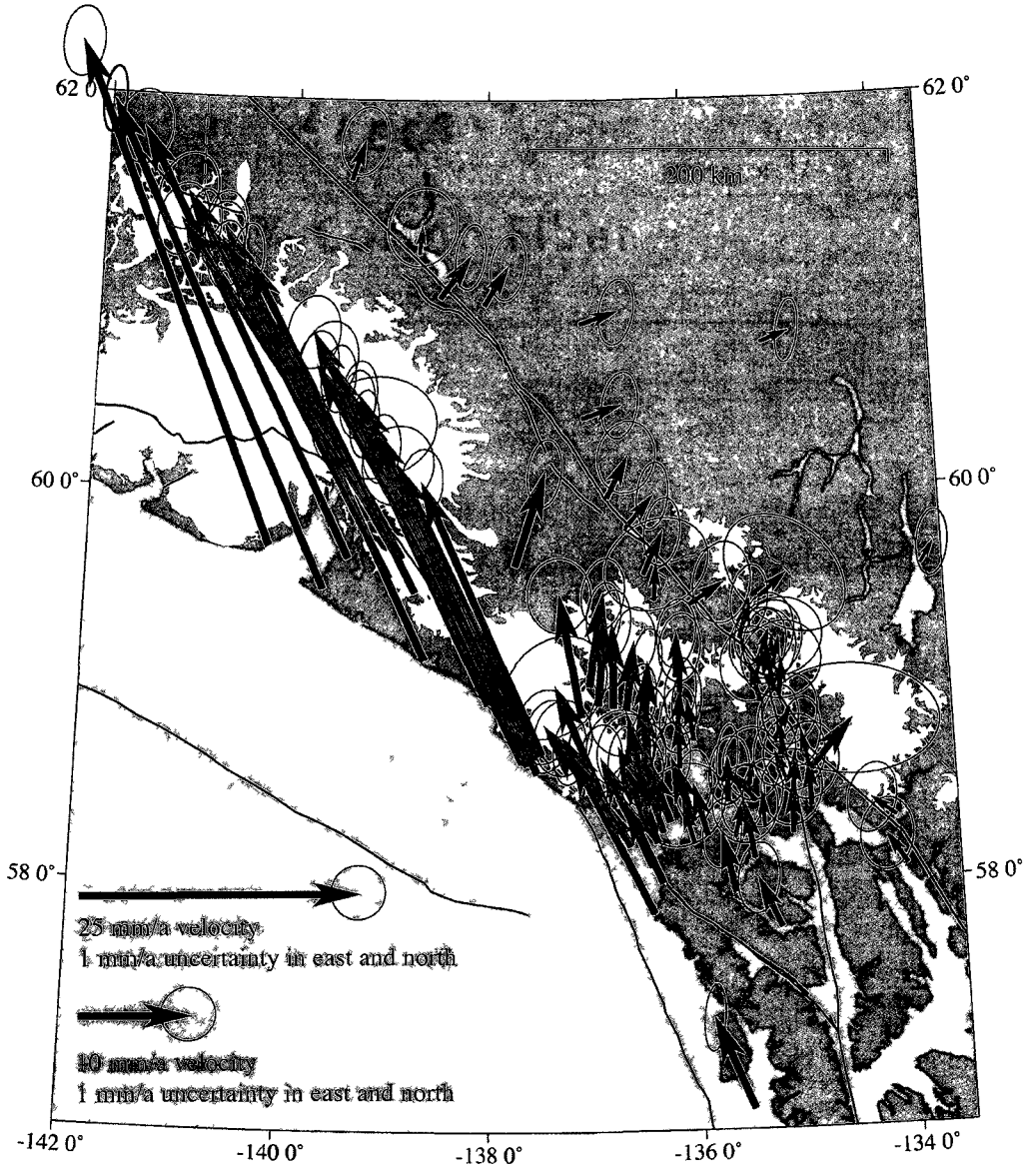

Figure 2.4. GPS velocities with GIA model predictions applied for southeast Alaska and the adjacent portion of the Canadian Cordillera. Figure 2.A-5 shows all of the GPS velocities used in our model.

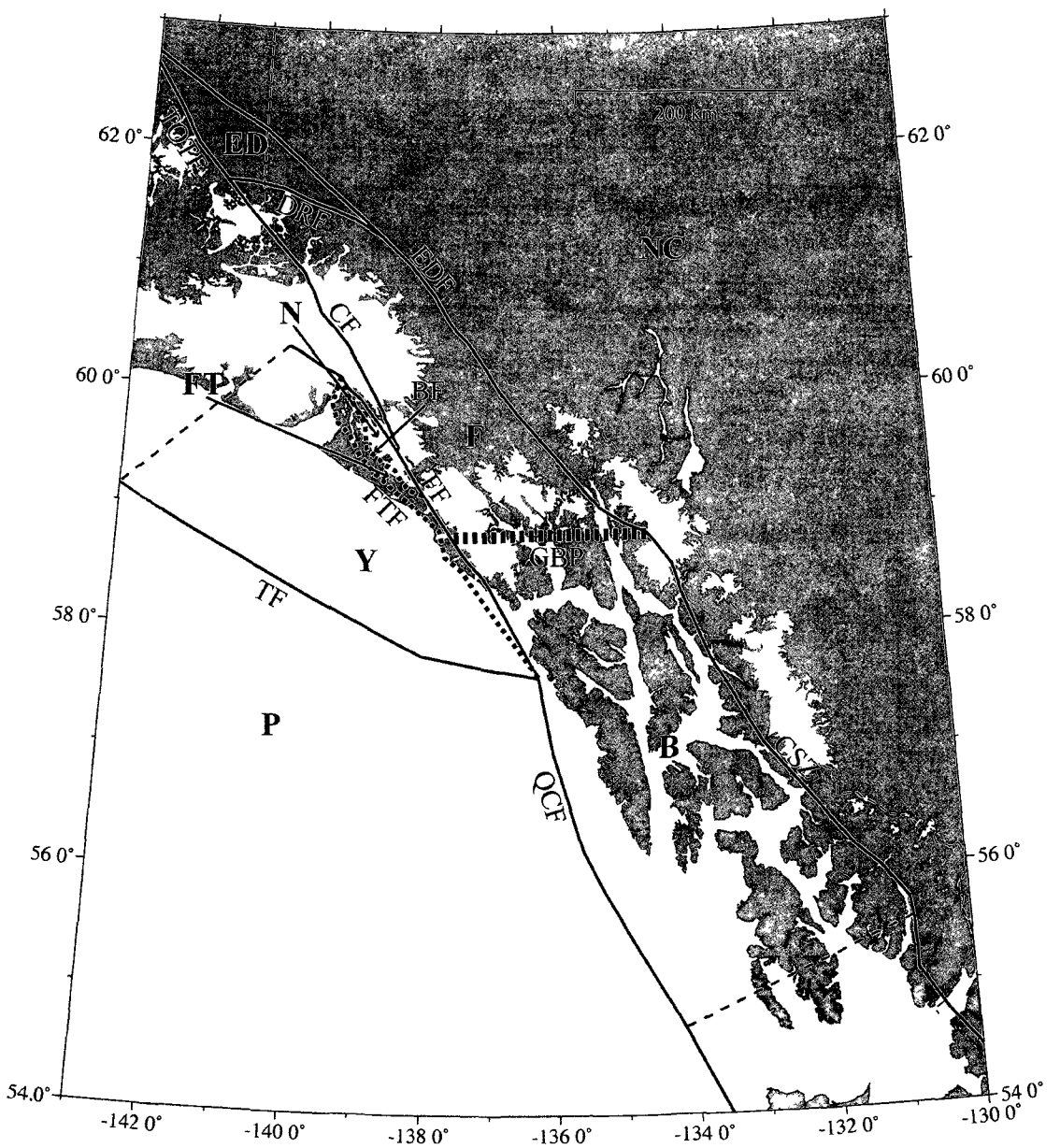

Figure 2.5. Blocks and bounding faults used in our southeast Alaska inversion model. Bold type indicates a block and regular type indicates a bounding fault. Abbreviations are: P, Pacific Plate; Y, Yakutat block; FT, Foothills block; N, Nunatak block; F, Fairweather block; B, Baranof block; ED, Eastern Denali block; NC, Northern Cordillera block; TF, Transition fault; FTF, Foothills fault; BF, Boundary fault; FF, Fairweather fault; QCF, Queen Charlotte fault; CSZ, Coastal Shear zone; GBP, Glacier Bay Partition; EDF, Eastern Denali fault; DRF, Duke River fault; CF, Totschunda – Totschunda Connector fault; and TOTF, Totschunda fault.

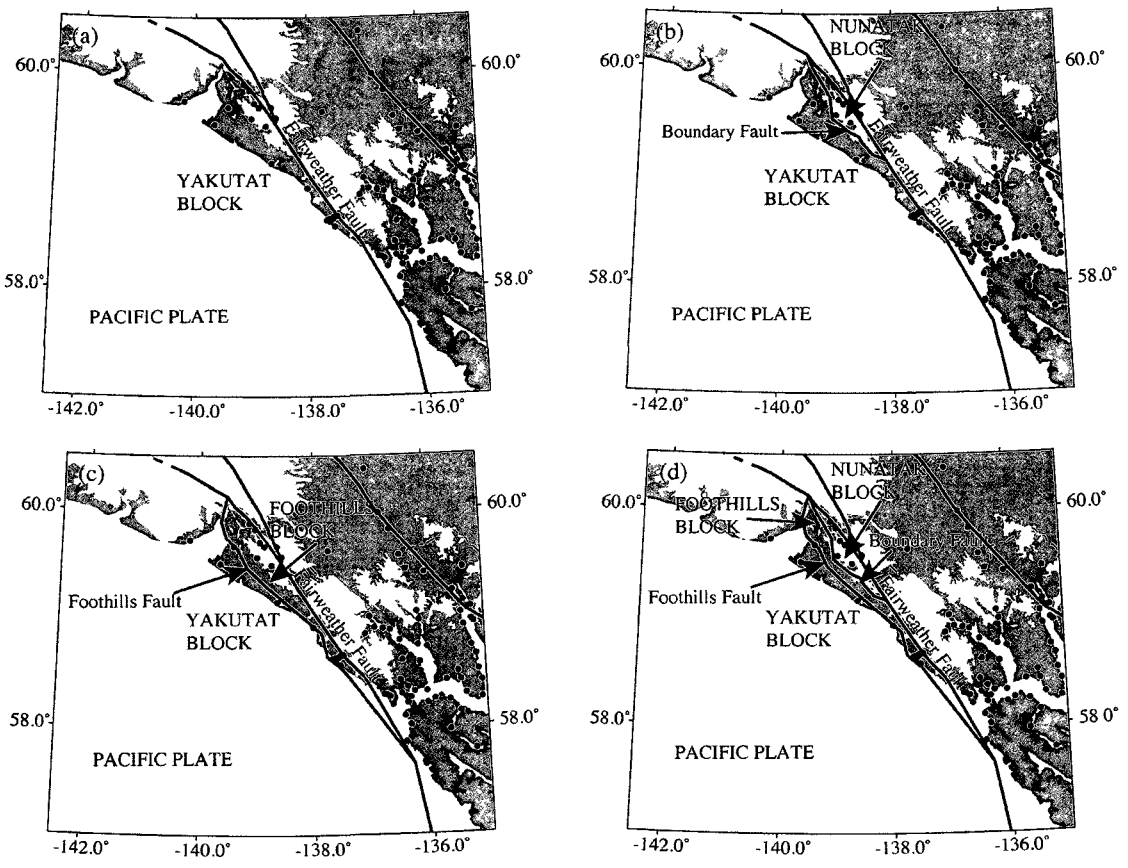

Figure 2.6. Alternate model geometries without an offshore fault. Black dots show locations of GPS sites. (a). Model without any faults west of the Fairweather fault. (b). Model including the Boundary fault and resulting Nunatak block. (c). Model including the Foothills fault and the resulting Foothills block. (d). Model including the Boundary fault and the Nunatak block as well as the Foothills fault and the Foothills block.

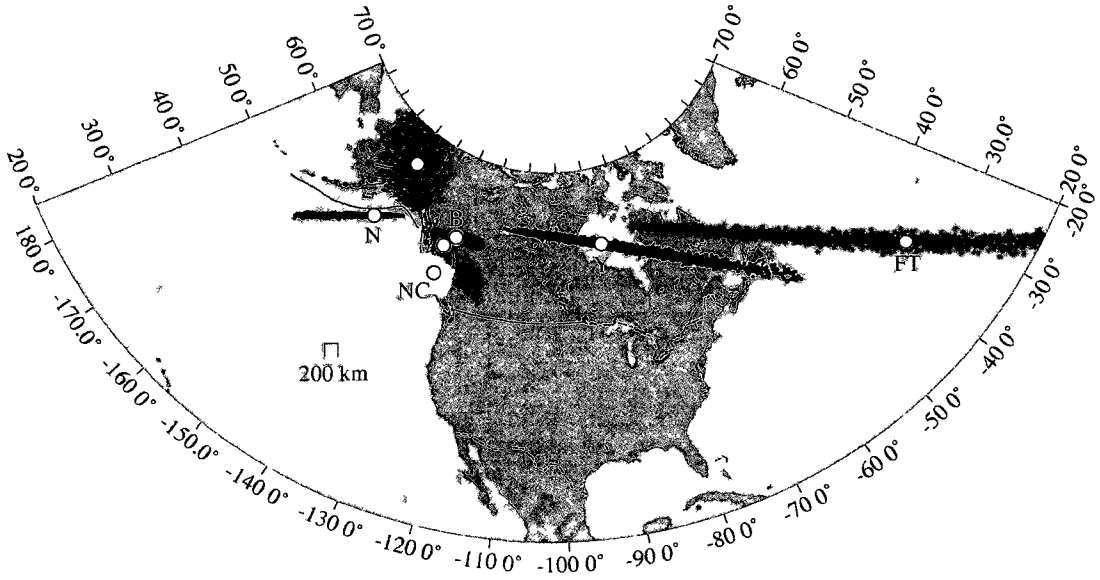

Figure 2.7. Euler poles and uncertainty clouds for our preferred block model. Uncertainty clouds represent the 95% confidence regions for the pole locations. Abbreviations are: ED, Eastern Denali block; N, Nunatak block; F, Fairweather block; B, Baranof block; NC, Northern Cordillera block; Y, Yakutat block; FT, Foothills block. Table 2.3 lists the locations, rotation rates, angular velocities, and angular velocity covariances for the poles. All poles are relative to the North America definition of *Sella et al.* [2007].

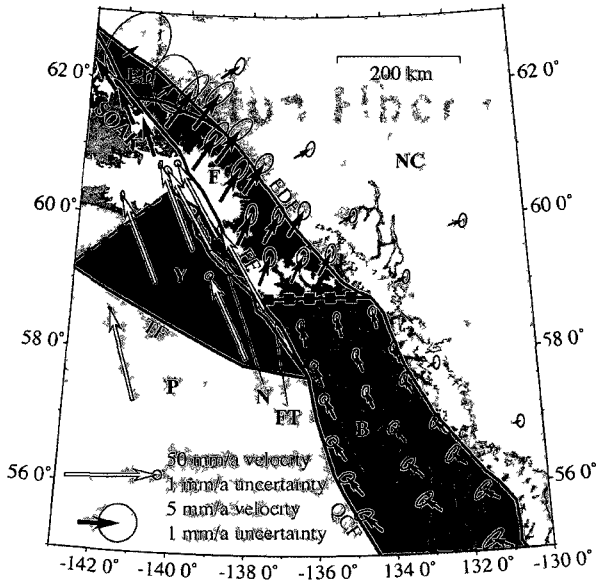

Figure 2.8. Block velocity predictions for selected points in southeast Alaska and adjacent Canada. Note the different vector scales used. All block velocity predictions are relative to the North America definition of *Sella et al.* [2007]. SOAK predictions are derived from *Fletcher* [2002]. Pacific plate velocity is derived from *Plattner et. al.* [2007]. Abbreviations are: P, Pacific plate; Y, Yakutat block; N, Nunatak block; FT, Foothills block; B, Baranof block; F, Fairweather block; NC, Northern Cordillera block; ED, Eastern Denali block; SOAK, Southern Alaska block; QCF, Queen Charlotte fault; FF, Fairweather fault; TF, Transition fault; EDF, Eastern Denali fault.

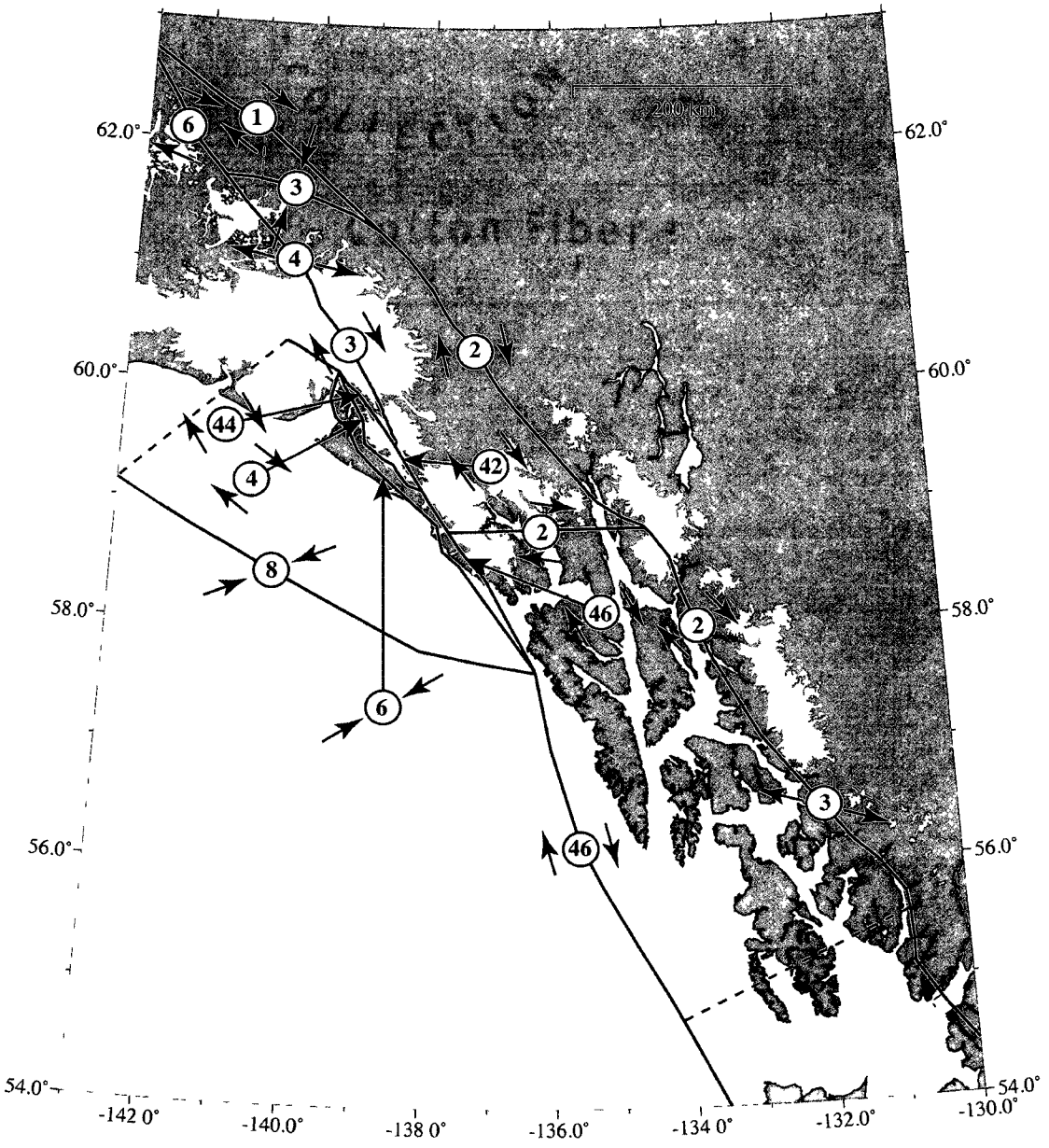

Figure 2.9. Relative block motion predictions for southeast Alaska. Dark gray arrows indicate sense of relative motion while the circled numbers give the magnitude of the motion in mm/a rounded to the nearest whole number. For faults with offset numbers, long black arrows connect the circled number to the appropriate fault.

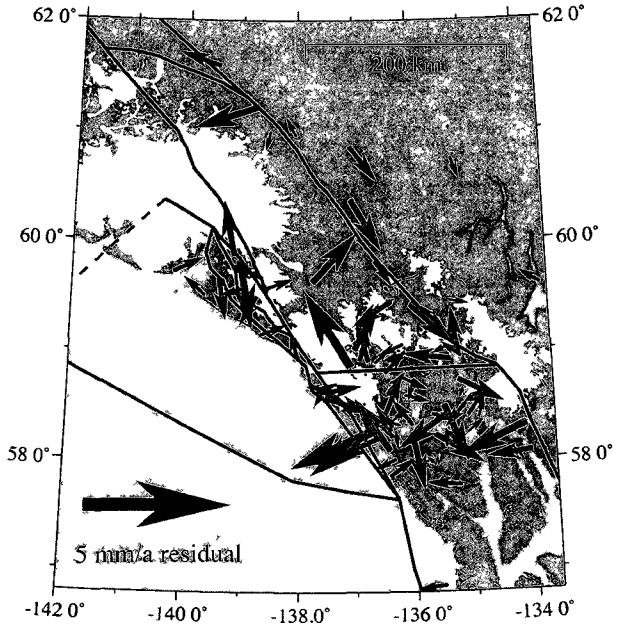

Figure 2.10. Velocity residuals between data and block model predictions. Residuals are only shown for sites whose data uncertainties are less than 1.5 times the average uncertainty. 76% of the sites have residuals smaller than their 1-σ uncertainty estimates.

Table 2.1. F-test results for alternative model fault geometries

Model Geometry	χ_r^2	WRSS	P[a]	DoF[b]	F[c]	F calculated relative to
1 No Transition fault, no Foothills or Boundary faults	3 6	652 11	18	188	N/A	N/A
2 No Transition fault, no Foothills fault, with Boundary fault	3 26	563 58	21	185	9 58	Model 1
3 No Transition fault, with Foothills fault, no Boundary fault	2 01	361 41	21	185	49 07	Model 1
4 No Transition fault, with Foothills and Boundary faults	1 8	321 24	24	182	7 5	Model 3
5 With Transition fault, no Foothills or Boundary faults	1 54	281 2	21	185	80 46	Model 1
6 With Transition fault, no Foothills fault, with Boundary fault	1 48	267 58	24	182	3 05	Model 5
7 With Transition fault, with Foothills fault, no Boundary fault	1 16	216 75	24	182	17 84	Model 5
8 With Transition fault, Foothills, and Boundary faults	1 09	201 3	27	179	4 52	Model 7
9 With Transition, Foothills, Boundary and GB faults	1 01	184 6	30	176	5 27	Model 8

[a] Number of model Parameters
[b] Degrees of Freedom
[c] F value of 2.13 indicates a 90% significance level, F value of 2.66 indicates a 95% significance level, F value of 3.9 indicates a 99% significance level

Table 2.2. Fault geometry parameters for block model[a]

Fault Segment	Fault Width (km)	Locking Depth (km)	Dip (°)
Totschunda	10	10	90
Duke River	10	10	90
Eastern Denali (Shakwak)	10	10	90
Eastern Denali (Dalton)	10	10	90
Malaspina Fairweather (60 3°-60°)	5	5	90
Upper Fairweather (60°-60 5°)	8	7 6	79, to NE
Central Fairweather (59 5°-57 65°)	10	10	90
Queen Charlotte	10	10	90
Transition (northern and central)	8	8	90
Transition (Cross Sound area)	28 5	26 8	70, to NE
Coast Shear zone	10	10	90
Boundary (60 1°-59 9°)	8	8	90
Boundary (59 9°-59 7°)	8	7 96	85, to NE
Boundary (59 7°-59 5°)	8	8	90
Boundary (59 5°-59)	0	0	90
Foothills (60 1-58 86°)	8	8	90
Foothills (58 86°-58 5°)	12	12	90
Foothills (58 5°-57 65°)	4	4 98	85, to NE
Glacier Bay	8	8	90

[a]Parameter values are averages for the fault segment. Fault width is measured in the downdip direction.

Table 2.3. Poles, rotation rates, and angular velocities

Block	Lat. (°N)	Long. (°E)	Rate (°/Ma)	Omega (X, Y, Z) (10^{-3} rad/Ma)	Omega Covariance (xx, xy, xz, yy, yz, zz) (10^{-6} rad/Ma^2)
Yakutat	59 47	-87 82	-1 04 ± 0 32	-0 35, 9 25, -15 69	5 70, 5 05, -12 73, 4 49, -11 30, 28 47
Fairweather	57 11	-129 89	-0 44 ± 0 18	2 70, 3 23, -6 52	1 44, 1 34, -3 32, 1 26, -3 10, 7 63
Baranof	58 8	-127 67	-0 32 ± 0 09	1 77, 2 29, -4 79	0 35, 0 35, -0 79, 0 34, -0 77, 1 75
N Cordillera	52 99	-129 58	-0 14 ± 0 03	0 95, 1 15, -1 98	0 03, 0 03, -0 07, 0 04, -0 08, 0 17
Nunatak	55 94	-148 9	3 74 ± 1 72	-31 31, -18 89, 54 09	134 02, 117 31, -301 97, 102 71, -264 35, 680 44
Foothills	34 79	-35 08	-0 48 ± 0 13	-5 67, 3 98, -4 82	5 00, 4 36, -10 87, 3 84, -9 54, 23 79
E Denali	65 15	-148 22	-0 30 ± 0 55	-1 85, -1 14, 4 69	12 99, 10 87, -30 42, 9 19, -25 59, 71 51

Appendix 2.A Supplemental Figures

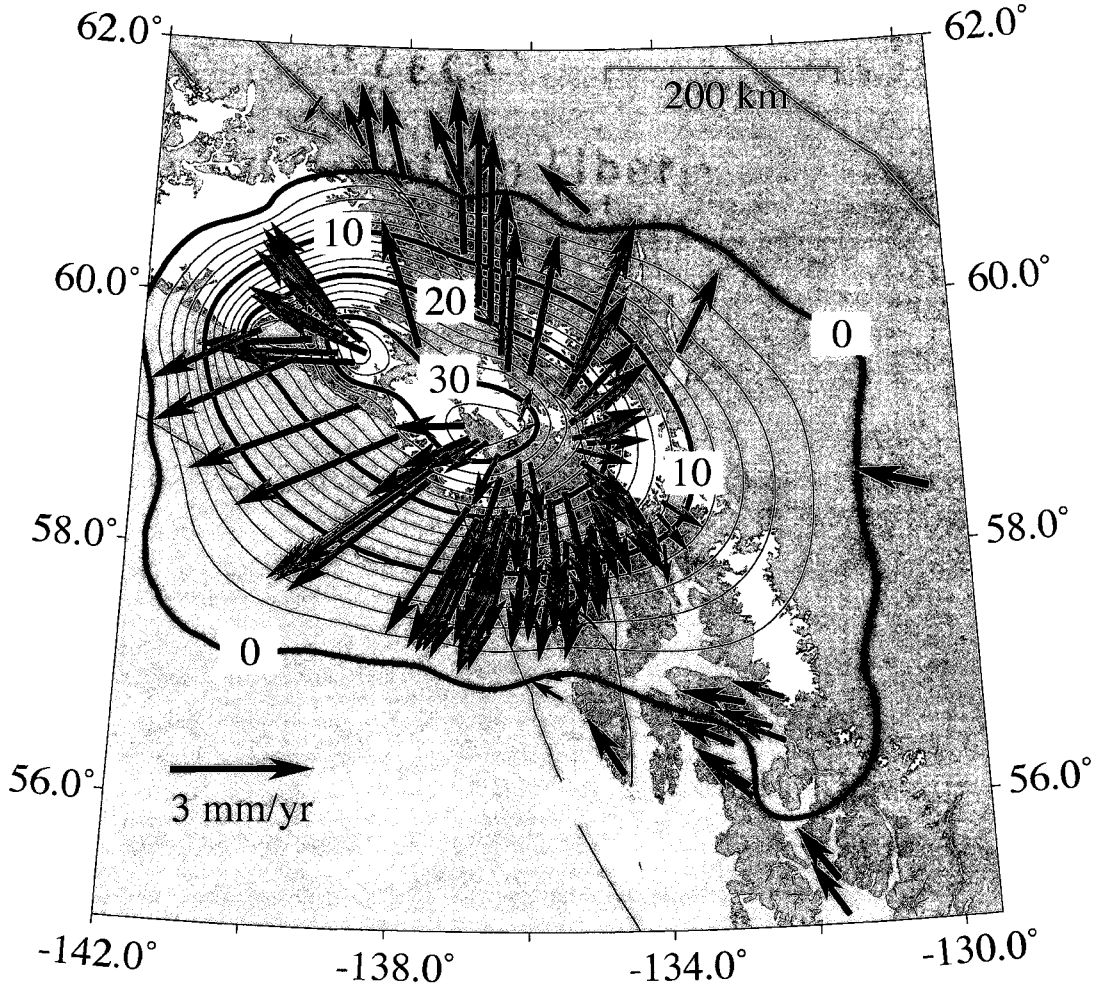

Figure 2.A-1. Glacial isostatic adjustment model predictions for southeast Alaska. Vectors show the horizontal motion while the contours show the vertical motion. Contour label units are mm/yr.

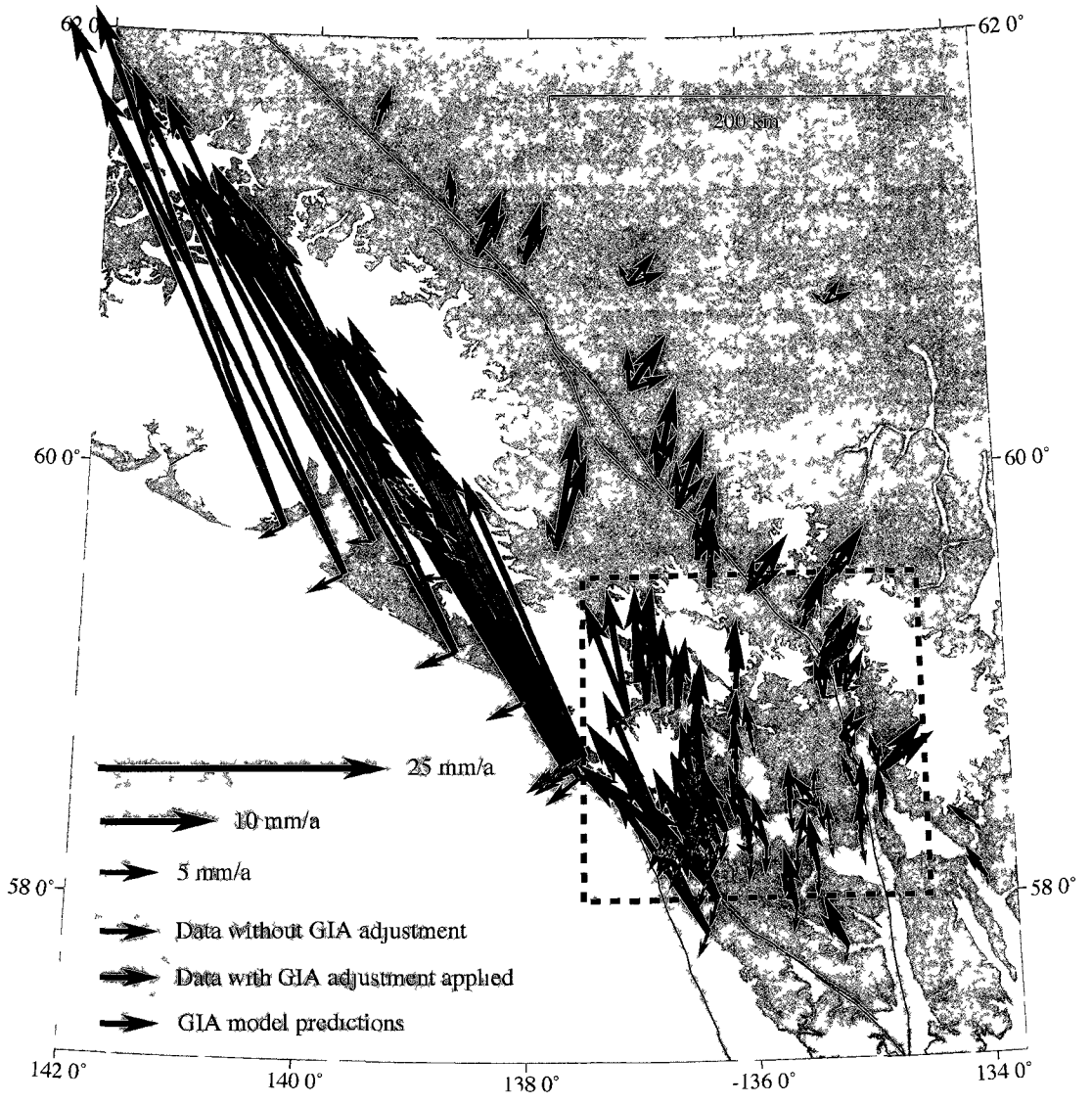

Figure 2.A-2. Comparison between data and glacial isostatic adjustment model predictions. Dashed outline shows area highlighted in Figure 2.A-3.

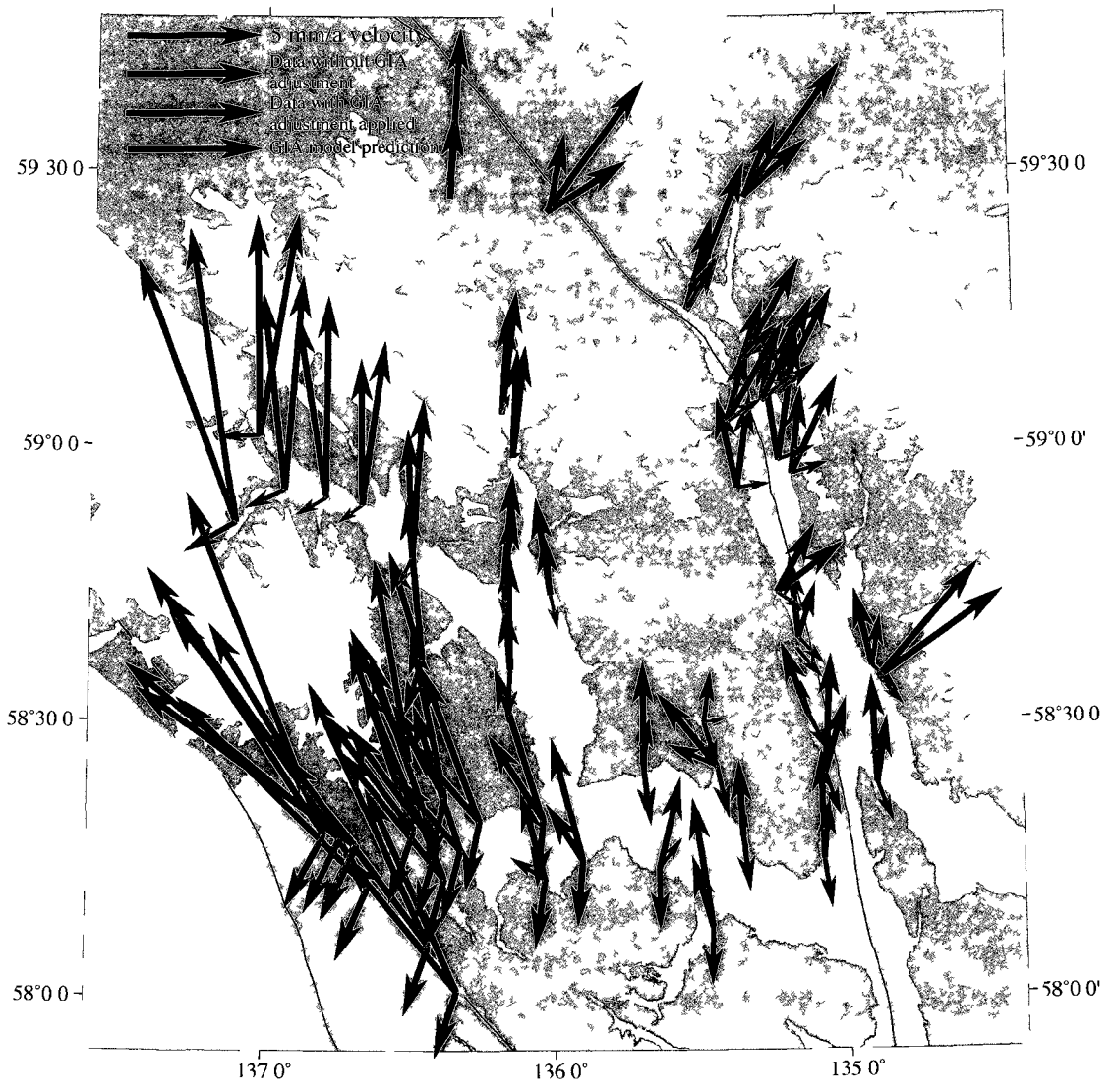

Figure 2 A-3 Comparison between data and glacial isostatic adjustment model predictions in the Glacier Bay area

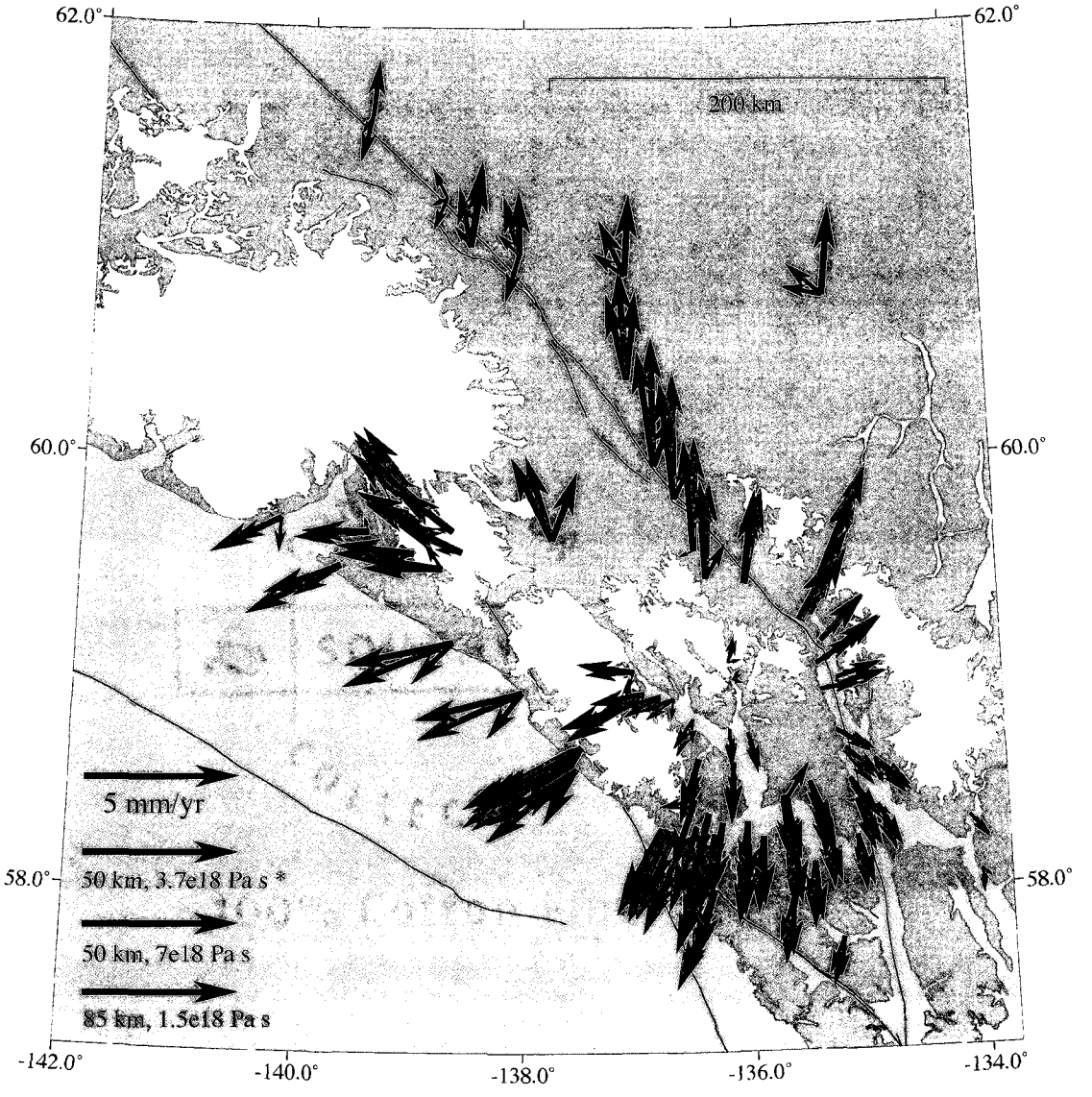

Figure 2.A-4. Comparison of GIA model predictions for preferred and end-member acceptable model parameters. Model marked with an asterisk is our best-fit model.

value of 9.6, which exceeds the F-test criteria for significance at the 99% level. These results strongly suggest that the Northern Cordillera has a motion distinct from that of stable North America.

Small velocities such as the ones seen in the Northern Cordillera might be caused by transient strain instead of long-term tectonic block motion. A possible source of transient signal could be a under- or over-estimation of the horizontal GIA effects in southeast Alaska. To test this possibility, we ran the test discussed in the previous paragraph using data that had had the two end-member GIA models applied instead of our best-fit model. In both cases, the block model version including the Northern Cordillera block had an overall misfit more than 10% smaller than the North America version and exceeded the F-test criteria for significance at the 99% level. Another likely candidate for non-tectonic transient motion would be GIA from the loss of the Laurentide Ice Sheet. The ICE4G model [*Peltier*, 2002] estimates that the horizontal motion from GIA effects in the Northern Cordillera would be small (< 2 mm/a) and oriented W-SW. Removing this signal would intensify the N-NE trend seen in the GPS velocities, not diminish it. Strain accumulation on an unrecognized locked fault is also not a probable explanation. There are simply no candidate faults that could produce N-NE-directed deformation over such a large area.

The eastern and southern boundaries of the Northern Cordillera block are not clearly delineated and our dataset does not extend far enough to directly examine the possible alternatives. *Leonard et al.* [2008] found that GPS velocities at sites located east of the Mackenzie and Canadian Rocky Mountains displayed near-zero horizontal motion,

suggesting that they represent stable North America. To the south, *McCaffrey et al.* [2007] presented a block model for the western Cordillera that included several blocks in southwestern British Columbia. We compared predicted block velocities from our Northern Cordillera block to the predicted velocities of the British Columbia blocks to see if they were compatible. The Northern Cordillera block predictions were larger and oriented in the opposite direction than the British Columbia block predictions. Based on this, we conclude that the Northern Cordillera block terminates north of this region.

An unresolved problem is how strain is transferred from the main plate boundary zone into the Northern Cordillera. Based on high heat flow measurements, *Mazzotti and Hyndman* [2002] devised a model for the Cordillera that involves a strong upper crust over a hot, weak, lower crust. This weak lower crust could serve as a detachment and allow the upper crust to move over the uppermost mantle. In this model, a small amount of Yakutat-North America relative motion is transferred into the Cordilleran upper crust, which then moves as a semi-rigid block over the weak lower crust and eventually thrusts over the stable craton. Such a model would allow the translation of the upper crust without much internal deformation.

In our block model, a portion of the Yakutat-North America relative motion is transmitted directly from the main plate boundary zone into the Fairweather and Baranof blocks, which then undergo clearly defined rotations. East of the Fairweather and Baranof blocks, our Northern Cordillera results are completely compatible with the model of *Mazzotti and Hyndman* [2002]. However, from our modeling we cannot rule out the alternative possibility that the Northern Cordillera is a rigid block and that the

convergence at its eastern boundary involves slip on faults that cut through the lithosphere.

2.8 Conclusions

We have used an extensive GPS dataset to develop a block model for southeastern Alaska and the adjoining region of Canada. The block model provides an integrated kinematic view of the regional tectonics and provides new constraints on seismic hazard evaluation.

Southeast Alaska is strongly affected by the collision of the Yakutat block with southern Alaska and our block model provides a snapshot of the present tectonic response. According to our model, the Yakutat block is moving at a velocity of 50.3 ± 0.8 mm/a towards N22.9 ± 0.6° W, a velocity that is similar in magnitude but more westerly than the velocity of the Pacific plate. The relative block motion between the Yakutat block and the Southern Alaska block indicates that ~ 45 mm/a of convergence must be accommodated across the St. Elias orogen to the north of our study area. The eastern edge of the Yakutat block is deforming, represented in the model by two small northwesterly moving blocks located west of the Fairweather fault. Part of the strain from the collision is transferred east of the Fairweather – Queen Charlotte system and causes the area north of Glacier Bay to rotate clockwise into the Northern Cordillera. The region south of Glacier Bay undergoes a much slower clockwise rotation and may be at least partially pulled along by the northern block motion. Strain is also transferred further east into the Northern Cordillera block, which displays small northeasterly motions. Our results suggest that the entire southeastern Alaska margin is mobile.

The vast majority of the relative block motion (and thus most of the seismic hazard) is concentrated along the Fairweather-Queen Charlotte fault system. Our block model predicts average dextral slip of 42.9 ± 0.9 mm/a along the Fairweather fault and transpressive relative motion along the Queen Charlotte fault equivalent to 43.8 ± 0.6 mm/a. In our model, a combination of dextral and reverse slip on the Boundary and Foothills faults accommodates about half of the observed convergence between the Pacific plate and the Fairweather fault. A deformation zone encompassing these two faults could provide an explanation for the 1899 Yakutat Bay earthquakes. The remaining relative motion is taken up on an offshore fault, here taken to be the Transition fault. GPS velocities along the coastal regions cannot be explained without the presence of the offshore fault.

2.9 Acknowledgements

Thora Árnadóttir and two anonymous reviewers provided helpful comments. We thank Stéphane Mazzotti and Lucinda Leonard for providing data from sites in the Canadian Cordillera and the Queen Charlotte Islands. We also thank Natasha Ruppert for providing focal mechanism information and comments about seismicity patterns, Peter Hauessler for providing geologic slip rate estimates on the northern Eastern Denali fault, and Wes Wallace for helpful discussions. Glacier Bay National Park provided assistance with remote field logistics. Figures were generated with the Generic Mapping Tools software of *Wessel and Smith* [1998]. This research was funded by NSF grants EAR-0409426, EAR-0408801, EAR-0229934, and EAR-9870144.

2.10 References

Arendt, A. A., K. A. Echelmeyer, W. D. Harrison, C. S. Lingle, and V. B. Valentine (2002), Rapid wastage of Alaska glaciers and their contribution to rising sea level, *Science*, *297*, 382-386.

Argus, D. F. (2007), Defining the translational velocity of the reference frame of Earth, *Geophys. J. Intl.*, *169*, 830-838

Árnadóttir, T., B. Lund, W. Jiang, H. Geirsson, H. Björnsson, P. Einarsson, and T. Sigurdsson (2009), Glacial rebound and plate spreading: results from the first countrywide GPS observations in Iceland, *Geophys. J. Int.*, *177*, 691-716.

Brew, D.A. (1994), Latest Mesozoic and Cenozoic magmatism in southeastern Alaska, in *The Geology of North America*, vol. G1, *The Geology of Alaska*, edited by G. Plafker and H.C. Berg, pp. 621-656, Geol. Soc. Am., Boulder, Colo.

Brew, D. A, and A. B. Ford (1981), The Coast plutonic complex sill, southeastern Alaska, in *The U.S. Geological Survey in Alaska: Accomplishments during 1978,* edited by N. R. D. Albert and T. L. Hudson, *U.S. Geol. Surv. Circ. 823-B*, B96-B98.

Brew, D. A., and A. B. Ford (1998), The Coast Mountains shear zones in southeastern Alaska – descriptions, relations, and lithologic terrance significance, in *Geologic Studies in Alaska by the U.S. Geological Survey, 1996*, edited by J. E. Gray and J.R. Riehle, *U.S. Geol. Prof. Paper 1595*, pp. 183-192.

Brew, D. A., B. R. Johnson, D. Grybeck, A. Griscon, D. F. Barnes, A. L. Kimball, J. C. Still, and J. L. Rataj (1978), Mineral Resources of Glacier Bay National Monument Wilderness Study Area, Alaska, *U.S. Geol. Surv. Open File Rept. 78-494*, 712 pp.

Bruns, T. R. (1983), Model for the origin of the Yakutat Block, an accreting terrane in the northern Gulf of Alaska, *Geology, 11*, 718-721.

Clague, J. J., S. G. Evans (1993), Historic retreat of Grand Pacific and Melbern Glaciers, St. Elias Mountains, Canada: an analogue for decay of the Cordilleran ice sheet at the end of the Pliestocene?, *J. Glaciol., 39*, 619 – 624.

Doig, R. (1998), Paleoseismological evidence from lake sediments for recent movement on the Denali and other faults, Yukon Territory, Canada, *Tectonophysics, 296*, 363-370.

Doser, D. I. (2006), Relocations of earthquakes (1899-1917) in south-central Alaska, *Pure Appl. Geophys. , 163*, 1461-1478.

Doser, D. I., and R. Lomas (2000), The transition from strike-slip to oblique subduction in southeastern Alaska from seismological studies, *Tectonophysics, 316*, 45-65.

Dziewonski, A. M., and D. L. Anderson (1981), Preliminary Reference Earth Model (PREM), *Phys. Earth. Planet. Inter., 25*, 297-356.

Ferris, A., and G. A. Abers, D. H. Christensen, and E. Veenstra (2003), High Resolution image of the subducted Pacific (?) Plate beneath central Alaska, 50-150 km depth, *Earth Planet. Sci. Lett., 214*, 575-588.

Fletcher, H. (2002), Crustal deformation in Alaska measured using Global Positioning System, Ph.D. dissertation, 135 pp., Univ. of Alaska, Fairbanks.

Fletcher, H. J, and J. T. Freymueller (1999), New constraints on the motion of the Yakutat Block, *Geophys. Res. Lett., 26*, 3029-3032.

Fletcher, H. J., and J. T. Freymueller (2003), New constraints on the motion of the Fairweather Fault, Alaska, from GPS Observations, *Geophys. Res. Lett.*, *30*(3), doi:10.1029/2002GL016476.

Freed, A. M., R. Burgmann, E. Calais, J. Freymueller, and S. Hreinsdottir (2006), Implications of deformation following the 2002 Denali, Alaska, earthquake for postseismic relaxation processes and lithospheric rheology, *J. Geophys. Res., 111*, B01401, doi:10.1029/2005JB003894.

Freymueller, J. T., S. C. Cohen, R. Cross, J. Elliott, H. Fletcher, C. Larsen, S. Hreinsdóttir, and C. Zweck (2008), Active deformation processes in Alaska, based on 15 years of GPS measurements, in *Active Tectonics and Seismic Potential of Alaska*, edited by J. T. Freymueller et al., pp. 1-42, American Geophysical Union, Washington, D.C.

Gipp, M. R. (2003), Subsidence and tectonic controls on glacially influenced continental margins: examples from the Gulf of Alaska and the western Scotian Shelf and Slope, *Quat. Int., 99*, 3-27.

Gulick, S. P. S., L. A. Lowe, T. L. Pavlis, J. V. Gardner, and L. A. Mayer (2007), Geophysical insights into the Transition Fault debate: Propagating strike-slip in response to stalling Yakutat Block subduction in the Gulf of Alaska, *Geology, 35*, 763-766.

Hallet, B., L. Hunter, and J. Bogen (1996), Rates of erosion and sediment evacuation by glaciers: A review of field data and their implications, *Global and Planetary Change*, *12*, p. 213–235.

Harrison, W. D., C. F. Raymond, K. A. Echelmeyer, R. M. Krimmel (2003), A macroscopic approach to glacier dynamics, *J. Glaciol.*, *49*, (164), 13 – 21.

Henton, J. A., M. R. Craymer, R. Ferland, H. Dragert, S. Mazzotti, and D. L. Forbes (2006), Crustal Motion and Deformation Monitoring of the Canadian Landmass, *Geomatica*, *60*, 173-191.

Horner, R. B. (1983), Seismicity in the St. Elias region of northwestern Canada and southeastern Alaska, *Bull. Seis. Soc. Am.*, *73*, 1117-1137.

Hreinsdóttir, S. , J. T. Freymueller, R. Bürgmann, and J. Mitchell (2006), Coseismic deformation of the 2002 Denali Fault Earthquake: Insights from GPS measurements, *J. Geophys. Res.*, *111*, B03308, doi:10.1029/2005JB003676.

Jaeger, J. M., C. A. Nittrouer, N. D. Scott, and J. D. Milliman (1998), Sediment accumulation along a glacially impacted mountainous coastline: Northeast Gulf of Alaska, *Basin Research, 10*, 155-173.

Johnson, K. M., R. Bürgmann, and J. T. Freymueller (2009), Coupled afterslip and visco-elastic flow following the 2002 Denali Fault, Alaska earthquake, *Geophys. J. Intl.*, *176*, 670-682.

Kalbas, J. L., A. M. Freed, and K. D. Ridgway (2008), Contemporary fault mechanics in southern Alaska, in *Active Tectonics and Seismic Potential of Alaska*, edited by J. T. Freymueller et al., pp. 321-336, American Geophysical Union, Washington, D.C.

Klepeis, K. A., M. L. Crawford, and G. Gehrels (1998), Structural history of the crustal-scale Coast shear zone north of Portland Canal, southeast Alaska and British Columbia, *J. Structural Geol., 20*(7), 883-904.

Kogan, M. G., and G. M. Steblov (2008), Current global plate kinematics from GPS (1995–2007) with the plate-consistent reference frame, *J. Geophys. Res., 113*, B04416, doi:10.1029/2007JB005353.

Koppes. M. N., and B. Hallet (2002), Influence of rapid glacial retreat on the rate of erosion by tidewater glaciers, *Geology*, *30*, 47-50.

Lagoe, M. B., C. H. Eyles, N. Eyles, and C. Hale (1993), Timing of late Cenozoic tidewater glaciation in the far North Pacific, *Geol. Soc. Am. Bull.*, *105*, 1542-1560.

Lahr, J. C., and G. Plafker (1980), Holocene Pacific-North American plate interaction in southern Alaska: Implications for the Yakataga seismic gap, *Geology, 8*, 483-486.

Lahr, J.C., R. A. Page, Stephens, C.D., Christensen, D.H., 1988, Unusual earthquakes in the Gulf of Alaska and fragmentation of the Pacific Plate, *Geophys. Res. Lett., 15*, 1483-1486.

Lanphere, M. A. (1978), Displacement history of the Denali fault system, Alaska and Canada, *Can. J. Earth Sci., 15,* 817-822.

Larsen, C. F., R. J. Motyka, J. T. Freymueller, K. A. Echelmeyer, and E. R. Ivins (2004), Rapid uplift of southern Alaska caused by recent ice loss, *Geophys. J. Intl., 158*, 1118-1133.

Larsen, C. F., R. J. Motyka, J. T. Freymueller, K. A. Echelmeyer, and E. R. Ivins (2005), Rapid viscoelastic uplift in southeast Alaska caused by post-Little Ice Age glacial retreat, *Earth Planet. Sci. Lett., 237*, 548-560.

Leonard, L. J., S. Mazzotti, and R.D. Hyndman (2008), Deformation rates estimated from earthquakes in the northern Cordillera of Canada and eastern Alaska, *J. Geophys. Res., 113*, B08406, doi:10.1029/2007JB005456.

Leonard, L. J., R. D. Hyndman, S. Mazzotti, L. Nykolaishen, M. Schmidt, and S. Hippchen (2007), Current deformation in the northern Canadian Cordillera inferred from GPS measurements, *J. Geophys. Res.*, *112*, B11401, doi:10.1029/2007JB005061.

Lisowski, M, J. C. Savage, and R. O. Buford (1987), Strain accumulation across the Fairweather and Totschunda faults, Alaska, *J. Geophys. Res.*, *92*, 11,552-11,560.

MacKevett, E. M., D. A. Brew, C. C. Hawley, L. C. Huff, and J. G. Smith (1971), Mineral Resources of Glacier Bay National Monument, Alaska, *U.S. Geol. Surv. Prof. Paper 632*, 96 pp.

Mazzotti, S., and R. D. Hyndman (2002), Yakutat collision and strain transfer across the northern Canadian Cordillera, *Geology, 30*(6), 495-498.

Mazzotti, S., L. J. Leonard, R. D. Hyndman, and J. F. Cassidy (2008), Tectonics, Dynamics, and Seismic Hazard in the Canada-Alaska Cordillera, in *Active Tectonics and Seismic Potential of Alaska*, edited by J. T. Freymueller et al., pp. 297-320, American Geophysical Union, Washington, D.C.

Mazzotti, S., R. D. Hyndman, P. Flück, A. J. Smith, and M. Schmidt (2003), Distribution of the Pacific/North America motion in the Queen Charlotte Islands – S. Alaska plate boundary zone, *Geophys. Res.Lett., 30*(14), 1762, doi:10.1029/2003GL017586.

McCaffrey, R. (2002), Crustal block rotations and plate coupling, in *Plate Boundary Zones*, edited by S. Stein and J. Freymueller, pp. 101-122, American Geophysical Union, Washington, D.C.

McCaffrey, R., A. I. Qumar, R. W. King, R. Wells, G. Khazaradze, C. A. Williams, C. W. Stevens, J. J. Vollick, and P. C. Zwick (2007), Fault locking, block rotation and crustal deformation in the Pacific Northwest, *Geophys. J. Int.*, doi: 10.1111/j.1365-246X.2007.03371.x.

McClelland, W. C., B. Tikoff, and C. A. Manduca (2000), Two-phase evolution of accretionary margins: examples from the North American Cordillera, *Tectonophys., 326*, 37-55.

McClelland, W. C., G. E. Gehrels, S. D. Samson, and P. J. Patchett (1992), Structural and geochronologic relations along the western flank of the Coast Mountains Batholith: Stikine River to Cape Fanshaw, central southeastern Alaska, *J. Structural Geol. 100*(4), 107-123.

Meade, B. J. and B. H. Hager (1999), Simultaneous inversions of geodetic and geologic data for block motions in plate boundary zones, *AGU Fall Meet., 80*, F267-268.

Meade, B. J., and B. H. Hager (2005), Block models of crustal motion in southern California constrained by GPS measurements, *J. Geophys. Res., 110*, B03403, doi:10.1029/2004JB003209.

Meade, B. J., B. H. Hager, S. C. McClusky, R. E. Rellinger, S. Ergintav, O. Lenk, A. Barka, and H. Ozener (2002), Estimates of seismic potential in the Marmara Sea region from block models of secular deformation constrained by Global Positioning System measurements, *Bull. Seis. Soc. Am., 92*, 208-215.

Milne, G. A., J. L. Davis, J. X. Mitrovica, H.-G. Scherneck, J. M. Johansson, M. Vermeer, H. Koivula (2001), Space-geodetic con- straints on glacial isostatic adjustment in Fennoscandia, *Science, 291*, 2381–2385.

Motyka, R. J. (2003), Little ice age subsidence and post little ice age uplift at Juneau, Alaska inferred from dendrochronology and geomorphology, Quat. Res., *59*, 300 309.

Nishenko, S. P., and K. H. Jacob (1990), Seismic potential of the Queen Charlotte Alaska-Aleutian seismic zone, *J. Geophys. Res., 95*, 2511-2532.

Pavlis, T. L., C. Picornell, L. Serpa, R. L. Bruhn, and G. Plafker (2004), Tectonic processes during oblique collision: Insights from the St. Elias orogen, northern North American Cordillera, *Tectonics, 23*, TC3001, doi:10.1029/2003TC001557.

Pegler, G., and S. Das (1996), The 1987-1992 Gulf of Alaska earthquakes, *Tectonophysics, 257*, 111-136.

Peltier, W. R. (2002), Global glacial isostatic adjustment: palaeogeodetic and space geodetic tests of the ICE-4G (VM2) model, *J. Quaternary Sci., 17*, 491-510.

Perez, O. J., and K. H. Jacob (1980), Tectonic model and seismic potential of the eastern Gulf of Alaska and Yakataga Seismic Gap, *J. Geophys. Res., 85*, 7132-7150.

Plafker, G., and W. Thatcher (2008), Geological and geophysical evaluation of the mechanism of the great 1899 Yakutat Bay Earthquake, in *Active Tectonics and Seismic Potential of Alaska*, edited by J. T. Freymueller et al., pp. 215-236, American Geophysical Union, Washington, D.C.

Plafker, G., L. Gilpin, and J. Lahr (1994b), Neotectonic map of Alaska, in The Geology of North America, Decade of North American Geology, vol. G-1, edited by G. Plafker and H. C. Berg, Geol. Soc. Am., Boulder, Colo.

Plafker, G., J. C. Moore, and G. R. Winkler (1994a), Geology of the southern Alaska margin, in *The Geology of North America*, vol. G1, *The Geology of Alaska*, edited by G. Plafker and H. C. Berg, pp. 389-449, Geol. Soc. Am., Boulder, Colo.

Plafker, G., T. Hudson, T. R. Bruns, and M. Rubin (1978), Late Quaternary offsets along the Fairweather faults and crustal plate interactions in southern Alaska, *Can. J. Earth Sci., 15*, 805-816.

Plattner, C., R. Malservisi, T. H. Dixon, P. LaFemina, G. F. Sella, J. Fletcher, F. Suarez-Vidal (2007), New constraints on relative motion between the Pacific Plate and Baja California microplate (Mexico) from GPS measurements, *Geophys. J. Int.*, doi:10.1111/j.1365-246X.2007.03494.x.

Pollitz, F. F. (2005), Transient rheology of the upper mantle beneath central Alaska inferred from the crustal velocity field following the 2002 Denali earthquake, *J. Geophys. Res., 110*, B08407, doi:10.1029/2005JB003672.

Porter, S. C. (1989), Late Holocene fluctuations of the fiord glacier system in Icy Bay, Alaska, *Arct. Alp. Res., 21*, 364 – 379.

Okada, Y. (1985), Surface deformation due to shear and tensile faults in a half-space, *Bull. Seismol. Soc. Am., 75*, 1135–1154.

Reece, R., S. P. Gulick, G. L. Christeson, and L. L. Worthington (2009), Intraplate shearing and basin deformation in the Pacific Plate as a result of the Yakutat Block collision with North America, *Eos Trans. AGU, 90*(52), Fall Meet. Suppl., Abstract T33C-1924.

Richter, D. H., and N. A. Matson (1971), Quaternary faulting in the eastern Alaska Range, *Geol. Soc. Am. Bull., 82,* 1529-1540.

Rusmore, M. E., G. Gehrels, and G. J. Woodsworth (2001), Southern continuation of the Coast shear zone and Paleocene strain partitioning in British Columbia – southeast Alaska, *Geol. Soc. Am. Bull., 113*(8), 961-975.

Schell, M. M., and Ruff, L. J., (1989) Rupture of a seismic gap in southeastern Alaska; The Sitka earthquake (Ms 7.6): *Physics of the Earth and Planetary Interiors, 54*, p. 241-257.

Seitz, G. J., P. J. Haeussler, A. J. Crone, P. Lipovsky, and D. P. Schwartz (2008), Eastern Denali fault slip rate and paleoseismic history, Kluane Lake area, Yukon Territory, Canada, *AGU Fall Meet.,* T53B-1947.

Sella, G. F., S. Stein, T. H. Dixon, M. Craymer, T. S. James, S. Mazzotti, and R.K. Dokka, (2007), Observation of glacial isostatic adjustment in "stable" North America with GPS, *Geophy. Res. Lett., 34*, L02306, doi: 10.1029/2006GL027081.

Sheaf, M. A., L. Serpa, and T. L. Pavlis (2003), Exhumation rates in the St. Elias Mountains, Alaska, *Tectonophysics, 367*, 1-11.

Spada, G. (2003), The theory behind TABOO, Samizdat Press, Golden-White River Junction.

Spada, G., A. Antonioli, L. Boschi, V. Brandi, S. Cianetti, G. Galvani, C. Giunchi, B. Perniola, N. P. Agostinetti, A. Piersanti, and P. Stocchi (2003), TABOO, User Guide, Samizdat Press, Golden-White River Junction.

Spada, G., A. Antonioli, L. Boschi, V. Brandi, S. Cianetti, G. Galvani, C. Giunchi, B. Perniola, N. P. Agostinetti, A. Piersanti, and P. Stocchi (2004), Geodesy: modeling earth's post-glacial rebound, *EOS Trans., 85*, 62.

Suito, H., and J. T. Freymueller (2009), A viscoelastic and afterslip postseismic deformation model for the 1964 Alaska earthquake, *J. Geophys. Res., 114*, B11404, doi:10.1029/2008JB005954.

Tarr, R. S., and L. Martin (1912), The earthquakes of Yakutat Bay, Alaska in September 1899, *U.S. Geol. Surv. Prof. Paper, 69*, 135 pp.

Wessel, P., and W. H. F. Smith (1998), New, improved version of the Generic Mapping Tools Released, *EOS Trans., 79,* 579.

Wiles, G. C., D. J. Barclay, P. E. Calkin (1999), Tree-ring-dated Little Ice Age histories of maritime glaciers from western Prince William Sound, Alaska, *The Holocene, 9*, 163 – 173.

Wolf, L. W., C. A. Rowe, R. B. Horner (1997), Periodic seismicity near Mt. Ogden on the Alaska-British Columbia border: A case for for hydrologically triggered earthquakes?, *Bull. Seis. Soc. Am, 87*(6), 1473-1483.

Zumberge, J. F., Heflin, M. B., Jefferson, D. J., Watkins, M.M. & Webb, F.H., (1997), Precise point positioning for the efficient and robust analysis of GPS data from large networks, *J. Geophys. Res., 102,* 5005–5017.

velocities begin to rotate clockwise and increase in magnitude before becoming smaller again near Prince William Sound. Finally, velocities at sites along the northern and western edges of the Bering Glacier display a clear counterclockwise rotation (more prominent in the north) relative to surrounding sites.

3.5 Block Model

3.5.1 Modeling Approach

To develop our block model for the St. Elias orogen, we adapted the method of *Meade and Hager* [2005] as described in *Elliott et al.* [2010]. We present a brief summary of the concept below; further details can be found in those studies.

Assuming linear elasticity, the interseismic velocity $\vec{v}_I$ observed at a GPS site as a combination of block motion and elastic effects:

$$\vec{v}_I = \vec{v}_B(\vec{x}_{site}) - \vec{v}_{SD}(\vec{x}_{site}, \vec{x}_{geom}) \quad (1)$$

The GPS site coordinates correspond to $\vec{x}_{site}$, the fault geometry to $\vec{x}_{geom}$, and the linear block velocity to $\vec{v}_B$. The term $\vec{v}_{SD}$ represents the slip deficit accumulating on a locked fault and can be written as

$$\vec{v}_{SD} = \mathbf{G}(\vec{x}_{site}, \vec{x}_{geom})\vec{s} \quad (2)$$

G is the matrix of Green's functions that relate slip, $\vec{s}$, on each fault plane to the displacement at each GPS site assuming an elastic half-space and a Poisson's ratio of 0.25 [*Okada*, 1985].

Both the block velocity term and the slip deficit term can be written in terms of the block angular velocity, Ω. Combining the block motions and slip deficit

contributions into a single term **R** and substituting our data vector (observed GPS velocities and a priori block angular velocities) $\vec{d}$ for the interseismic velocity term yields

$$\vec{d} = \mathbf{R}\vec{\Omega}. \tag{3}$$

This equation allows us to solve for the block angular velocities $\vec{\Omega}$ through a weighted linear least-squares inversion.

$$\vec{\Omega}_{est} = (\mathbf{R}^T\mathbf{W}\mathbf{R})^{-1}\mathbf{R}^T\mathbf{W}\vec{d} \tag{4}$$

where $\mathbf{W}^T\mathbf{W} = \Sigma^{-1}$ and Σ is the data covariance matrix.

In this method, the fault slip rates depend directly on the block angular velocities and the block geometries. Since the slip rates cannot vary independently of each other, the block model guarantees that the estimated slip rates are internally consistent.

3.5.2 Blocks and Fault Geometries

Our block model includes four fault systems or fault zones: the Malaspina – Pamplona system, the Yakataga – Chaix Hills system, the Foreland fault zone, and the decollement between the Yakutat block and the upper plate. These faults form the boundaries between four blocks (Figure 3.6). The mountainous landscape and extreme ice cover of the St. Elias region results in many inferred faults with imprecise locations on maps. The fault locations used in our model are derived from geologic maps, seismicity trends, or topographic features as discussed below.

The Pamplona – Malaspina fault system has been postulated to be the present day deformation front between the Yakutat block and southern Alaska [*Lahr and Plafker*, 1980; *Worthington et al.*, 2008]. Seismic reflection profiles imaged three faults within

the active, eastern portion of the offshore Pamplona fault zone [*Worthington et al.*, 2010]. *Doser et al.* [1997] relocated a series of moderate (M5-6.7) earthquakes that occurred in the Pamplona zone in 1970 and *Doser* [2006] suggested that the September 4, 1899 M8 event may have occurred there. The Pamplona zone presumably links to the Malaspina fault somewhere in the vicinity of Icy Bay, where a prominent cluster of seismicity is present (Figure 3.2). Most of the trace of the Malaspina fault is obscured by ice, but the fault was penetrated during exploratory drilling in the hills northeast of Icy Bay [*Plafker*, 1987]. Aftershock distribution implies that the Malaspina fault may have been involved in the 1979 St. Elias earthquake rupture [*Estabrook et al.*, 1992] and the southern Alaska margin may have ruptured east to the fault during past megathrust events [*Shennan et al.*, 2009].

Our model Yakataga – Chaix Hills system is a composite of the Dome Pass fault [*Plafker and Miller*, 1957], the Chaix Hills fault, and the Miller Creek fault. Much of region is covered by ice, but the Chaix Hills fault is exposed on both sides of the Tyndall Glacier fjord in northern Icy Bay [*Chapman et al.*, in prep.]. Thermochronology results [*Spotila and Berger*, 2010] suggest that the Chaix Hills fault is currently active in the region north of the Malaspina Glacier.

The Foreland fault zone is included as a blind thrust in our model. Seismicity clusters (Figure 3.2) and aftershock migration following the 1979 St. Elias earthquake [*Estabrook et al.*, 1992] indicate that active deformation continues south of the Malaspina fault. In addition, the GPS velocities along the eastern coast of Icy Bay (Figure 3.5) indicate that convergence is occurring between those stations and the coherent Yakutat

block along the eastern edge of the Malaspina Glacier. The Foreland fault zone is discussed further below.

We take the Yakutat decollement to be the interface between sedimentary layers and the Yakutat basement crust as interpreted from offshore seismic reflection profiles [*Worthington et al.*, 2010]. In the eastern half of our study region, the decollement likely ruptured during the 1979 St. Elias earthquake [*Estabrook et al.*,1992]. Our placement of the beginning of the main megathrust along the eastern edge of the Bering Glacier coincides with the easternmost limit of observed coseismic uplift from the 1964 Prince William Sound earthquake [*Shennan et al.*, 2009] and provides the best fit to the GPS data.

Previous studies [*Lahr and Plafker*, 1980; *Fletcher*, 2002] proposed that most of Alaska south of the Denali fault was part of a counterclockwise rotating block. The Southern Alaska block (SOAK) [*Fletcher*, 2002], which had a rotation rate constrained by GPS data, and the Wrangell block [*Lahr and Plafker*, 1980] gave motion predictions of 5 – 6 mm/yr within the St. Elias orogen. We found that our data required faster block motions and propose that the Elias block occupies the region north and west of the central thrust belt (Figure 3.6). A boundary between the Elias block and the slower moving SOAK must exist north of our study area based on slip rates along the Denali fault [*Fletcher*, 2002; *Freymueller et al.*, 2008], but it is beyond the scope of the present work to determine the location of that boundary.

We include the Bering Deformation Zone (BDZ) in the region surrounding the western edge of the Bering Glacier. The term deformation zone is used instead of block

due to the fact that the best fit between the model and data was achieved by allowing all boundaries of the area to fully creep. Our motivation for including the BDZ was to improve the fit between the GPS data and the block model in this region. An earlier version of our model, without any structures or additional blocks in the Bering Glacier region (Figure 3.7a), resulted in a coherent pattern of southwest-directed residuals at sites located along the northern and western edges of the glacier. *Bruhn et al.* [2004] proposed a thrust fault boundary beneath the Bering Glacier, separating the eastern orogen from a belt of second-phase folds west of the glacier. Including this boundary (Figure 3.7b) in our initial model improved the misfit between the model and the GPS data by less than 5%. Adding the BDZ reduced the misfit by 30%. The evidence for and implications of the BDZ are discussed further below.

Fault locking depths, dips, widths in the downdip direction, and degree of coupling on the fault planes are all fixed; they are not estimated as part of the inversion. We used an iterative process to adjust fault segment endpoints, fault locking depths, fault width and dip, and percent coupling to find the geometry that minimized the misfit to the GPS data. When the information was available, we began with estimates of the fault geometry based on seismic data and geologic measurements. Geologic estimates of dip may disagree with our final fault geometry since faults are often steeper at the surface than at depth. Our model fault planes have a constant dip along their width, representing the average dip. The GPS data constrain how deep the model fault plane lies beneath the sites and where the downdip end of the locked fault is located. Unless there are GPS sites

near the updip end of the fault, our model geometry will not be sensitive to near surface steepening of the fault. Table 3.4 lists the parameters for our model faults.

3.5.3 A Priori Block Motion Estimate

Our block modeling approach allows the inclusion of a priori block motion estimates. We used an a priori block angular velocity for one block in our model, the Yakutat block. The data set used in this study does not include any GPS sites on the Yakutat block, so its inclusion is solely important for the calculation of deformation along its boundaries, including the decollement. The Yakutat block velocity was taken from *Elliott et al.* [2010].

We also included uncertainties for the Yakutat block angular velocities as a priori information. To guarantee numerical stability during the inversion and limit the maximum rate of vertical axis rotation for small blocks, we applied loose a priori uncertainties to the estimated angular velocities in our block model. These were large, with σ equal to 0.1 radians/My.

3.6 Results and Interpretation

3.6.1 Pole and Rotation Rate Estimates

We inverted 133 data (east and north components of GPS velocities at 65 sites and X, Y, and Z components of a priori angular velocities for one block) to estimate 12 model parameters (X, Y, and Z components of angular velocity for four blocks). We transformed the estimated angular velocities from the XYZ coordinate system to the geographic coordinate system (latitude, longitude, and rotation rate) in order to present the block rotations in the familiar Euler pole format. Figure 3.8 and Table 3.5 show the

Euler poles, rotation rates, angular velocities, and associated uncertainties for the blocks in our preferred model. Predicted linear block velocities are displayed in Figure 3.9.

As discussed in *Elliott et al.* [2010], the angular velocities of small blocks with uneven site distributions have a large uncertainty in one component, usually the local vertical. In cases where the axis of the Cartesian error ellipsoid is large, the uncertainty regions for the Euler poles are distorted from ellipses into the shape of a great circle due to the nonlinear transformation between geographic and Cartesian coordinates. Distortion of the uncertainty ellipsoid is exacerbated at high latitudes such as those in this study. For these reasons, we display a Monte Carlo sampling of the uncertainty region rather than the standard 95% confidence ellipses with the poles in Figure 3.8. We took 2500 random samples of a zero-mean distribution with a covariance equal to the angular velocity covariance, added each sample to our estimated angular velocities, computed the corresponding Euler pole, and plotted the pole as a point on the map. The density of the points on the map corresponds to the probability distribution of the pole location. For blocks with large uncertainty regions for the poles, the predicted linear block velocities for points on the blocks will still have small uncertainties. This follows from the strong correlation between the pole location and the angular speed.

The pole for the Malaspina block is located in the southern Mackenzie Mountains, making it farthest pole from southern Alaska. This distance is consistent with the parallel velocities observed on the block. We find the pole for the Icy Bay block in the western Yukon Territory. A location closer to the block allows more variation in velocities along

the block, as is seen in the increase in block velocity magnitudes from southwest to northeast along the Icy Bay block.

Even closer to its block, the Elias block pole is located east of Kodiak Island. The proximity of the pole results in predicted block motions that vary considerably along the span of the block. In the east, the block velocities are largest and are nearly parallel to the velocities along the Icy Bay block. Moving towards Prince William Sound, the estimated Elias block velocities become smaller and display a counterclockwise rotation.

The pole for the Bering Deformation Zone lies in the Gulf of Alaska south of the Bering Glacier. This location results in linear block velocity estimates that clearly undergo a counterclockwise rotation as well as a north to south decrease in magnitude.

3.6.2 Relative Block Motions

Relative block motions resulting from our preferred model are shown in Figure 3.10. In the eastern orogen, relative motion is accommodated within a relatively narrow band of thrust faults. At the outboard edge of this band, the Foreland fault zone displays nearly pure convergance. The Malaspina – Pamplona system shows sinstral – oblique motion. Located furthest inboard from the deformation front, the Yakataga – Chaix Hills fault system accommodates the largest amount of the surface relative block motion. The sense of motion becomes slightly more oblique from west to east and the rate of relative motion decreases as the fault moves onshore and further inland into the orogen.

North and west of the band of thrust faults, relative block motion is accommodated on the subduction interface between the Yakutat block and the Elias block. The sense of motion remains a constant NW – SE throughout, but the orientation

of fault planes result in more oblique motion in the eastern orogen than in the west. The magnitude of the relative motion increases from east to west, with the highest values predicted for the interface beneath Prince William Sound.

3.6.3 Goodness of Fit

Our block model gives a reasonable explanation for the observed GPS velocity field in the St. Elias orogen of southeast and south central Alaska as shown by the residual vector plot in Figure 3.11. The reduced χ^2 (χ^2 per degree of freedom) is 1.6. 90% of the residuals fall within the 95% confidence bounds for the data. The mean residual velocity magnitude is 1.5 mm/yr while the mean data uncertainty is 1.8 mm/yr. The residual velocities do not show a coherent trend in any region.

3.7 Discussion

3.7.1 Slip Rates and Seismic Hazard

None of the faults in our model have published geodetic or geologic slip rate estimates. Previous models of the St. Elias orogen [e.g. *Sauber et al.*, 1997; *Savage and Lisowski*, 1988] have usually assumed that the main source of the regional deformation is strain accumulation along a subduction interface that is slipping at a rate equal to the Pacific plate – North America relative velocity. This rate of motion was 50 – 60 mm/yr depending on the plate motion model used (e.g. *Minster and Jordon*, 1978; *Chase*, 1978; *DeMets et al.*, 1994].

Our block model predicts variable rates of slip along the Malaspina fault, with obliquity decreasing from south to north. Offshore, an average of 6.9 ± 1.5 mm/yr of left-lateral strike-slip and 6.3 ± 3.9 mm/yr of reverse slip occurs. Within Icy Bay, the

fault appears to be fully creeping. Northeast of Icy Bay, the segment of the fault crossing the Samovar Hills has 5.2 ± 1.4 mm/yr of left-lateral slip and 10.5 ± 3 mm/yr of reverse slip. Farther east, our model shows an average of 5.4 ± 1.8 mm/yr left-lateral motion with 13.8 ± 6.9 mm/yr of reverse slip, but the fault planes are 40% coupled, resulting in effective slip rates of 2.6 mm/yr and 5.5 mm/yr.

In the region between the coast and Icy Bay, our model gives an average of 8.4 ± 8.2 mm/yr right-lateral strike-slip motion and 22.0 ± 1.4 mm/yr of reverse slip along the Yakataga – Chaix Hills fault. Between Icy Bay and the eastern border of our study area, the model puts 8.3 ± 8.7 mm/yr of right-lateral slip and 14.3 ± 1.8 mm/yr of reverse slip on the fault. The Yakataga – Chaix Hills fault system, represented in our block model by a single fault strand, is likely comprised of multiple parallel faults. For this reason, our slip rates should be viewed as a total estimate for the Yakataga – Chaix Hills region. Even as a total estimate, our slip rates suggest a much higher rate of convergence across the central fold-and-thrust belt than the average ~ 6 mm/yr over the past ~ 6 Myr found by *Wallace* [2008]. These two estimates are not necessarily incompatible. Several studies have presented evidence that the St. Elias orogen has undergone a tectonic reorganization, including a migration of the active deformation to the onshore region, since the late Pliocene [*Berger et al.,* 2008; *Worthington et al.*, 2010; *Chapman et al.*, in prep.]. Such a shift in deformation would cause present-day rates of convergence across the fold-and-thrust belt to be different than those observed over the longer term geologic record.

We suggest that the interface that ruptured during the 1979 St. Elias earthquake is the Yakutat – Elias block decollement, not the Pacific – North America decollement. On this interface, our model estimates 23.5 ± 1 mm/yr of right-lateral slip and 31.4 ± 1 mm/yr of reverse slip with 30% coupling on the plane, giving effective slip deficit rates of 7 mm/yr dextral motion and 9.4 mm/yr thrust motion. This oblique slip is compatible with the results of *Estabrook et al.* [1992] that suggested a pure thrust mechanism for the first subevent of the earthquake and a second subevent with a significant right-lateral strike-slip component.

Using paleoseismic evidence, *Shennan et al.* [2009] concluded that the great earthquakes along the Aleutian megathrust ruptured as far east as the Bering Glacier during the past three events in 1964, ~ 900 BP, and ~ 1500 BP. *Chapman et al.* [in prep.] inverted coseismic uplift data to estimate ~ 17 m of dip-slip during the 1964 event on the segment of the decollement underlying the southern end of the Bering Glacier. Our model predicts 90% coupling on that fault segment and an effective slip rate of 14.3 ± 0.5 mm/yr left-lateral strike-slip motion and 44.4 ± 0.8 mm/yr of reverse slip. At this rate of reverse motion, the fault would recover 17 m of motion in < 400 years, well within the reoccurrence interval of great megathrust events.

3.7.2 Onshore versus Offshore Deformation

According to our model results, ~ 37 mm/yr of convergence is accommodated between the Yakutat block and the region north of the Yakataga – Chaix Hills fault system. This convergence rate estimate is compatible with the 80 km of shortening over the Pleistocene suggested by the reconstructions of *Pavlis et al.* [2004]. Both of these

estimates are over six times higher than the estimated convergence across the offshore continuation of the fold and thrust belt, the Pamplona zone. Using kinematic reconstruction and depth converted seismic reflection images, *Worthington et al.* [2010] found that the Pamplona zone has accommodated 6 – 8 km of shortening over the Pleistocene, equivalent to an average of 3 – 5 mm/yr of convergence. *Worthington et al.* [2010] suggested that the discrepancy could be explained by convergence being accommodated on the Yakutat decollement at depth or by the majority of present day convergence being accommodated by onshore structures. This latter idea has been proposed by *Chapman et al.* [2008], who postulated that the active deformation in the orogen migrated toward the onshore fold and thrust belt in response to increased levels of glacial erosion since the late Pliocene.

We propose layer parallel shortening as an alternative mechanism that could account for some of the difference between the onshore and offshore convergence estimates. Not recorded in the discrete deformation, layer parallel shortening is the result of porosity loss and dewatering of the sediments upon approach to the deformation front as well as during the accretionary process. *Gulick et al.* [1998] showed an example from the southern Cascadia subduction zone where the seismic velocity of the accreting sediments increases in advance of the frontal thrust and interpreted this change to be the result of dewatering. In the case of the Yakutat block collision, *Worthington et al.* [submitted] show a distinct increase in the sediment velocities in the seismic reflection data around 45 km in front of the first fold and thrust feature of the Pamplona zone. The average velocities of the entire sediment section at a number of positions within 110 km

of the deformation front are shown in Table 3.6. Sediments within 45 km of the deformation front have significantly faster seismic velocities than those further from the front with the major seismic velocity change occurring between 60 and 45 km.

Using the empirically derived global relationship between normally consolidated siliciclastic sediment velocity and porosity from *Erickson and Jarrard* [1998], we calculated average sediment porosity for each position relative to the deformation front (Table 3.6). These values depend on shale content; we chose a shale fraction of 0.6 and assume that porosity loss as opposed to cementation is the dominant process causing the velocity increase [*Erickson and Jarrard*, 1998]. This is a reasonable assumption for glacially derived siliciclastics. Between 110 and 60 km from the deformation front, the average velocities and porosities are largely equivalent despite the increasing sediment thickness. These values are distinctly different from the velocities and equivalent porosities within the 45 km closest to the deformation front. Porosities in the region located 45 – 60 km from the deformation front, where the greatest change in velocities and therefore porosities occurs, decrease from an average of 30% to an average of 17%. We suggest that this 13% porosity loss over a short distance is due to layer parallel shortening. A 13% porosity loss over 17 km amounts to 2.2 km of shortening. Based on our estimated convergence rate of 37 mm/yr, it would take 460,000 yr for 17 km of convergence, or 2.2 km of shortening, to occur. Assuming these values are valid over the 1.8 My since the late Pliocene/early Pleistocene, 8.5 km of shortening not recorded by discrete deformation has occurred through layer parallel shortening. This is equivalent to an average convergence rate of ~ 5 mm/yr. Combined with the estimate of the

convergence rate across discrete structures given by *Worthington et al.* [2010], the region offshore of the St. Elias orogen may accommodate up to 27% of the predicted convergence. While this value indicates that the majority of the convergence is likely accommodated within onshore structures or perhaps along the Yakutat decollement, it emphasizes the importance of accounting for possible sources of deformation outside of discrete folds and faults.

3.7.3 The Malaspina Foreland Fault Zone

Our block model predicts that ~ 14 mm/yr of convergence is accommodated along the Foreland fault zone crossing the Malaspina Glacier. The southward-migrating aftershock pattern following the 1979 St. Elias earthquake [*Estabrook et al.*, 1992] and current seismicity patterns (Figure 3.2) imply that active deformation continues south of the Malaspina fault. Our model results indicate that the Foreland fault zone is fully creeping. Based on this, we suggest that the boundary represents a deformation zone rather than a discrete fault. The western end of the fault zone approximately corresponds to the zone of increased seismic velocities discussed in the previous section. This may suggest that the Foreland fault zone is the onshore continuation of the distributed deformation in advance of the main deformation front.

3.7.4 Bering Glacier Region Deformation

We include the Bering Deformation Zone as a block in our model. The BDZ is surrounded by what appears to be rigid Elias block and has fully creeping fault boundaries. Its location and lack of sharply defined boundaries raise questions about its tectonic significance and whether our interpretation could be biased by transient strain.

The improbability of detectable transient strain from the postseismic effects of the 1899, 1958, and 1979 has been discussed in a previous section as has our correction for the effects of the 1964 earthquake. Since this region contains the largest surging glacier in North America, there is the possibility that the anomalous residuals we observe around the Bering Glacier are due to the elastic response to load changes associated with a glacial surge instead of tectonics. A previous surge between 1993 – 1995 resulted in significant surface deformation in the area surrounding the glacier [*Sauber et al.*, 2000]. The Bering Glacier began to surge during the second half of 2008, although visual observations of the glacier suggest that this surge is much smaller than the 1993 – 1995 event. In our data set, the GPS sites showing the residuals have different occupation histories: some were visited for the last time in 2008 and some received the last visit in 2009. If the surge was significantly impacting the GPS velocities, the sites with 2009 occupations should have velocities markedly different than the sites with 2008 final visits. This is not the case. Additionally, surge effects should impact sites on both sides of the Bering Glacier as demonstrated by *Sauber et al.* [2000]. In our data set, only sites west of the proposed Bering Glacier structure have the southwestward – directed residuals. Based on these observations, we do not believe the anomalous GPS velocities and model residuals around the western side of the Bering Glacier are solely due to surge effects.

Bruhn et al. [2004] proposed that a north-south trending fault beneath the Bering Glacier served as a major structural boundary within the St. Elias orogen. East of this fault, the fold-and-thrust belt accommodates convergence on multiple faults that likely

sole into the Yakutat decollement. To the west of the fault, superimposed folding and faulting deform the old Yakutat suture (the Chugach – St. Elias fault) and the fold-and-thrust belt. *Bruhn et al.* [2004] reported that the second-phase folds, when mapped in detail, formed elliptical interference patterns that reflected the complexities of sedimentary bedding planes after they had undergone two phases of folding. They suggested that these second phase folds formed as sediments were stripped off the Yakutat block basement and crumpled into the sharp bend in the plate margin formed by the intersection of the megathrust with the old suture along the Chugach – St. Elias fault. *Chapman et al.* [in prep.] suggested that the structurally complex, repeatedly deformed rocks west of the proposed Bering Glacier structure represent the final stage of accretion of the Yakutat block as the sedimentary layers are offscraped and subduction of Yakutat basement begins.

Based on the geological findings of complex, multistage deformation in the region west of the Bering Glacier, it seems entirely plausible that a deformation zone rather than a coherent block surrounds the postulated Bering Glacier structure. The marked change in the GPS velocity field along the northern and western edges of the Bering Glacier likely reflect a combination of elastic effects from multiple faults, including the Bering Glacier structure, as well as distributed deformation from the folding and refolding of the sediment cover.

We found that a single block, the Elias block, could describe the upper plate motion both east and west of the Bering Deformation Zone. A more reasonable kinematic scenario would have the Bering Deformation Zone link to a boundary or

boundaries that would divide the upper plate into multiple blocks. Although the GPS data do not show clear evidence of multiple blocks, a boundary or deformation zone with a very low rate of motion could exist within the Elias block. Reasonable locations for such a boundary include a continuation from the Bering Deformation Zone north through the observed division between the collisional and subduction regimes or a connection between the Bering Deformation Zone and the break in seismicity seen north of Prince William Sound (Figure 3.2). If one of these boundaries does exist, the Bering Deformation Zone could represent the first stage of the breakup of the Elias block.

3.7.5 Collision and Accretion versus Subduction

The location of the transition between the collisional tectonic regime and subduction along the Aleutian megathrust has long been a major question in southern Alaskan tectonics. Our fault model (Figure 3.6) shows a clear division between these two regions. In the east, a series of thrust faults sole out into the Yakutat decollement. Only a small width of the decollement, located north of the thrust faults, is locked and accumulating elastic strain. This system of crustal thrust faults is needed to explain the high strain gradient observed in the GPS velocity field in the eastern half of the orogen. From the Bering Glacier west, crustal faults are not required to explain the GPS data. Instead, wide locked segments of the Yakutat decollement mark the beginning of the Aleutian megathrust and result in the relatively uniform GPS velocities seen in the western orogen. Based on our observations, the supposed transition between the tectonic regimes is actually a very abrupt change.

The division between the collisional/thrust fault regime and subduction aligns with the Gulf of Alaska shear zone (Figure 3.12). This suggests that the different styles of deformation caused by the Yakutat collision onshore extend offshore as well. The Gulf of Alaska shear zone is defined by a series of M7+ earthquakes between 1987 and 1992 that occurred along a north-south trend that coincides with a pre-existing weakness in the Pacific plate, magnetic anomaly 13 [*Lahr et al.*, 1988; Pegler *and Das*, 1996]. Previous studies have suggested that the shear zone is evidence of fragmentation of the Pacific plate in response to the Yakutat collision with southern Alaska [*Lahr et al.*, 1988; *Reece et al.*, 2009; *Elliott et al.*, 2010]. Assuming the various components are coupled, the transition between collision and subduction across the St. Elias orogen could cause differential stress in the Pacific plate, resulting in an Eastern Pacific block east of the shear zone and normal Pacific plate to the west.

3.7.6 Plate Coupling Variations and the 1964 Rupture

In our model, the broad, NW-dipping subduction interface between the Elias block and the Yakutat block begins in the vicinity of the Bering Glacier and extends inland beneath the western St. Elias orogen. Our results imply that the locked portion of the megathrust underlies a much greater portion of southern Alaska than any other study has suggested.

We find significant variation in the preferred degree of coupling on the fault planes across the region (Figure 3.6). The regions north and west of the Bering Glacier display strong coupling. Southwest of the glacier, the degree of coupling is moderate as

is the coupling in the Cordova region. Further north, around Valdez, the coupling again becomes strong.

Suito and Freymueller [2009] presented an interseismic slip estimate that included possible effects from postseismic motion and slow slip events for a subduction interface that extended to the Bering Glacier region. Their model suggests strong coupling near the southern end of the Bering Glacier and more moderate levels of coupling offshore and in the Cordova region, a result in good agreement with our block model. As their model did not extend far inland from the coast, comparison to the remainder of our model subduction interface is not possible.

Many models of the coseismic slip distribution [e.g. *Ichinose et al.*, 2007; *Zweck et al.*, 2002] for the 1964 megathrust event do not extend the rupture planes as far east as the Bering Glacier. *Holdahl and Sauber* [1994] included rupture planes near the southern end of the glacier and geologic coseismic uplift estimates from the area in their inversion for the slip distribution. They found high slip around the Bering Glacier surrounded by more moderate amounts of slip offshore and around Cordova. The coseismic slip model of *Suito and Freymueller* [2009] is based in part on the model geometry and data set of *Holdahl and Sauber* [1994] but suggests low-to-moderate slip around the southern Bering Glacier and higher slip around Cordova. These models support our conclusion that the Yakutat subduction interface extends to the Bering Glacier.

Our results imply that seismic hazard evaluations for the megathrust need to account for the likelihood that the locked subduction interface extends as far east as the Bering Glacier and that the interface appears to be strongly coupled in that region.

3.7.7. Lateral Escape in the Western St. Elias Orogen

In Figure 3.9, the predicted velocities along the Elias block show a clear counterclockwise rotation. This implies lateral escape may be occurring along the forearc of the Aleutian megathrust, beginning in the western St. Elias orogen.

Haeussler et al. [2000] reported on evidence of recent (Pliocene and Quaternary) dextral transpression on structures, including the Castle Mountain fault, within the Cook Inlet basin. These findings went counter to the left-lateral oblique shear expected from the relative motion between the Pacific and North American plates. They suggested that the dextral transpression was driven by the Yakutat collision and resulted in the lateral escape of part of the accretionary complex to the southwest. Our block model shows how the NNW-directed "push" from the colliding Yakutat block can be transformed into lateral escape.

3.8 Conclusions

We have presented a new GPS data set for the St. Elias orogen and used that data to develop a block model for southeast and south central Alaska. The block model provides an integrated kinematic view of the regional tectonics and provides new constraints on seismic hazard evaluation.

The strongest tectonic influence in the region is the collision of the Yakutat block with southern Alaska, which results in ~37 mm/yr of convergence across the St. Elias orogen. In the eastern orogen, this convergence is accommodated across a fairly narrow band of sub-parallel N- and NW-dipping thrust faults. These structures produce high strain gradients across Icy Bay and the Mount St. Elias area. Outboard of the main

deformation front, the Malaspina fault, a small amount of the convergence appears to be accommodated through distributed deformation beneath the Malaspina Glacier and offshore by layer parallel shortening of the sediments.

In the vicinity of the Bering Glacier, the thrust belt transitions into a subduction interface between the Yakutat block and the counterclockwise-rotating Elias block. This transition aligns with the Gulf of Alaska shear zone, supporting the idea that the Pacific plate is fragmenting in response to the Yakutat collision. The locked decollement extends under the entire western orogen and shows a high degree of coupling under the Chugach Mountains and Bering Glacier. There is more moderate coupling offshore and around Cordova. The area surrounding the western and northern edges of the Bering Glacier undergoing distributed deformation, represented by a narrow, southwesterly moving block. At the far western end of the orogen, block velocity predictions suggest crustal extrusion westward along the Aleutian forearc. Our results imply that the whole of southeast and south central Alaska is a mobile margin.

3.9 Acknowledgments

The fieldwork required for this study would not have been possible without Jan Gundersen and Lambert DeGavere of Era Helicopters, George Carter of Coastal Helicopters, Paul Claus of Ultima Thule Outfitters, and Steve Ranney of Orca Adventure Lodge. We thank Wes Wallace, Ron Bruhn, Terry Pavlis, Jay Chapman, and Natasha Ruppert for helpful discussions. Figures were generated with the Generic Mapping Tools software of Wessel and Smith [1998]. This research was funded by NSF Grants EAR-

0409426 and EAR-1009593 and a thesis completion fellowship from the University of Alaska to JE.

3.10 References

Argus, D. F. (2007), Defining the translational velocity of the reference frame of Earth, *Geophys. J. Int., 169*, 830–838, doi:10.1111/j.1365-246X.2007.03344.x.

Berger, A. L., S. P. Gulick, J. A. Spotila, J. M. Jaeger, J. B. Chapman, L. A. Lowe, T. L. Pavlis, K. R. Ridgway, B. Willems, and A. McAleer (2008), Tectonic Response to Late Cenozoic Climate Change: Example of a Glaciated Orogenic Wedge, *Nature Geoscience, 1,* 793 – 799.

Bruhn, R. L, T. L. Pavlis, G. Plafker, and L. Serpa (2004), Deformation during terrance accretion in the Saint Elias orogen, Alaska, *Geol. Soc. Am. Bull., 116,* 771-787, doi:10.1130/B25182.1

Bruns, T. R. (1983), Model for the origin of the Yakutat Block, an accreting terrane in the northern Gulf of Alaska, *Geology*, 11, 718–721, doi:10.1130/0091 7613(1983)11<718:MFTOOT>2.0.CO;2.

Chapman, J. B., T. L. Pavlis, S. Gulick, A. Berger, L. Lowe, J. Spotila, R. Bruhn, M. Vorkink, P. Koons, A. Barker, C. Picornell, K. Ridgway, B. Hallet, J. Jaeger, and J. McCalpin (2008), Neotectonics of the Yakutat collision: Changes in deformation driven by mass redistribution, in *Active Tectonics and Seismic Potential of Alaska, Geophys. Monogr. Ser.*, edited by J. T. Freymueller, P. J. Haeussler, R. Wesson, and G. Ekstrom, AGU, Washington, D. C., pp. 65 – 81.

Chase, C. G. (1978), Plate Kinematics: The Americas, east Africa, and the rest of the World, *Earth Planet. Sci. Lett.*, *37*, 355-368.

DeMets, C., R. G. Gordon, D. Argus, and S. Stein (1994), Effect of recent revisions to the geomagnetic reversal time scale on estimates of current plate motions, *Geophys. Res. Lett., 21*, 2191 – 2194.

Dietrich, R., E. R. Ivins, G. Casassa, H. Lange, J. Wendt, and M. Fritsche (2010), Rapid crustal uplift in Patagonia due to enhanced ice loss, *Earth. Planet Sci. Lett., 289*, 22 –29.

Doser, D. I. (2006), Relocations of earthquakes (1899–1917) in south-central Alaska, *Pure Appl. Geophys., 163*, 1461–1476, doi:10.1007/s00024-006-0085-3.

Doser, D. I., J. R. Pelton, and A. M. Veilleux (1997), Earthquakes in the Pamplona Zone, Yakutat Block, South Central Alaska, *J. Geophys. Res.*, *102*, 24,499-24,511.

Elliott, J. L., C. F. Larsen, J. T. Freymueller, and R. J. Motyka (2010), Tectonic block motion and glacial isostatic adjustment in southeast Alaska and adjacent Canada constrained by GPS measurements, *J. Geophys. Res.*,*115*, B09407, doi:10.1029/2009JB007139.

Erickson, S.N., and Jarrard, R.D., 1998. Velocity-porosity relationships for water saturated siliciclastic sediments. J. Geophys. Res., 103:30385–30406.

Estabrook, C. H., J. L. Nabelek, and A. L. Lerner-Lam (1992), Tectonic Model of the Pacific Plate Boundary in the Gulf of Alaska from Broadband Analysis of the 1979 St. Elias, Alaska, Earthquake and its Aftershocks, *J. Geophys. Res., 97*, 6587-6612.

Ferris, A., G. A. Abers, D. H. Christensen, and E. Veenstra (2003), High resolution image of the subducted Pacific (?) Plate beneath central Alaska, 50–150 km depth, *Earth Planet. Sci. Lett., 214*, 575–588, doi:10.1016/S0012-821X(03)00403-5.

Fletcher, H. (2002), Crustal deformation in Alaska measured using Global Positioning System, Ph.D. dissertation, 135 pp., Univ. of Alaska Fairbanks, Fairbanks.

Freed, A. M., R. Burgmann, E. Calais, J. Freymueller, and S. Hreinsdottir (2006), Implications of deformation following the 2002 Denali, Alaska, earthquake for postseismic relaxation processes and lithospheric rheology, *J. Geophys. Res., 111*, B01401, doi:10.1029/2005JB003894.

Freymueller, J. T., S. C. Cohen, R. Cross, J. Elliott, H. Fletcher, C. Larsen, S. Hreinsdóttir, and C. Zweck (2008), Active deformation processes in Alaska, based on 15 years of GPS measurements, in *Active Tectonics and Seismic Potential of Alaska,* edited by J. T. Freymueller et al., pp. 1–42, AGU, Washington, D. C.

Gulick, S. P. S., A. S. Meltzer, and S. H. Clarke Jr (1998), Seismic structure of the Southern Cascadia subduction zone and accretionary prism north of the Mendocino Triple Junction, *J. Geophys. Res., 103*, 27207 – 27222.

Haeussler, P. J., R. L. Bruhn, and T. L. Pratt (2000), Potential seismic hazards and tectonics of the upper Cook Inlet basin, Alaska, based on analysis of Pliocene and younger deformation, *Geo. Soc. Am. Bull., 112*, 1414-1429.

Holdahl, S. R., and J. Sauber (1994), Coseismic slip in the 1964 Prince William Sound earthquake: A new geodetic inversion, *Pure Appl. Geophys., 142*, 55–82, doi:10.1007/BF00875968.

Horner, R. B. (1983), Seismicity in the St. Elias region of northwestern Canada and southeastern Alaska, *Bull. Seismol. Soc. Am., 73*, 1117–1137.

Ichinose, G., P. Somerville, H. K. Thio, R. Graves, and D. O'Connell (2007), Rupture process of the 1964 Prince William Sound, Alaska, earthquake from the combined inversion of seismic, tsunami, and geodetic data, *J. Geophys. Res., 112*, B07306, doi:10.1029/2006JB004728.

Johnson, K. M., R. Bürgmann, and J. T. Freymueller (2009), Coupled afterslip and visco-elastic flow following the 2002 Denali fault, Alaska earthquake, *Geophys. J. Int., 176*, 670–682, doi:10.1111/j.1365-246X. 2008.04029.x.

Kogan, M. G., and G. M. Steblov (2008), Current global plate kinematics from GPS (1995–2007) with the plate-consistent reference frame, *J. Geophys. Res., 113,* B04416, doi:10.1029/2007JB005353.

Lagoe, M. B., C. H. Eyles, N. Eyles, and C. Hale (1993), Timing of late Cenozoic tidewater glaciation in the far North Pacific, *Geol. Soc. Am. Bull., 105*, 1542–1560, doi:10.1130/0016-7606(1993)105<1542: TOLCTG>2.3.CO;2.

Lahr, J. C., and G. Plafker (1980), Holocene Pacific-North American plate interaction in southern Alaska: Implications for the Yakataga seismic gap, *Geology, 8,* 483-486.

Lahr, J. C., R. A. Page, C. D. Stephens, and D. H. Christensen (1988), Unusual earthquakes in the Gulf of Alaska and fragmentation of the Pacific Plate, *Geophys. Res. Lett., 15*, 1483–1486.

Larsen, C. F., R. J. Motyka, J. T. Freymueller, K. A. Echelmeyer, and E. R. Ivins (2004), Rapid uplift of southern Alaska caused by recent ice loss, *Geophys. J. Int., 158*, 1118–1133, doi:10.1111/j.1365-246X. 2004.02356.x.

Larsen, C. F., R. J. Motyka, J. T. Freymueller, K. A. Echelmeyer, and E. R. Ivins (2005), Rapid viscoelastic uplift in southeast Alaska caused by post-Little Ice Age glacial retreat, *Earth Planet. Sci. Lett., 237*, 548–560, doi:10.1016/j.epsl.2005.06.032.

McCaffrey, R. (2002), Crustal block rotations and plate coupling, in *Plate Boundary Zones*, edited by S. Stein and J. Freymueller, pp. 101–122, AGU, Washington, D. C.

Meade, B. J., and B. H. Hager (2005), Block models of crustal motion in southern California constrained by GPS measurements, *J. Geophys. Res., 110*, B03403, doi:10.1029/2004JB003209.

Minster, J. B., and T. H. Jordon (1978), Present-day Plate Motions, *J. Geophys. Res., 83,* 5331-5353.

Motyka, R. J. (2003), Little ice age subsidence and post little ice age uplift at Juneau, Alaska inferred from dendrochronology and geomorphology, *Quat. Res., 59*, 300 – 309, doi:10.1016/S0033-5894(03)00032-2.

Okada, Y. (1985), Surface deformation due to shear and tensile faults in a half-space, *Bull. Seismol. Soc. Am., 75*, 1135–1154.

Pavlis, T. L., C. Picornell, and L. Serpa (2004), Tectonic Processes During Oblique Collision: Insights from the St. Elias Orogen, Northern American Cordillera, *Tectonics, 23*, TC3001, doi:10.1029/2003TC001557.

Pegler, G., and S. Das (1996), The 1987-1992 Gulf of Alaska earthquakes, *Tectonophysics, 257*, 111–136.

Perez, O. J., and K. H. Jacob (1980), Tectonic model and seismic potential of the eastern Gulf of Alaska and Yakataga Seismic Gap, *J. Geophys. Res., 85*, 7132–7150, doi:10.1029/JB085iB12p07132.

Plafker, G. (1987), Regional geology and petroleum potential of the northern Gulf of Alaska, in *Geology and resource potential of the continental margin of the western North American and adjacent ocean basins – Beaufort Sea to Baja California*, Edited by D. W. Scholl, A. Grantz, and J. G. Vedder, Circum-Pacific Council for Energy and Mineral Resources Earth Science Series, *6*, pp. 229 – 268.

Plafker, G., and D. J. Miller (1957), Reconnaissance geology of the Malaspina district, Alaska: U.S. Geol. Survey Oil and Gas Inv. Map OM-189, scale 1:125,000.

Plafker, G., J. C. Moore, and G. R. Winkler (1994), Geology of the southern Alaska margin, in *The Geology of North America*, vol. G1, *The Geology of Alaska*, edited by G. Plafker and H. C. Berg, pp. 389–449, Geol. Soc. Am., Boulder, Colo.

Plafker, G., T. Hudson, T. R. Bruns, and M. Rubin (1978), Late Quaternary offsets along the Fairweather faults and crustal plate interactions in southern Alaska, *Can. J. Earth Sci., 15*, 805-816.

Plattner, C., R. Malservisi, T. H. Dixon, P. LaFemina, G. F. Sella, J. Fletcher, F. Suarez-Vidal (2007), New constraints on relative motion between the Pacific Plate and Baja California microplate (Mexico) from GPS measurements, *Geophys. J. Int.*, doi:10.1111/j.1365-246X.2007.03494.x.

Pollitz, F. F. (2005), Transient rheology of the upper mantle beneath central Alaska inferred from the crustal velocity field following the 2002 Denali earthquake, *J. Geophys. Res., 110*, B08407, doi:10.1029/2005JB003672.

Reece, R., S. P. Gulick, G. L. Christeson, and L. L. Worthington (2009), Intraplate shearing and basin deformation in the Pacific Plate as a result of the Yakutat Block collision with North America, *Eos Trans. AGU, 90*(52), Fall Meet. Suppl., Abstract T33C–1924.

Sauber, J., S. McClusky, and R. King (1997), Relation of Ongoing Deformation Rates to the Subduction Zone Process in Southern Alaska, *Geophys. Res. Lett., 24*, 2853-2856.

Sauber, J., G. Plafker, B. F. Molnia, and M. A. Bryant (2000), Crustal Deformation Associated with Glacial Fluctuations in the Eastern Chugach Mountains, Alaska, *J. Geophys. Res., 105,* 8055-8077.

Savage, J. C., and M. Lisowski (1986), Strain Accumulation in the Yakataga Seismic Gap, Southern Alaska, *J. Geophys. Res., 91*, 9495-9506.

Savage, J. C., and M. Lisowski (1988), Deformation in the Yakataga Seismic Gap, Southern Alaska, 1980-1986, *J. Geophys. Res., 93*, 4731-4744.

Savage, J. C., M. Lisowski, and W. H. Prescott (1986), Strain Accumulation in the Shumagin and Yakataga Seismic Gaps, Alaska, *Science, 231,* 585-587.

Sella, G. F., S. Stein, T. H. Dixon, M. Craymer, T. S. James, S. Mazzotti, and R. K. Dokka (2007), Observation of glacial isostatic adjustment in "stable" North America with GPS, *Geophys. Res. Lett., 34*, L02306, doi:10.1029/2006GL027081.

Shennan, I., R. Bruhn, and G. Plafker (2009), Multi-segment Earthquakes and Tsunami Potential of the Aleutian Megathrust, *Quat. Sci. Rev., 28*, 7-13.

Spotila, J. A., A. L. Berger (2010), Exhumation at Orogenic Indentor Corners Under Long-term Glacial Conditions: Example of the St. Elias Orogen, Southern Alaska, *Tectonophyics, 490*, 241-256.

Stephans, C. D., J. C. Lahr, K. A. Fogleman, and R. B. Horner (1980), The St. Elias, Alaska, Earthquake of February 28, 1979: Regional Recording of Aftershocks and Short-Term, Pre-Earthquake Seismicity, *Bull. Seis. Soc. Am., 70*, 1607-1633.

Suito, H., and J. T. Freymueller (2009), A viscoelastic and afterslip postseismic deformation model for the 1964 Alaska earthquake, *J. Geophys.Res., 114*, B11404, doi:10.1029/2008JB005954.

Tarr, R. S., and L. Martin (1912), The earthquakes of Yakutat Bay, Alaska in September 1899, *U.S. Geol. Surv. Prof. Pap., 69*, 135 pp.

Wallace, W. K. (2008), Yakataga fold-and-thrust belt: structural geometry and tectonic implications of a small continental collision zone, in *Tectonics and Seismic Hazards of Alaska, Geophys. Monogr. Ser.*, edited by J. T. Freymueller, P. J. Haeussler, R. Wesson, and G. Ekstrom, AGU, Washington, D. C., pp. 237 – 256.

Worthington, L. L., S. P. Gulick, and T. L. Pavlis (2008), Identifying active structures in the Kayak Island and Pamplona Zones: Implications for offshore tectonics of the Yakutat microplate, Gulf of Alaska, in *Tectonics and Seismic Hazards of Alaska, Geophys. Monogr. Ser.*, edited by J. T. Freymueller, P. J. Haeussler, R. Wesson, and G. Ekstrom, AGU, Washington, D. C., pp. 257 – 268.

Worthington, L. L., S. P. S. Gulick, and T. L. Pavlis (2010), Coupled Stratigraphic and Evolution of a Glaciated Orogenic Wedge, Offshore St. Elias Orogen, Alaska, *Tectonics, 29*, TC6013, doi:10.1029/2010TC002723.

Zumberge, J. F., M. B. Heflin, D. J. Jefferson, M. M. Watkins, and F. H. Webb (1997), Precise point positioning for the efficient and robust analysis of GPS data from large networks, *J. Geophys. Res.,102*, 5005–5017, doi:10.1029/96JB03860.

Zweck, C., J. T. Freymueller, and S. C. Cohen (2002), The 1964 great Alaska earthquake: Present day and cumulative postseismic deformation in the western Kenai Peninsula, *Phys. Earth Planet. Inter., 132*, 5–20, doi:10.1016/S0031 9201(02)00041-9.

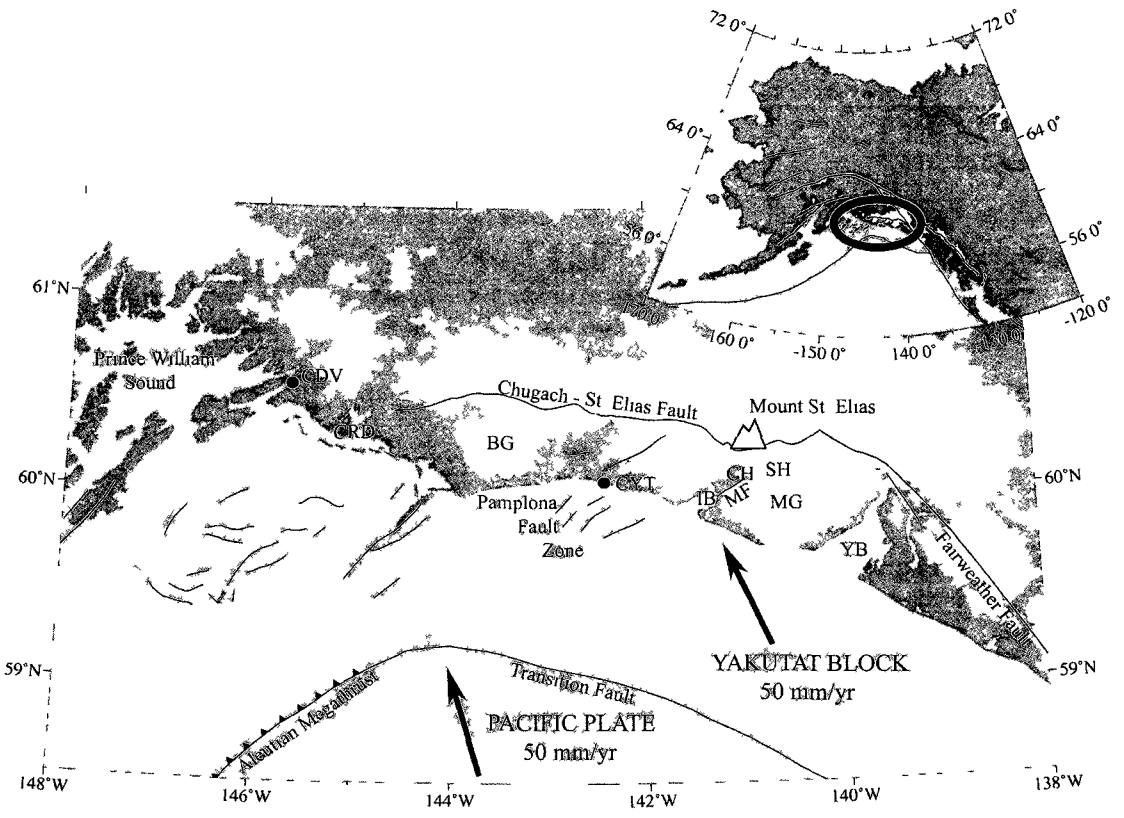

Figure 3.1. Tectonic setting for the St. Elias Orogen. YB is Yakutat Bay, MG is the Malaspina Glacier, MF is the Malaspina Fault, SH is the Samovar Hills, CH is the Chaix Hills, IB is Icy Bay, CYT is Yakataga, BG is the Bering Glacier, CRD is the Copper River Delta, and CDV is Cordova. Yakutat block velocity is from *Elliott et al.* [2010] and the Pacific plate velocity is from *Plattner et al.* [2009].

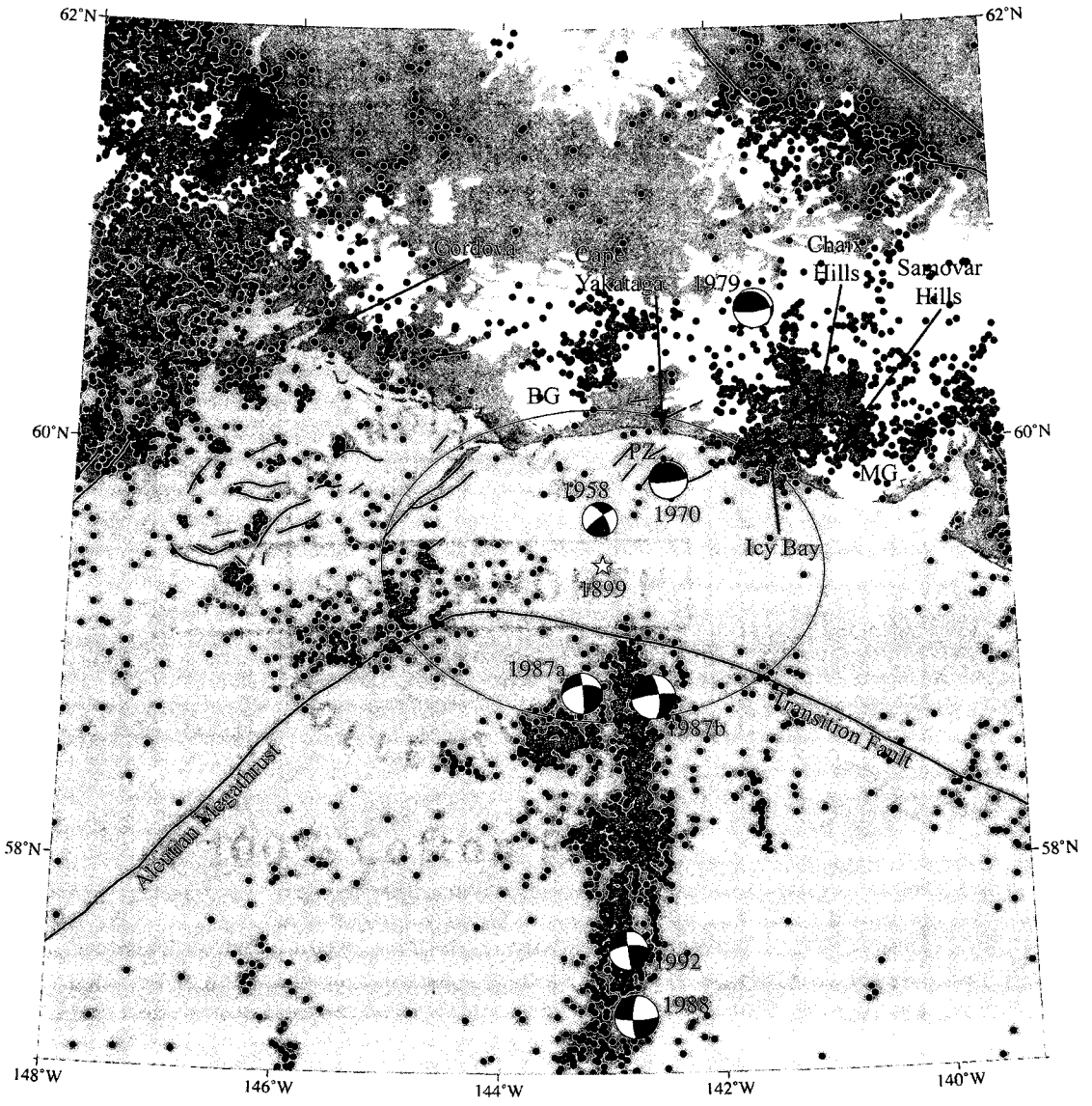

Figure 3.2. Seismicity in the St. Elias region. Green dots are M > 2 events that occurred between 1980 and mid-2005 (when a new seismic network was installed across the orogen). Blue dots are M > 2 events that occurred between mid-2005 and late 2010. Events taken from AEIC catalog. Yellow star (and associated error ellipse) marks the M8 1899 event as relocated by *Doser* [2006]. Focal mechanisms for M > 6 events are shown and are taken from *Estabrook et al.* [1992] (1979), *Doser et al.* [1997] (1958 and 1970), and *Pegler and Das* [1996] (Gulf of Alaska sequence).

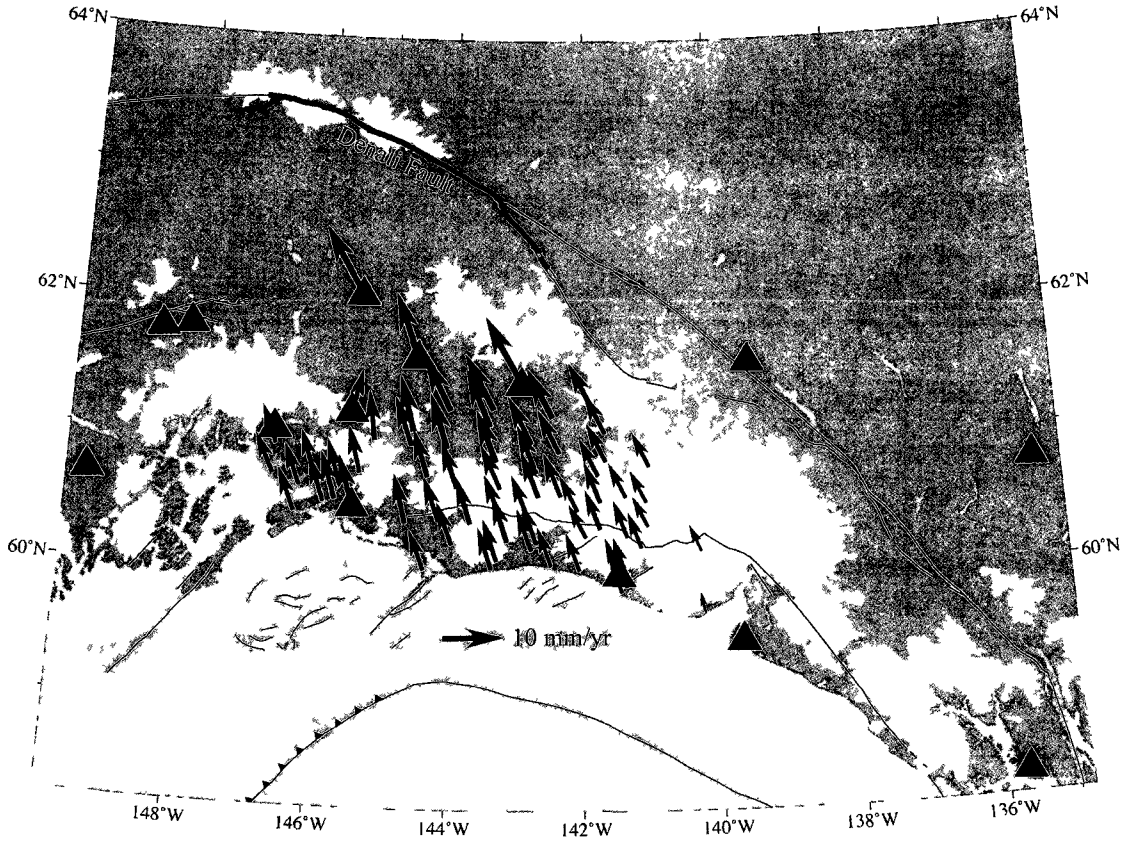

Figure 3.3. Denali fault earthquake postseismic estimate for the St. Elias orogen. Red section of Denali fault shows area ruptured during the 2002 earthquake. Blue triangles show locations of sites used in the postseismic estimate. Red arrows show the predicted Denali postseismic estimates for the sites used in this study.

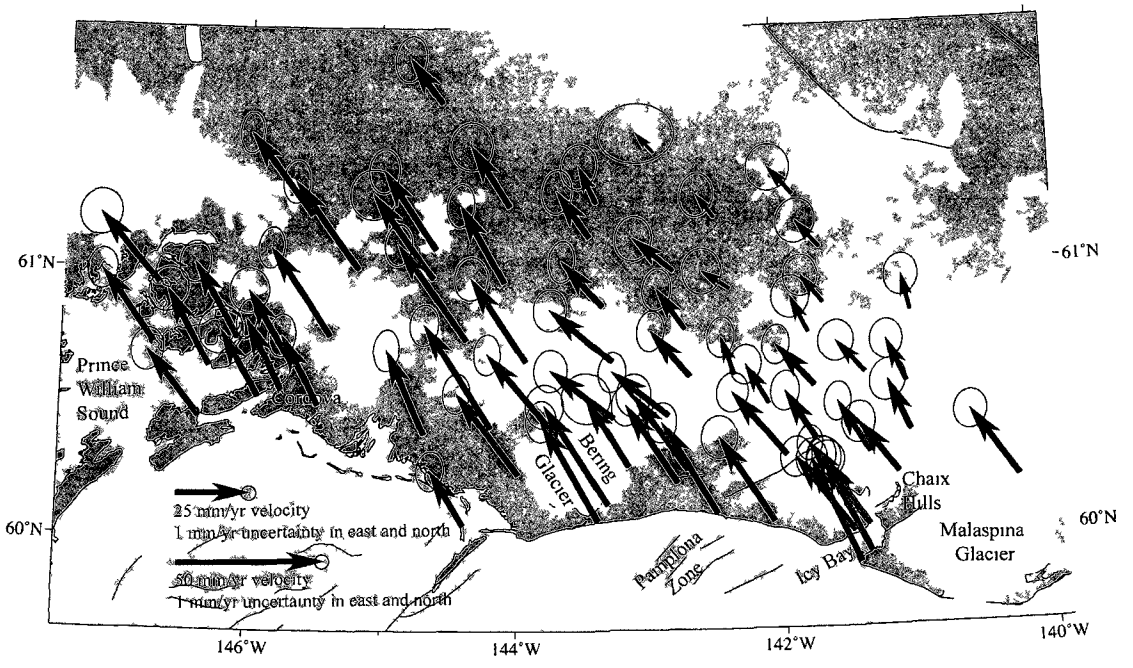

Figure 3 4. GPS velocities with GIA model predictions and postseismic estimates applied for the St. Elias orogen.

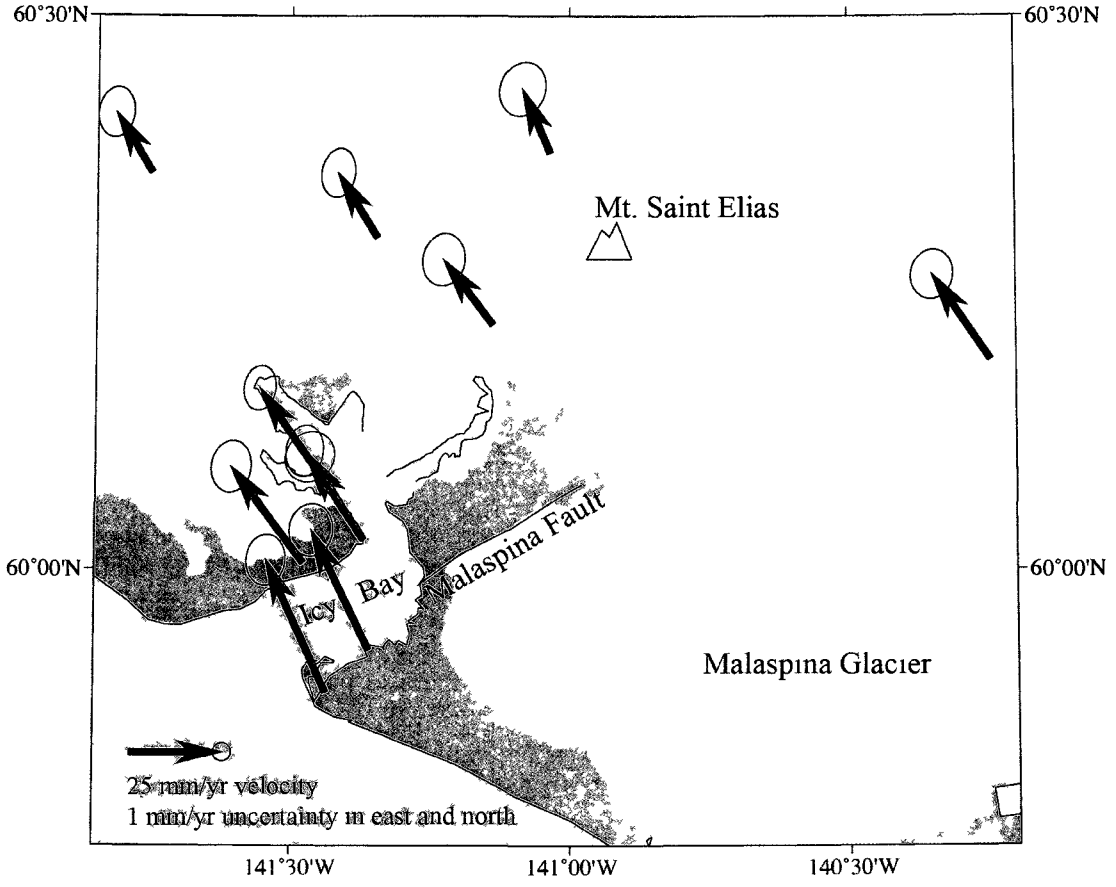

Figure 3.5. GPS velocities in the Icy Bay region.

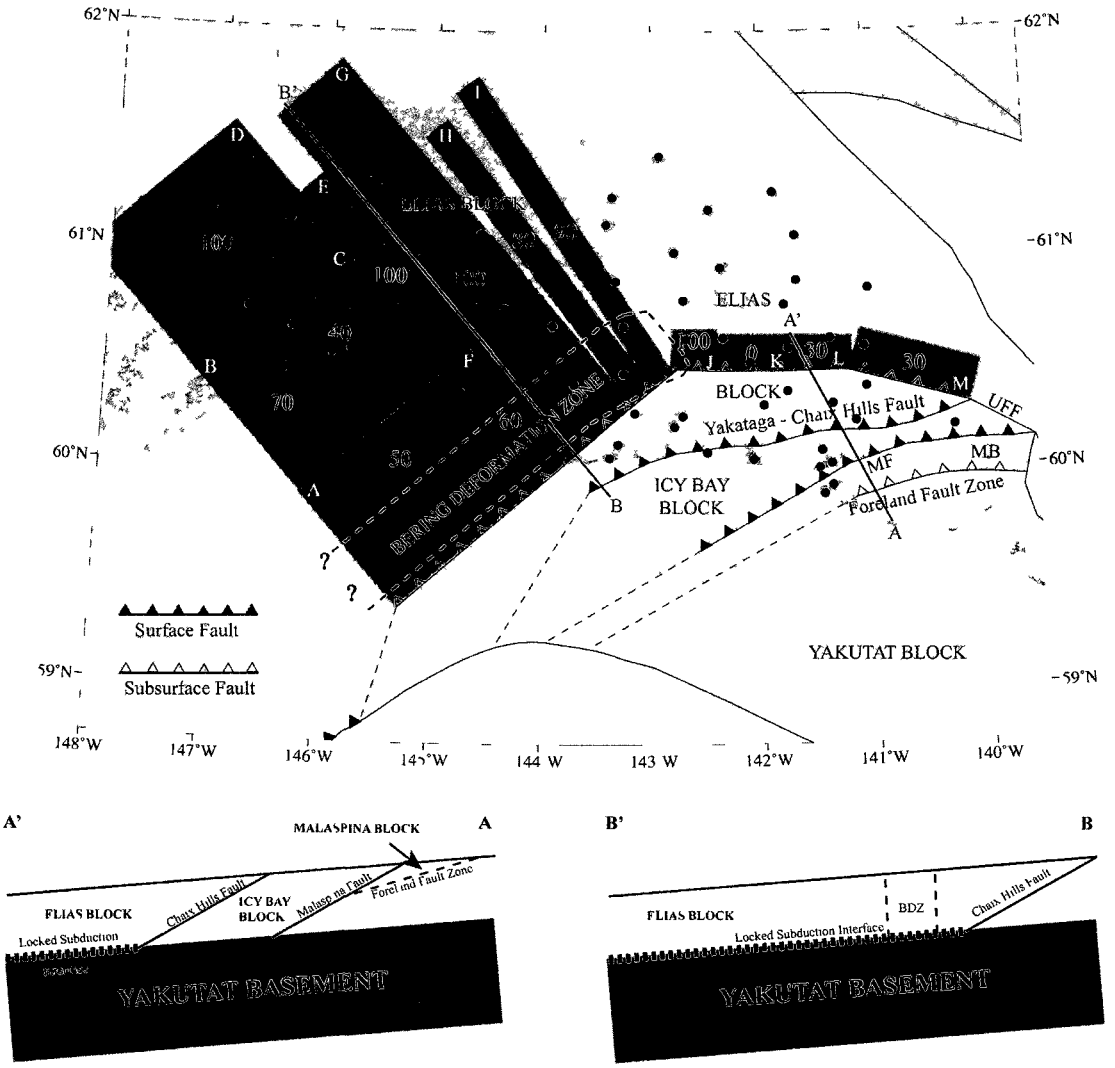

Figure 3.6. Block and fault geometries used in the model. MF is the Malaspina fault, MB is the Malaspina block, UFF is the upper Fairweather fault. Green dots mark the locations of the GPS sites used in this study. Gray rectangles represent the extent of the locked planes of the Yakutat – Elias block subduction interface while black numbers indicate the percent coupling on each plane. Gaps between the northern planes are a result of a curve in the fault geometry and do not affect the model results. Updip ends of the subduction interface are marked by the teeth along the southern edges of the gray rectangles. White letters identify model planes listed in Table 3.4. Crustal faults end at the beginning of the subduction interface. Heavy dashed line marks the limits of the Bering Deformation Zone. Light dashed lines represent inferred fault connections and continuations that are not constrained by our model. Cross sections are schematic and not to scale.

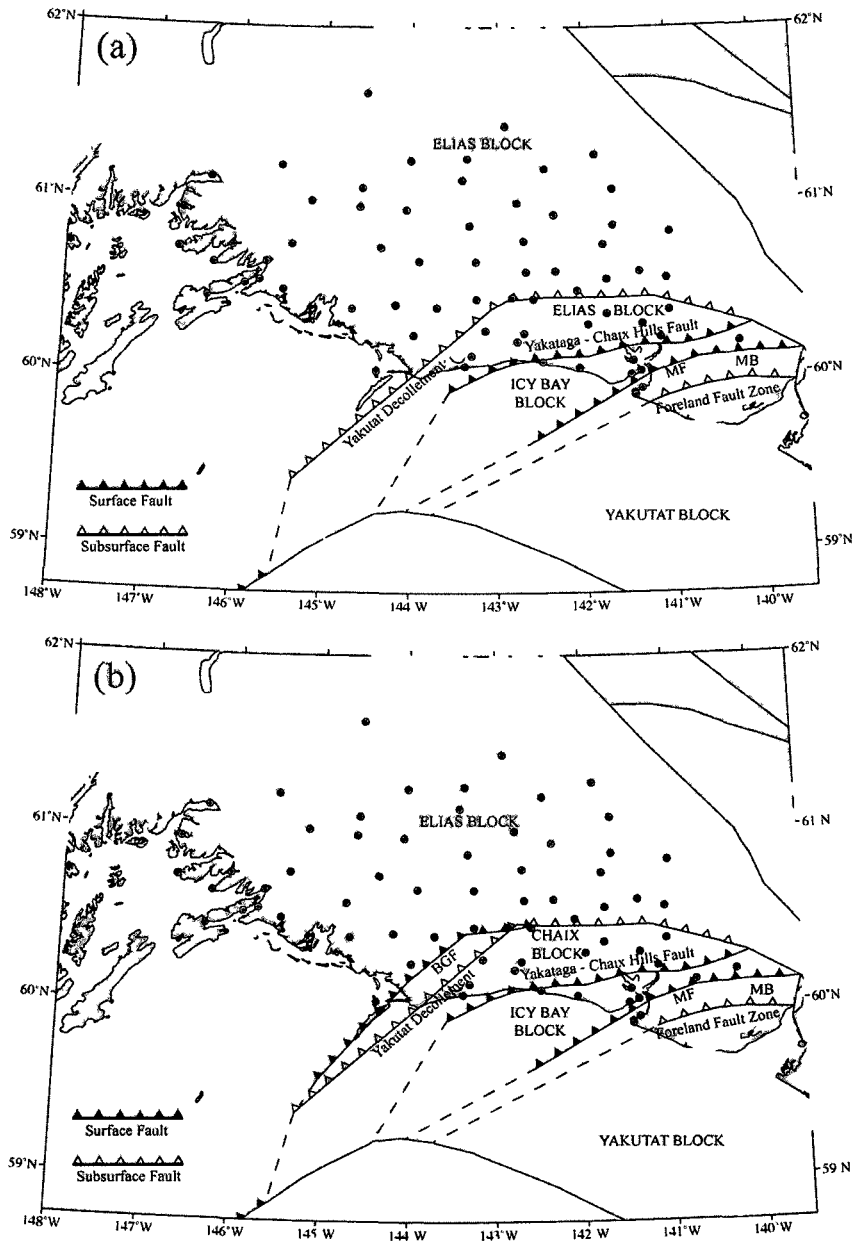

Figure 3.7. Alternate fault geometries. MB is the Malaspina block and MF is the Malaspina fault. Green dots mark the locations of the GPS sites used in this study. (a). Geometry without additional faults or blocks in the Bering Glacier region. (b) Geometry including a thrust fault along the western half of the Bering Glacier. BGF is the Bering Glacier fault.

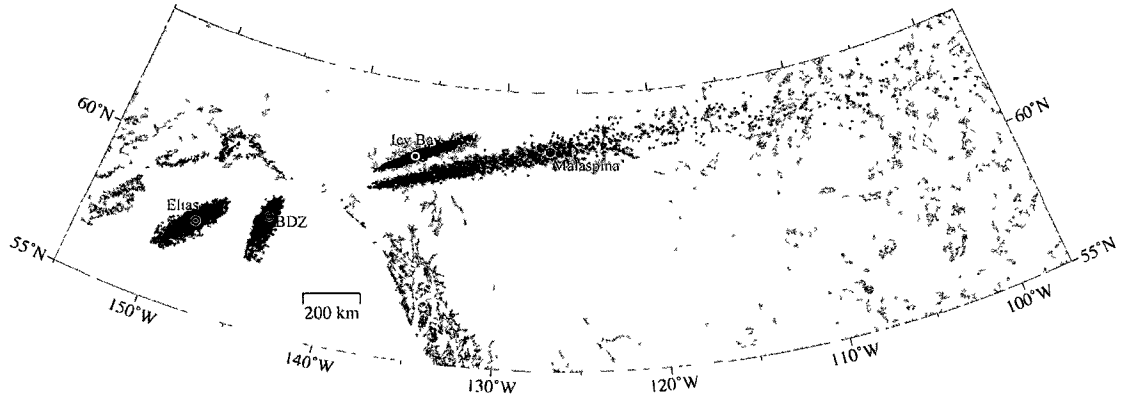

Figure 3.8. Poles and uncertainty estimates. BDZ is the Bering Deformation Zone.

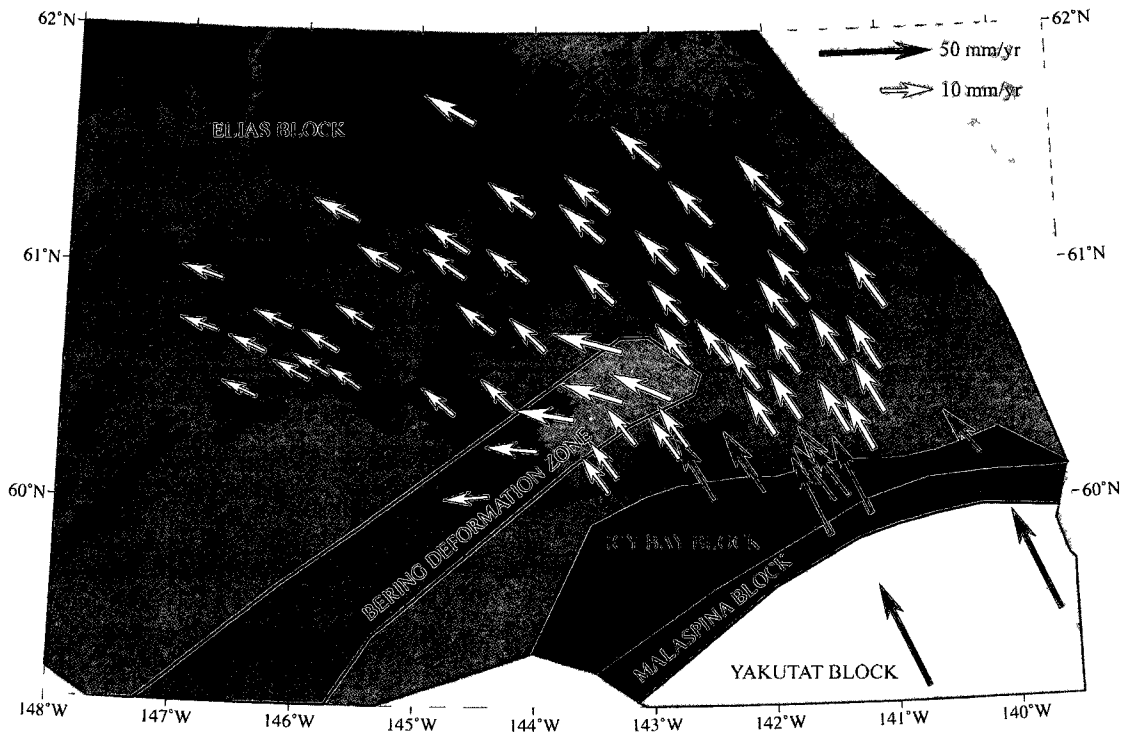

Figure 3.9. Model block velocity predictions for the St. Elias orogen. Note the different scales for the gray and white vectors.

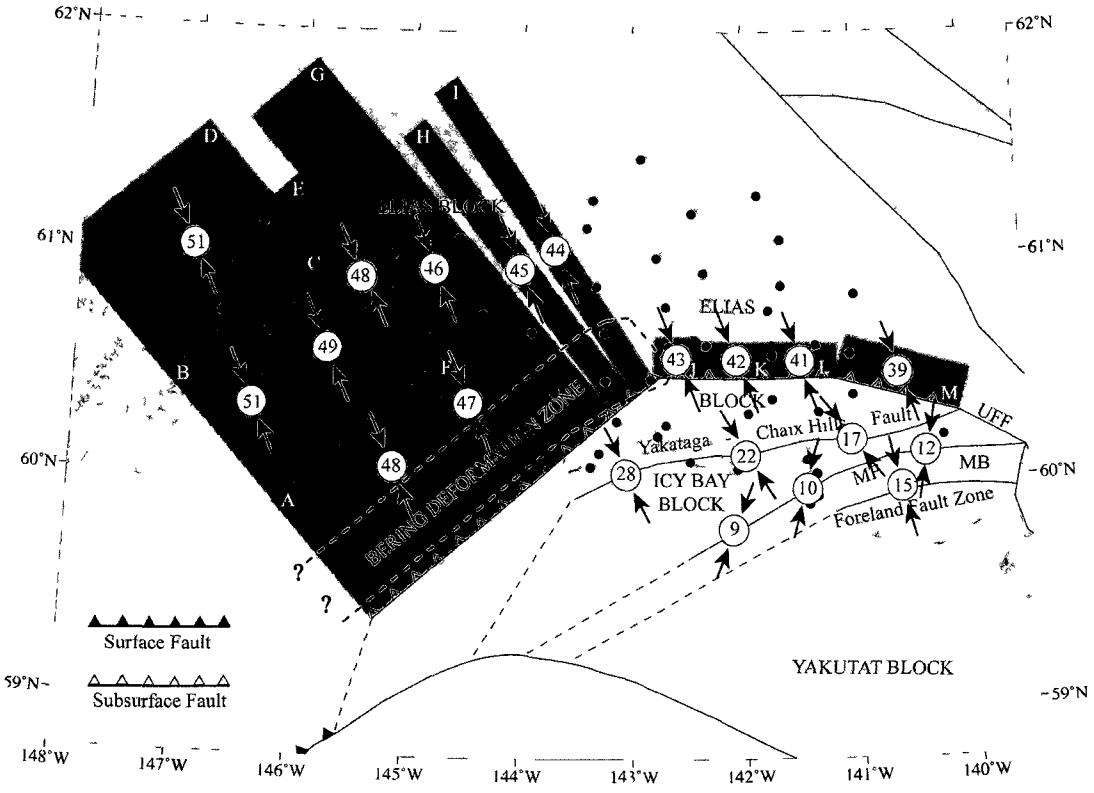

Figure 3.10. Relative block motions in the St. Elias orogen. Numbers in circles are the predicted relative block motions in mm/yr. Arrows show the sense of the relative motion. Coupling estimates have not been applied (see Table 3.4).

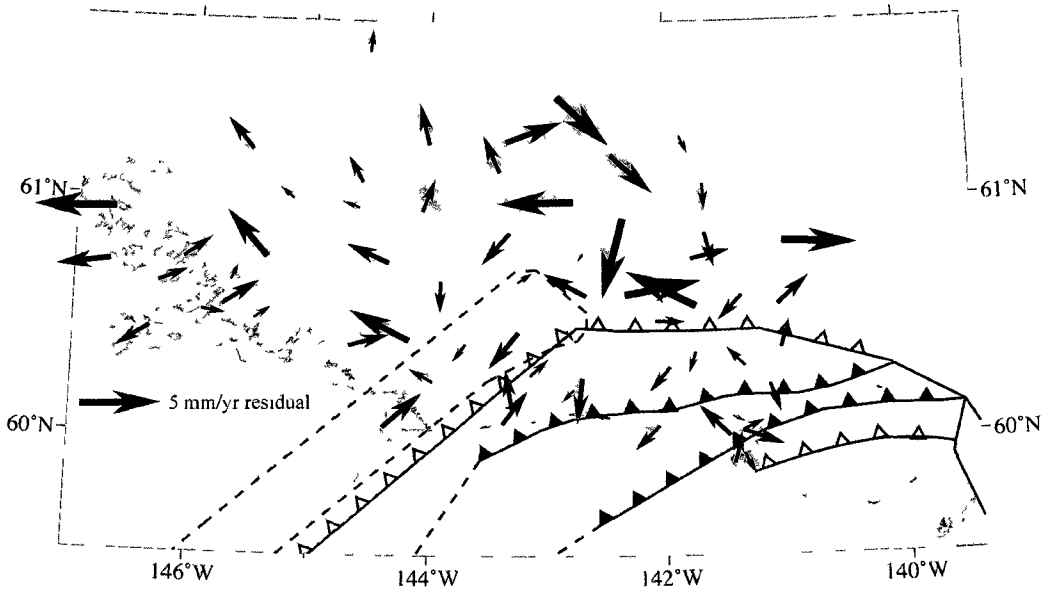

Figure 3.11. Velocity residuals between the data and block model predictions. Data uncertainty ellipses have been omitted for clarity.

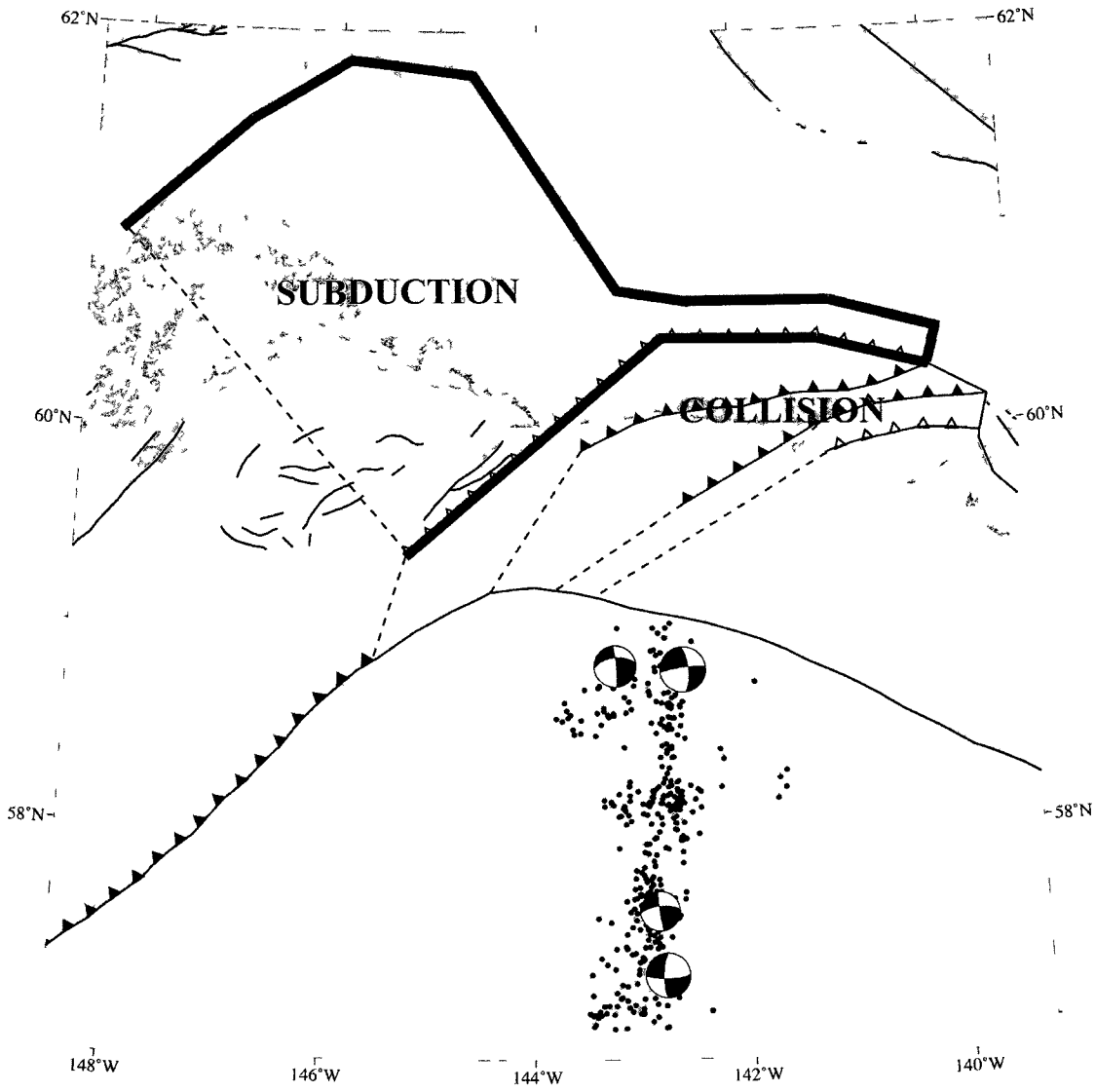

Figure 3.12 Division between tectonic regimes in the St. Elias orogen.

Table 3.1 GPS velocities used in this study, in cm/yr[a]

Site Name	Longitude (°E)	Latitude (°N)	V_{East}	V_{North}	σ_{East}	σ_{North}
3443	-141.35985	59.92709	-1.917	3.657	0.139	0.154
3444	-141.36876	60.02655	-1.866	2.557	0.164	0.154
AFGR	-144.57991	61.07662	-1.492	3.295	0.109	0.140
AMBE	-141.47729	60.00602	-2.302	3.066	0.117	0.144
BAGL	-142.67618	60.59644	-1.334	2.268	0.084	0.132
BERG	-143.70058	60.39395	-2.307	3.198	0.083	0.132
BLF2	-145.67819	60.65179	-1.283	2.796	0.171	0.157
BREM	-144.60559	60.96817	-1.774	3.346	0.221	0.192
BRKN	-141.66120	60.86270	-0.825	1.629	0.128	0.146
CDST	-143.36150	61.24570	-0.659	2.071	0.124	0.147
CHOS	-143.97163	60.23424	-2.201	3.150	0.086	0.134
CODO	-145.47545	60.49372	-1.258	2.892	0.087	0.136
DISA	-141.66980	61.06860	-0.870	1.613	0.160	0.161
DIVD	-143.25350	60.65560	-2.140	2.439	0.120	0.142
DON	-143.37678	60.05785	-2.049	3.822	0.112	0.143
ELIS	-141.05650	60.55850	-0.819	2.123	0.124	0.145
EYAC	-145.74986	60.54870	-1.077	2.769	0.039	0.123
FARO	-143.41450	61.12091	-1.089	2.410	0.090	0.134
FAUS	-144.06609	60.95389	-1.329	3.342	0.082	0.132
GLRY	-144.35220	60.73644	-2.213	3.823	0.087	0.134

GRIS	-146.29200	60.63960	-1.201	2.745	0.169	0.162
GULL	-146.70371	60.72296	-1.557	2.555	0.099	0.140
HAM2	-144.38277	60.04339	-1.253	2.159	0.088	0.135
HANN	-143.14517	60.26061	-1.503	2.905	0.238	0.200
HAWK	-141.86650	61.26800	-0.871	1.618	0.183	0.174
ICBD	-141.74557	60.55415	-1.392	2.141	0.084	0.131
ICE9	-142.83869	60.45030	-1.968	2.080	0.089	0.134
ISLE	-142.34093	60.60122	-0.492	2.005	0.082	0.131
JILL	-145.16981	61.00129	-1.724	3.424	0.096	0.138
KHIT	-143.24904	60.44227	-2.197	2.204	0.127	0.149
KIAG	-142.36060	60.92310	-0.980	1.333	0.160	0.169
KICH	-141.36950	60.02690	-1.942	2.871	0.105	0.143
KUSH	-144.17627	60.40928	-2.297	3.990	0.096	0.137
LARI	-143.32448	60.86197	-1.336	2.346	0.071	0.128
LEPR	-141.96690	60.29490	-2.002	2.669	0.114	0.144
LIBF	-144.53594	61.62019	-0.930	2.218	0.100	0.137
LOGN	-141.00430	60.82380	-0.394	1.883	0.132	0.153
MARO	-142.70719	60.24734	-1.885	3.058	0.138	0.153
MCAR	-142.92043	61.43200	-0.271	0.587	0.448	0.339
MIST	-146.67706	60.94338	-1.659	2.424	0.191	0.176
MNFS	-141.36310	60.59790	-1.117	1.768	0.140	0.152
NATI	-146.07641	60.74500	-1.221	2.756	0.115	0.144

NOYL	-143.30056	60.11815	-2.252	3.809	0.164	0.162
PENU	-142.46470	61.18880	-0.671	1.545	0.115	0.143
PERF	-144.01820	61.23540	-1.287	2.761	0.170	0.168
PONR	-142.78222	60.19904	-1.810	3.114	0.103	0.138
RAG	-144.67728	60.38643	-1.279	3.350	0.079	0.133
RALF	-141.13870	60.22050	-1.618	2.374	0.132	0.152
RIOU	-141.43699	59.88863	-1.816	3.948	0.117	0.145
RKAV	-141.34624	60.29913	-1.308	2.400	0.085	0.133
RUB2	-146.35800	60.44780	-1.620	2.462	0.121	0.149
RUDE	-145.38220	60.75375	-1.814	3.370	0.081	0.133
SILA	-140.24600	60.18860	-1.903	3.170	0.134	0.152
STEG	-142.08900	60.49000	-0.901	1.935	0.109	0.141
STEL	-141.03554	60.37637	-1.008	2.345	0.151	0.171
TANR	-142.78460	60.99210	-1.378	1.878	0.138	0.153
TIME	-142.70506	60.77445	-0.956	2.140	0.090	0.133
TOYU	-141.45004	60.08603	-1.819	2.566	0.086	0.133
TRM2	-145.92160	60.52600	-1.164	2.548	0.207	0.178
TSIN	-145.52823	61.20357	-1.183	2.955	0.096	0.138
WHTU	-142.06695	60.04784	-2.064	3.359	0.151	0.159
WOLV	-143.90750	60.65910	-1.823	3.415	0.127	0.147
YAHT	-141.75167	60.35807	-1.170	2.250	0.094	0.136
YAKR	-142.48645	60.08146	-2.017	3.550	0.105	0.138

YESS	-141.77850	60.75340	-0.682	1.909	0.150	0.154

[a] Velocities are calculated relative to the North America motion estimate of *Sella et al.* [2007]. Velocities do not have postseismic corrections or GIA adjustments applied.

Table 3.2 Occupation histories for GPS sites in the St. Elias orogen

Site	# of Obs.	First Obs.	Last Obs.	Time Span	GPS Observations Per Year					
					< '05	'05	'06	'07	'08	'09
3443	11	2005.53	2008.55	3.02	0	5	0	2	4	0
3444	23	2006.55	2008.58	2.03	0	0	5	4	14	0
AFGR	20	2005.51	2008.69	3.18	0	3	6	5	6	0
AMBE	9	2005.52	2008.56	3.04	0	4	0	2	3	0
BAGL	21	2005.53	2008.64	3.11	0	7	0	0	14	0
BERG	59	2005.54	2008.73	3.19	0	4	4	2	49	0
BLF2	8	2005.39	2009.57	4.18	0	2	0	3	0	3
BREM	20	2004.53	2008.67	4.15	8, '04	0	6	5	1	0
BRKN	16	2006.51	2008.62	2.11	0	0	6	0	10	0
CDST	18	2006.51	2008.55	2.98	0	0	5	0	13	0
CHOS	9	2005.51	2009.67	4.16	0	5	0	0	0	4
CODO	15	2005.42	2009.57	4.17	0	2	4	4	2	3
DISA	10	2006.53	2008.56	2.03	0	0	6	0	4	0
DIVD	35	2006.52	2008.64	2.12	0	0	6	0	29	0
DON	16	2005.52	2008.55	3.03	0	3	3	4	6	0
ELIS	19	2006.51	2008.53	2.03	0	0	8	0	11	0
EYAC	1258	2005.4	2009.7	4.30	0	173	306	246	276	257
FARO	21	2005.54	2008.68	3.15	0	7	5	4	5	0
FAUS	24	2005.51	2008.73	3.22	0	7	0	0	17	0
GLRY	10	2005.51	2009.68	4.18	0	7	0	0	0	3

GRIS	9	2005.39	2009.57	4.18	0	3	0	3	0	3
GULL	10	2005.39	2009.57	4.18	0	3	0	4	0	3
HAM2	8	2005.51	2009.67	4.16	0	4	0	0	0	4
HANN	6	2005.51	2007.55	2.04	0	2	0	4	0	0
HAWK	11	2006.53	2008.56	2.02	0	0	8	0	3	0
ICBD	57	2005.56	2008.7	3.13	0	5	0	0	52	0
ICE9	10	2005.52	2009.68	4.16	0	4	0	0	0	6
ISLE	28	2005.53	2008.63	3.10	0	4	6	3	15	0
JILL	9	2005.51	2008.68	3.18	0	4	0	0	5	0
KHIT	4	2005.55	2009.68	4.13	0	2	0	0	0	2
KIAG	11	2006.53	2008.56	2.02	0	0	8	0	3	0
KICH	19	2005.58	2008.55	2.98	0	5	5	4	5	0
KUSH	8	2005.52	2009.57	4.18	0	4	0	0	0	4
LARI	51	2005.54	2008.67	3.13	0	7	6	7	31	0
LEPR	19	2006.53	2008.58	2.05	0	0	12	0	7	0
LIBF	17	2005.46	2009.52	4.06	0	6	3	3	2	3
LOGN	13	2006.53	2008.55	2.02	0	0	6	0	7	0
MARO	8	2005.53	2008.59	3.06	0	2	0	0	6	0
MCAR	9	2005.81	2009.52	3.71	0	4	0	0	2	3
MIST	19	2005.39	2007.58	2.19	0	3	0	16	0	0
MNFS	15	2006.51	2008.53	2.03	0	0	4	0	11	0
NATI	9	2005.39	2009.57	4.18	0	3	0	3	0	3

NOYL	8	2005.52	2008.51	2.99	0	3	0	0	5	0
PENU	17	2006.53	2008.54	2.01	0	0	9	0	8	0
PERF	9	2006.51	2008.68	2.17	0	0	6	0	3	0
PONR	44	2005.53	2008.73	3.19	0	4	0	0	40	0
RAG	23	2005.51	2008.62	3.11	0	6	2	2	13	0
RALF	15	2005.58	2008.57	2.99	0	3	6	2	4	0
RIOU	11	2005.53	2008.51	2.98	0	5	0	4	2	0
RKAV	19	2005.56	2008.54	2.98	0	6	0	0	13	0
RUB2	7	2005.39	2009.57	4.18	0	2	0	3	0	2
RUDE	8	2005.51	2009.67	4.17	0	4	0	0	0	4
SILA	19	2006.55	2008.58	2.03	0	0	5	6	8	0
STEG	21	2006.51	2008.54	2.03	0	0	10	0	11	0
STEL	14	2006.51	2008.52	2.01	0	0	7	0	7	0
TANR	16	2006.51	2008.64	2.13	0	0	5	0	11	0
TIME	26	2005.53	2008.55	3.02	0	7	4	5	10	0
TOYU	13	1993.47	2008.58	15.1	5, '93	0	0	0	8	0
TRM2	6	2005.39	2009.57	4.17	0	2	0	3	0	1
TSIN	18	2005.46	2009.65	4.19	0	6	4	2	3	3
WHTU	11	2005.53	2008.59	3.06	0	2	0	3	6	0
WOLV	9	2006.52	2009.68	3.16	0	0	6	0	0	3
YAHT	13	2005.56	2008.57	3.01	0	6	0	0	7	0
YAKR	25	2005.52	2008.53	3.01	0	2	9	2	12	0

YESS	12	2006.53	2008.56	2.02	0	0	5	0	7	0

Table 3.3 Denali postseismic estimates, in cm/yr

Site	Longitude (°E)	Latitude (°N)	V_{East}	V_{North}
3443	-141.35985	59.92709	-0.19	0.56
3444	-141.36876	60.02655	-0.26	0.43
AFGR	-144.57991	61.07662	-0.23	0.91
AMBE	-141.47729	60.00602	-0.22	0.61
BAGL	-142.67618	60.59644	-0.28	0.74
BERG	-143.70058	60.39395	-0.24	0.76
BLF2	-145.67819	60.65179	-0.22	0.75
BREM	-144.60559	60.96817	-0.27	0.79
BRKN	-141.66120	60.86270	-0.31	0.62
CDST	-143.36150	61.24570	-0.47	0.91
CHOS	-143.97163	60.23424	-0.25	0.68
CODO	-145.47545	60.49372	-0.24	0.85
DISA	-141.66980	61.06860	-0.33	0.66
DIVD	-143.25350	60.65560	-0.32	0.72
DON	-143.37678	60.05785	-0.22	0.67
ELIS	-141.05650	60.55850	-0.25	0.51
EYAC	-145.74986	60.54870	-0.24	0.76
FARO	-143.41450	61.12091	-0.39	0.94
FAUS	-144.06609	60.95389	-0.28	0.90
GLRY	-144.35220	60.73644	-0.24	0.77

GRIS	-146.29200	60.63960	-0.25	0.68
GULL	-146.70371	60.72296	-0.29	0.64
HAM2	-144.38277	60.04339	-0.25	0.65
HANN	-143.14517	60.26061	-0.24	0.76
HAWK	-141.86650	-61.26800	-0.37	0.73
ICBD	-141.74557	60.55415	-0.26	0.66
ICE9	-142.83869	60.45030	-0.26	0.68
ISLE	-142.34093	60.60122	-0.28	0.72
JILL	-145.16981	61.00129	-0.11	0.83
KHIT	-143.24904	60.44227	-0.26	0.69
KIAG	-142.36060	60.92310	-0.35	0.72
KICH	-141.36950	60.02690	-0.21	0.59
KUSH	-144.17627	60.40928	-0.25	0.72
LARI	-143.32448	60.86197	-0.32	0.85
LEPR	-141.96690	60.29490	-0.27	0.53
LIBF	-144.53594	61.62019	-0.39	1.07
LOGN	-141.00430	60.82380	-0.26	0.55
MARO	-142.70719	60.24734	-0.24	0.68
MCAR	-142.92043	61.43200	-0.61	1.13
MIST	-146.67706	60.94338	-0.22	0.61
MNFS	-141.36310	60.59790	-0.27	0.55
NATI	-146.07641	60.74500	-0.22	0.69

NOYL	-143.30056	60.11815	-0.22	0.68
PENU	-142.46470	61.18880	-0.41	0.81
PERF	-144.01820	61.23540	-0.44	0.90
PONR	-142.78222	60.19904	-0.23	0.67
RAG	-144.67728	60.38643	-0.20	0.81
RALF	-141.13870	60.22050	-0.21	0.57
RIOU	-141.43699	59.88863	-0.19	0.56
RKAV	-141.34624	60.29913	-0.22	0.60
RUB2	-146.35800	60.44780	-0.28	0.69
RUDE	-145.38220	60.75375	-0.19	0.75
SILA	-140.24600	60.18860	-0.19	0.41
STEG	-142.08900	60.49000	-0.29	0.59
STEL	-141.03554	60.37637	-0.24	0.48
TANR	-142.78460	60.99210	-0.38	0.78
TAZL	-145.43289	62.07986	-0.65	1.12
TIME	-142.70506	60.77445	-0.31	0.78
TOYU	-141.45004	60.08603282	-0.12	0.33
TRM2	-145.92160	60.52600	-0.25	0.74
TSIN	-145.52823	61.20357	0.15	0.69
WHTU	-142.06695	60.04784	-0.22	0.61
WOLV	-143.90750	60.65910	-0.26	0.76
YAHT	-141.75167	60.35807	-0.24	0.64

YAKR	-142.48645	60.08146	-0.22	0.64
YESS	-141.77850	60.75340	-0.30	0.61

Table 3.4 Model fault geometry parameters

Fault Segment	Dip (°)	Width (km)[a]	Depth (km)[b]	% Coupling
Foreland Fault Zone	5	0	0.5	0
Malaspina (Offshore)	20	45	0	100
Malaspina (Icy Bay)	20	10	0	0
Malaspina (Samovar Hills)	15	10	0	100
Malaspina (Samovar Hills to Fairweather fault)	15	10	0	30
Yakataga (Offshore)	15	20	0	100
Yakataga (Coast to W. Icy Bay)	10	25	0	100
Yakataga (W. Icy Bay to Samovar Hills)	30	12	0	100
Yakataga (Samovar Hills to Fairweather fault)	30	0	0	0
Yakutat Decollement A	5	54	11.5	50
Yakutat Decollement B	5	78	16.5	70
Yakutat Decollement C	5	78	16.5	40
Yakutat Decollement D	5	85	23.5	100
Yakutat Decollement E	5	110	16.5	100
Yakutat Decollement F	5	54	11.5	60
Yakutat Decollement G	5	200	11.5	100
Yakutat Decollment H	5	132	12.5	80
Yakutat Decollement I	5	150	14.5	90

Yakutat Decollement J	5	20	15	100
Yakutat Decollement K	5	18	15	0
Yakutat Decollement L	5	18	15	30
Yakutat Decollement M	5	20	15	30

[a] Fault width is in down-dip direction
[b] Depth is to top of fault plane

Table 3.5. Block poles, rotation rates, angular velocities, and uncertainties

Block	Latitude (°N)	Longitude (°E)	Rate (deg/My)	Omega (X,Y,Z) (10^3 rad/My)	Omega Covariance (xx,xy,xz,yy,yz,zz) (10^6 rad/My^2)
Malaspina	62 1	-126 92	-2 71 ± 3 54	13 31, 17 71, -41 84	606 26, 482 80, -1327 60, 384 55, -1057 30, 2907 50
Icy Bay	61 59	-135 91	-4 94 ± 1 09	29 45, 28 53, -75 82	55 54, 43 88, -122 43, 34 70, -96 77, 269 94
BDZ	58 71	-144 21	3 83 ± 1 03	-28 17, -20 31, 57 13	51 46, 37 94, -111 52, 28 00, -82 25 241 75
Elias	57 87	-148 36	1 40 ± 0 22	-11 08, -6 83, 20 73	2 32, 1 74, -5 18, 1 31, -3 90, 11 60

Table 3.6. Sediment characteristics relative to distance from deformation front.

Distance (km)	Thickness (km)	Velocity (km/s)	Porosity (%)
4.232	7.375	3.241	18.74
9.247	7.913	3.366	16.71
14.262	8.462	3.448	15.48
19.276	8.359	3.45	15.45
24.291	8.076	3.346	17.03
29.306	8.246	3.443	15.55
34.321	8.126	3.404	16.14
39.335	7.952	3.358	16.84
44.35	7.659	3.264	18.35
49.365	7.252	3.109	21.09
54.379	6.301	2.724	27.72
59.394	5.596	2.539	29.05
64.409	5.283	2.478	29.36
69.424	4.983	2.379	29.81
74.438	4.625	2.314	30.07
79.453	4.525	2.309	30.09
84.468	4.275	2.246	30.33
89.482	4.09	2.201	30.49
94.497	4.257	2.263	30.26
99.512	4.461	2.411	29.67
104.526	4.261	2.374	29.83
109.541	4.251	2.409	29.68

Chapter 4

The Influence of the Yakutat Block on Southern Alaska

4.1 General

The combined GPS velocity field for the St. Elias orogen and southeast Alaska (Figure 4.1) and the block model predictions for those regions (Figure 4.2) offer a snapshot of the present-day tectonics and a window into each stage of the Yakutat block's interaction with southern Alaska. These results provide answers to the questions set out in the introduction about the Yakutat block and its effect on the tectonics of southern Alaska.

What is the velocity of the Yakutat block? The Yakutat block itself moves at a rate of 50 mm/yr towards N23W. This velocity has a magnitude that is almost identical to that of the Pacific plate, but the Yakutat block moves at an azimuth ~ 10° more westerly than that plate. While small, this difference results in relative motion between the Yakutat block and the Pacific plate that may be accommodated along the Gulf of Alaska shear zone and the Transition fault.

What are the boundaries of the Yakutat block? The Transition fault forms the southern boundary of the Yakutat block while the Malaspina – Pamplona system serves as the fully developed western and northern boundaries. Along the block's eastern edge, the deformation zone represented by the Nunatak and Foothills blocks separates the Yakutat block from the Fairweather fault.

What is the current deformation front between the Yakutat block and southern Alaska? The present-day deformation front occurs in two stages: a fully developed thrust fault along the Malaspina – Pamplona system and an incipient front along the Foreland fault zone and its offshore continuation.

How is the relative plate motion partitioned between various structures? Where are the active structures? The majority of the relative plate motion in the region is accommodated along major boundary faults such as the Fairweather – Queen Charlotte system or within narrow bands of faults such as the Malaspina – Pamplona system and the Yakataga – Chaix Hills system. The remaining relative plate motion is distributed between a number of structures including the Transition fault, the Foothills thrust fault, the Boundary fault, and the Eastern Denali fault. Crustal faulting in the St. Elias orogen is concentrated in the southern part of the region.

Where does the transition from collision to subduction occur? Instead of a transition, there is an abrupt shift between the two tectonic regimes near the Bering Glacier. There, crustal thrust faults and a high strain gradient give way to a broad subduction interface and a relatively uniform GPS velocity field.

What are the far-field effects of the Yakutat collision? These effects include clockwise rotation of the Fairweather and Baranof blocks, northeasterly motion in the Northern Cordillera, counterclockwise rotation of the Elias block, possible lateral escape of material at the western end of the orogen, and fragmentation of the Pacific plate along the Gulf of Alaska shear zone.

While *Chapman et al.* [in prep.] suggested that the geologic data offered an along-strike record of accretion in the St. Elias orogen, the GPS results also give a view into the residual effects of the collision south of the current deformation front and in the far field. At the southern end of southeast Alaska, the relatively simple deformation observed is a result of motion between the coastal region and the Pacific plate. The Yakutat block has fully migrated past this area and no longer has a strong direct influence on the crustal movements. Closer to the deformation front, the tectonic signal is dominated by the transform fault system, but the Yakutat block is fragmenting along its eastern edge and proximity to the deformation front is causing the area inboard of the transform system to rotate clockwise into the Northern Cordillera. Just outboard of the active deformation front, distributed deformation is occurring, marking the beginning of the main collisional zone and indicating possible locations of developing structures. From the active deformation front along the Pamplona – Malaspina system to the central part of the orogen, collisional tectonics dominates the GPS signal as a series of en echelon faults accommodates oblique convergence. A portion of the strain is transferred north of the fault system and results in a counterclockwise rotation towards Prince William Sound. To the west, beginning near the Bering Glacier, the collisional regime transitions into a locked Yakutat decollement that extends a significant distance towards the northwest. The deformation observed around the Bering Glacier could represent the last phase of accretion as sedimentary cover on the Yakutat block is stripped and complexly deformed prior to subduction of Yakutat basement.

These results show many advances in understanding when compared to previous studies and tectonic models for the region. *Fletcher and Freymueller* [1999] presented a model that included a Yakutat block that moved 44 mm/yr towards N37°W, a result quite different from the usual assumption that the Yakutat block moved with the Pacific plate. They suggested that the Transition fault accommodated the ~ 20 mm/yr of Yakutat block – Pacific plate relative motion. Their Yakutat block velocity was equal to the GPS velocity at a site in the city of Yakutat and they did not account for the effects of glacial isostatic adjustment. Using data from a small network of GPS and EDM sites near the Fairweather fault and three GPS sites in the Northern Cordillera, *Fletcher and Freymueller* [2003] estimated slip rates for the Fairweather and Eastern Denali faults. Their model assumed that the region east of the Eastern Denali fault was stable North America and that the Fairweather block moved parallel to the faults. They had no data from sites on the Fairweather block.

In contrast, the results in this study are based on data from an extensive network of GPS sites covering southeast Alaska and the adjacent region of Canada and the effects of glacial isostatic adjustment were taken into account. The block modeling technique allowed the simultaneous estimation of block velocities and slip rates. Our estimated Yakutat block velocity is faster and more northerly, leading to a smaller, but still significant, amount of relative motion between that block and the Pacific plate. That relative motion is partitioned between several onshore and offshore structures instead of being solely accommodated along the Transition fault. This work revealed the details of the tectonic motion away from the main boundaries. Clockwise rotation of the area

inboard of the Fairweather fault is clearly seen, as is the northeasterly motion of the Northern Cordillera, indicating that stable North America must lie further east. This, in turn, implies that the whole southern Alaska margin is mobile.

Fletcher [2002] suggested that the area south of the Denali fault was the counterclockwise rotating Southern Alaska block. The pole of rotation for this block was adopted from *Stout and Chase* [1980] and the rotation rate was determined from GPS-derived slip rates on the Denali fault (which forms a small circle about the pole). The region north of the Denali fault was assumed to be stable North America and no postseismic effects from the M9.2 1964 earthquake were considered. In our model, both the pole and rotation rate of the Elias block are estimated using data from the St. Elias network that has been corrected for postseismic and glacial isostatic adjustment effects. The resulting pole is further south than that of *Stout and Chase* [1980] and the rotation rate is several times faster than that determined by *Fletcher* [2002]. This could mean that a boundary exists between the Elias block and the Southern Alaska block to the north of our study area. Alternatively, the Elias block and Southern Alaska block could be a single block whose pole and rotation rate need to be re-estimated using the block modeling technique, the expanded data set, and postseismic corrections. It is beyond the scope of the present study to determine which possibility is correct.

The geodetic studies of *Sauber et al.* [1997] and *Savage and Lisowski* [1986] used data from small networks of GPS and EDM sites in the St. Elias orogen to constrain a regional tectonic model. *Sauber et al.* [1997] explained the deformation field using a combination of subduction offshore the orogen and right-lateral shear in the northern part

of the orogen. They assumed subduction occurred at a rate and azimuth equal to the Pacific plate – North America relative motion and that the upper plate was North America. *Savage and Lisowski* [1986] also assumed the subduction interface was between the Pacific plate and North America, with the Yakutat block treated as part of North America. In the northern part of the orogen, they also suggested that right-lateral shear might be present.

The much more extensive data network used in our study clearly shows that subduction alone cannot explain the observed strain gradient in the eastern St. Elias orogen. Crustal faults with oblique slip are required. In addition, the subduction interface in our model is between the Yakutat block and the Elias block. The need for right-lateral shear is obviated by our use of the Yakutat block as the downgoing plate and the rotation of the Elias block.

In addition to refinements to previous models, this study has presented a number of new results. The rotation inboard of the Fairweather – Queen Charlotte system is clearly defined, which directly links strain from the Yakutat collision to the observed deformation in the Northern Cordillera. The extent of the "rigid" Yakutat block and the location of the present-day deformation front between the Yakutat block and southern Alaska have been determined. Concentrated areas of shortening have been identified within the eastern St. Elias orogen and fault slip deficit rates for structures accommodating this shortening have been estimated. The division between the complicated collisional tectonic regime and relatively simple subduction has been delineated and linked to possible fragmentation of the Pacific plate. Having the

subduction interface begin near the Bering Glacier puts this feature further east than usually assumed and the interface extends much farther inland beneath the western St. Elias orogen than other studies have suggested. The Bering Glacier region has been recognized as a possible deformation zone between the two tectonic regimes. This deformation zone may represent the final stage of accretion of the sedimentary layers of the Yakutat block or could indicate that the Elias block is beginning to fragment.

While this work has answered many questions about the tectonics of southern Alaska and the role of the Yakutat block, a number of puzzles remain to be solved. The Yakutat block is apparently subducting beneath Prince William Sound, but where does the transition between Yakutat subduction and Pacific plate subduction occur along the Aleutian megathrust? Are the Elias block and the Southern Alaska block part of the same block, or is there a boundary between them? The sparseness of the GPS network leads to a lack of constraints on the tectonic motions in the northeastern part of our study area. How is the strain from the Yakutat block transferred into this region around the Eastern Denali fault? What kind of motion might there be along the postulated Totshunda – Fairweather Connector fault? How do this study's conclusions about the division between collisional and subduction regimes and the extent of the subduction interface tie into the Wrangell volcanic field? Future studies can build on the results presented here to find solutions to these problems.

4.2 References

Fletcher, H. (2002), Crustal deformation in Alaska measured using Global Positioning System, Ph.D. dissertation, 135 pp., Univ. of Alaska Fairbanks, Fairbanks.

Fletcher, H. J, and J. T. Freymueller (1999), New constraints on the motion of the Yakutat Block, *Geophys. Res. Lett., 26*, 3029-3032.

Fletcher, H. J., and J. T. Freymueller (2003), New constraints on the motion of the Fairweather Fault, Alaska, from GPS Observations, *Geophys. Res. Lett.*, *30*(3), doi:10.1029/2002GL016476.

Sauber, J., S. McClusky, and R. King (1997), Relation of Ongoing Deformation Rates to the Subduction Zone Process in Southern Alaska, *Geophys. Res. Lett., 24*, 2853-2856.

Savage, J. C., M. Lisowski, and W. H. Prescott (1986), Strain Accumulation in the Shumagin and Yakataga Seismic Gaps, Alaska, *Science, 231,* 585-587.

Stout, J. H., and C. G. Chase (1980), Plate kinematics of the Denali fault system, *Can. J. Earth Sci.*, *17*, 1527-1537.

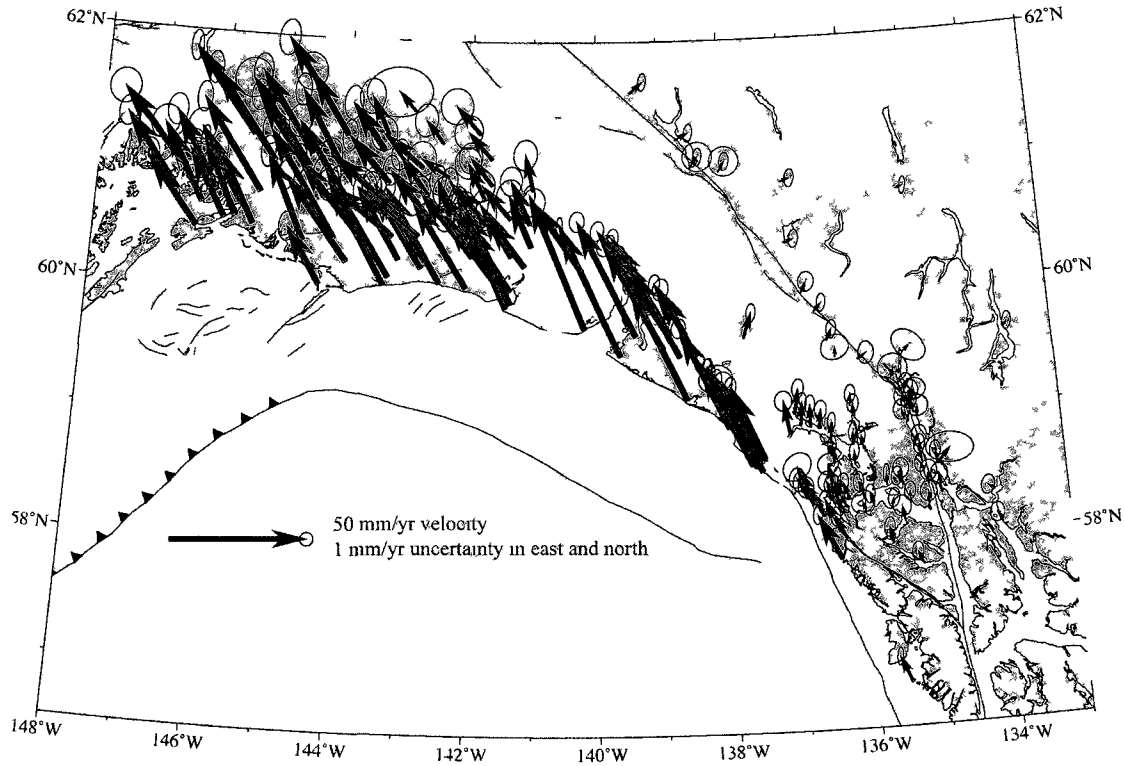

Figure 4.1. Combined velocity field for southeast Alaska and the St. Elias orogen.

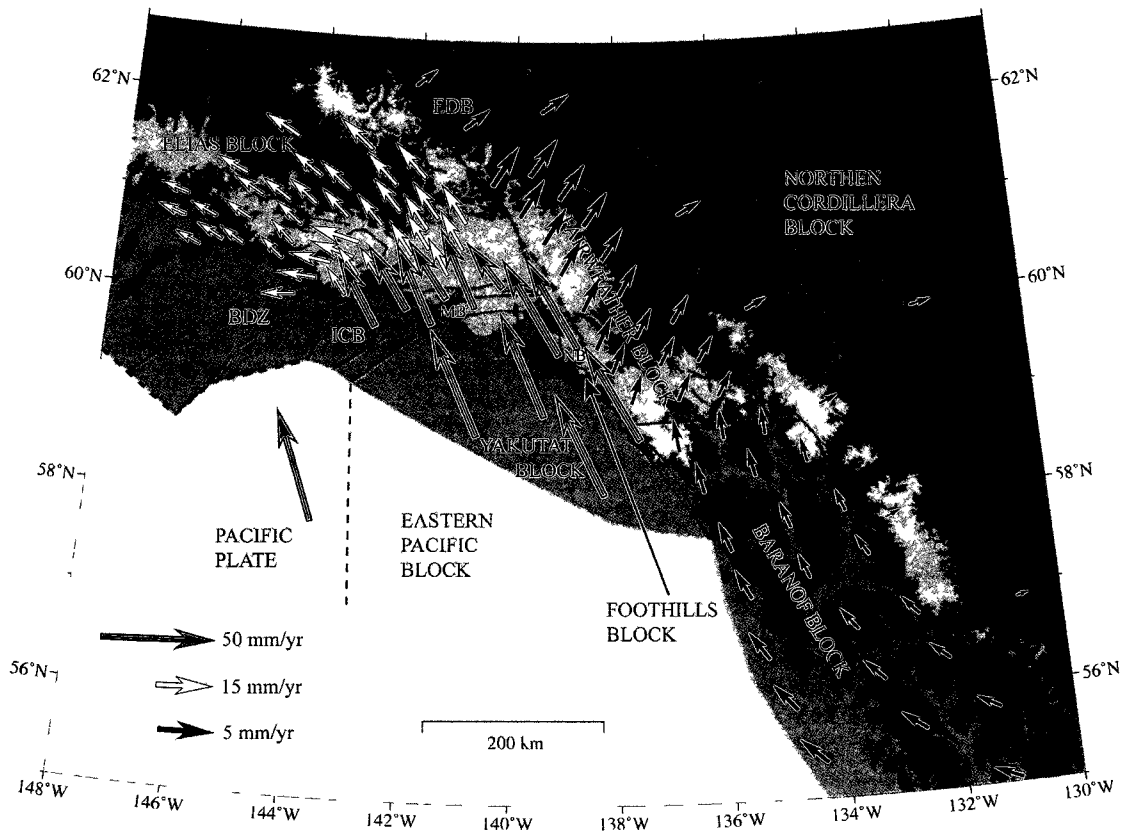

Figure 4.2. Block velocity predictions along the southern Alaska margin.